Micrometre-scale plasticity size effects in metals and ceramics: theory and experiment.

Zhu, Tingting

Micrometre-scale plasticity size effects in metals and ceramics: theory and experiment

Tingting Zhu

School of Engineering and Materials Science

Queen Mary, University of London

Supervisors: Dr. Andy Bushby and Prof. Dave Dunstan

Nov 2008

This thesis is submitted in partial fulfilment of the requirements for the degree of Doctor of Philosophy from Queen Mary, University of London

DECLARATION

I herewith declare that I autonomously carried out the PhD-thesis entitled "Micrometre-scale plasticity size effects in metals and ceramics: theory and experiment".

This thesis contains no material that has been submitted previously, in whole or in part, for the award of any other academic degree or diploma. Except where otherwise indicated, this thesis is my own work.

I hereby affirm the above statements to be complete and true to the best of my knowledge

Signature: Tingting Zhu.

ABSTRACT

This thesis comprises studies of size effects in the plasticity of metals and ceramics at length scales of the order of micrometres and includes both experimental work and theoretical development. Experimental results are presented for foil flexure (nickel and copper) and nanoindentation (ceramics and hard metals). These studies were conducted because existing data does not cover a range broad enough or with sufficient precision to test various theories.

With the developed bending technique, more accurate data is obtained covering a wide range of strain, especially around the key region of the elastic-plastic transition. Moreover, the interaction between grain and thickness size effect is successfully studied by varying the ratio of grain size over thickness of the foils.

After carefully calibrating the indenters, the macroscopic indentation yield strength for ceramics and high strength metals is determined in a direct way by using spherical nanoindentation. The magnitude of size effect is significantly different between metals and ceramics. By comparing the Berkovich and spherical indentation size effect, the results implies that the contact size, a, is the most fundamental length scale in the indentation size effect, independent of the indenter shape. The indentation strength is found to be inversely scaled with the square root of a.

The slip-distance theory (based on (Conrad *et al.*, 1967)) with an 'effective length scale' reconciling intrinsic and extrinsic size effects appears able to account for the size effects in all contexts, without requiring strain gradient plasticity theory or an implicit characteristic length.

ACKNOWLEDGEMENTS

First and foremost, I would like to express my sincere gratitude to my supervisors Dr. Andy Bushby and Prof. Dave Dunstan, who gave me unstinting support, guidance and extreme patience through my PhD. I have learnt so much during my years in QM, much of which is due to you.

Thank you to Prof. Tony Evans for aiding my work. I would also like to deeply thank Dr. Nigel Jennet, Dr. William Clegg, Prof. Tony Kelly and Dr. Michelle Oyen for valuable discussions and ideas.

I would like to extend my gratitude to my collaborators and colleagues Prof. Mark Hopkinson, university of Sheffield for growing the samples. The gratitude is extended to Dr. Ken P'ng, Dr. Chris Walker, Dr. Geoff Gannaway, and soon to be Drs. Xiaodong Hou, Tanya Ekers, Bruno Ehler and Sandra Korte. Thanks for your help in this work.

I would like to thank Ms Kathy Boydon, Ms Kate Shine, Ms Jazmina Moura, Mr Jonathan Hills, and Mr George Anderson for your support and big help.

I would also like to extend my big thanks to my friends, Jin Luo, Shima Shams, Dun Lu, Xiaole Weng, Shuang Yu, Wei Wang and Shuanwu Li.

A special thanks to my boy friend Wanrui, for your endurance and support and being with me through the most critical stages of this work.

Dedicated to my dearest parents: the most important people in my life! To my loved father, who always believes in my capabilities and encourages me throughout my life. To my mother for the unconditional loves and supports. You are dearly

cherished. I love you both than anything else in the world, and want to thank you for everything.

The financial support provided by EPSRC is gratefully acknowledged.

Thank you all!!

CONTENT LIST

FIGURE LIST

TABLE LIST

PUBLICATIONS LIST

Zhu, T.T., Bushby, A.J. and Dunstan, D.J.: 2008. Size effect in the initiation of plasticity for ceramics in nanoindentation. *Journal of the Mechanics and Physics of Solids*, **56**, 1170-1185.

Zhu, T.T., Hou, X.D., Bushby, A.J. and Dunstan, D.J.: 2008. Indentation size effect at the initiation of plasticity for ceramics and metals. *Journal of Physics D: Applied Physics*, **41**, 074004-10.

Zhu, T.T., Bushby, A.J. and Dunstan, D.J.: 2008. Review of mechanical size effect. *Materials Science and Technology*, accepted.

Zhu,T.T., Hou, X.D., Walker, C. J., P'ng, K. M.Y., Dunstan, D. J. and Bushby, A. J.: 2006, Size effect in the initiation of plasticity for ceramics in nanoscale contact loading. *Mater. Res. Soc. Symp. Proc.*, **976**, 0976-EE06-12.

Zhu, T.T., P'ng, K.M.Y., Bushby, A.J. and Dunstan, D.J.: 2007. Mapping of the initial volume at the onset of plasticity in nanoindentation, *Mater. Res. Soc. Symp. Proc.*, in press.

Zhu, T.T., Bushby, A.J. and Dunstan, D.J.: 2008. Analysis of the inverse square-root size effect in plasticity of metals. *J. Mech. Phys. Solids*, submitted.

Zhu, T.T., Bushby and A.J., Dunstan: Geometrical critical thickness theory for the size effect at the initiation of plasticity. *Mater. Res. Soc. Symp. Proc.* in preparation.

Bushby, A.J., **Zhu, T.T.** and Dunstan, D.J.: 2008. Slip distance model for the indentation size effect at the initiation of plasticity in ceramics and metals. *Journal of Materials Research*, in press.

Hou, X.D., **Zhu, T.T.**, Jennett, N.J. and Bushby, A.J.: 2006. The identation size effect and Hall-Petch behaviour of annealed polycrystalline copper, *Mater. Res. Soc. Symp. Proc.*, **976**, 0976-EE09-10.

Dunstan, D. J., P'ng, K. M. Y., **Zhu, T. T.**, Hou, X. D., Walker, C. J. and Bushby, A.J.: 2007. Strength of strained quantum wells and other small scale structures. *Phys. stat. sol. (b)*, **244**, 93–99.

Ehrler, B., Hou, X.D., **Zhu, T.T.**, P'ng, K.M.Y., Walker, C.J., Bushby, A.J. and Dunstan, D.J.: 2008. Grain size and sample size interact to determine strength in soft metals, *Philo Mag.*, in press.

Dunstan, D.J., Ehrler, B., **Zhu, T.T.**, Hou, X.D., P'ng, K.M.Y. and Bushby, A.J.: 2008. The strength of thin films, small structures and materials under localised stresses. *Int. Conf. on Metal. Coatings and Thin Films*.

1 Introduction

Knowledge of the mechanical behaviour of materials is essential in materials science and applied mechanics. At large size scales, above say 1 millimetre, most materials' properties are well-established and constitutive models are available. Classical continuum plasticity models predict identical stress–strain responses for different geometrical dimensions, i.e., classical continuum answers are size independent. However, during the last few decades, it has become clear that mechanical properties can change drastically when the specimen dimensions are small. The strength of a material increases either when the structure is small or when only a small volume is under strain. The term 'size effect' covers generically all the ways in which this may happen. Nowadays, most material technologies rightly emphasise miniaturisation, from biomedical devices to thermal barrier coatings. Understanding small-scale mechanical properties is at the cutting-edge of materials science and technology.

This thesis comprises studies of plasticity size effects of metals and ceramics including both experimental work (bending and nanoindentation) and theoretical development (slip-distance theory), as the existing data is considered to be not covering a range broad enough or with sufficient precision to test various theories. Another motivation is that the interaction between intrinsic (grain size) and extrinsic (dimensional) size effect is interesting for engineering applications, but rarely reported both in experiments and in theories.

Two of the best experimental results on size effect studies are from measurements of the stress-strain relationship for thin copper wires in torsion (Fleck *et al.*, 1994) and for thin nickel foils in bending (Stölken and Evans, 1998). However, it is claimed that these data are fitted equally well by critical thickness theory as strain gradient plasticity theory (Dunstan and Bushby, 2004). Also, the interaction between grain size d and dimensional size (thickness) h is interesting, but not considered in these studies. Moreover, understanding the influence of material properties on these size effects is crucial for engineering design. Correspondingly, the bending technique (Stölken and Evans, 1998) is improved and performed on nickel (in chapter 3) and copper (in chapter 4) thin foils over a wider range of grain size and strain. Yield and work hardening size effects were clearly observed and analysed (in chapter 5). Finally, the influence of material properties was studied by comparing bending results of nickel and copper foils.

The study of the initial yield size effect via indentation is limited in the literature due to the difficulty in measuring yield strength (Syed Asif *et al.*, 1997; Gouldstone *et al.*, 2000; Leipner *et al.*, 2001; Herbert *et al.*, 2006). Recently, Spary *et al.* (2006) determined the yield strength of soft metals through finite element simulation together with spherical nanoindentation and claimed that the yield strength scaled as the inverse cube root of indenter radius R. However, all of the metals investigated in their study have relatively low yield strength, in which it is difficult to determine the yield point with low uncertainty. Hence, the yield size effect was studied in ceramics and hard metals (in chapter 7) here, which possess relatively high yield strength that

nonetheless deform by dislocation glide or twinning. Moreover, material parameters are extended by studying the indentation size effect in ceramics and hard metals. Finally, size effect of pointed indentation is studied together with that of spherical indentation.

In a remarkable number of instances the material strength scales with the reciprocal square root of the smallest length scale (specimen dimension, film thickness, grain size and contact size etc): denoted as $1/\sqrt{l}$ (Data obtained in bending and indentation in this work; Hall, 1953; Ma and Clarke, 1995; Swadener *et al.*, 2002; Volkert and Lilleodden, 2006). In the majority of these cases, strain gradients are involved, the most cited explanation is the strain gradient plasticity (SGP) theory, where the size effect can be attributed to hardening due to geometrically-necessary dislocations (GNDs) (Ashby, 1970). A characteristic length l^* is often introduced to parameterise the theory. In other cases, strain gradients are not involved; for instance, micro-pillar compression has uniform deformation without strain gradients, but also appears to closely follow $1/\sqrt{l}$ scaling (Volkert and Lilleodden, 2006). In this study, the slip-distance theory (Conrad *et al.*, 1967) naturally generates the $1/\sqrt{l}$ scaling and incorporates the material parameters that influence the size effect, without requiring strain gradient plasticity theory or an implicit characteristic length (chapter 8). A new analysis of the interactions of grain size and structure size is given which yields in excellent agreement with experiment in different loading geometries. This model also suggests that the yield strain and Burger's vector are the important material parameters in the size effect, which agrees well with the experimental observations.

2 Literature review - size effects and their interpretations

(This part has been accepted by Journal of Materials Science and Technology)

2.1 Introduction

The strength of a material increases either when the structure is small or when only a small volume is under strain. This behaviour is the so-called mechanical size effect.

The size effect can be categorized as 'intrinsic' and 'extrinsic'. Intrinsic size effects are due to microstructural (internal) constraints of materials, such as grain size. These are mainly controlled by processing steps in material fabrication. The extrinsic size effects are caused by dimensional constraints. These might be due to small sample size, in which physical mechanisms begin to experience the presence of the surface or an (external) interface (e.g. multilayer). A dimensional (extrinsic) constraint can also arise from the loading system, where the strained volume is small. Interactions between intrinsic and extrinsic size effects are particularly interesting for commercial use. However, currently, understanding of both the physics driving the size effects and their interaction is limited.

In this study, only the plastic behaviour (e.g. plastic yield point and work hardening) is considered. In other words, only the properties of material governed by dislocations are concerned here. There are good physical reasons why elastic properties do not change with size in the ranges of size considered here (e.g. no size dependence of Young's modulus).

Here, the small-scale strengthening phenomenon and historical and current explanations are briefly reviewed.

2.2 Intrinsic size effect – mechanical strengthening of materials due to microstructural constraints

2.2.1 Grain size strengthening in plasticity

Grain size has long been known to have a significant effect on the mechanical behaviour of materials, e.g. yield strength and fracture resistance (Brown and Ham, 1971).

The effect of grain size was first established quantitatively by Hall (1951) and Petch (1953) for the yield stress of low carbon steels as:

$$\tau_y = \tau_0 + kd^{-1/2} \tag{2.1}$$

where d is the grain size, τ_0 the lattice friction stress of single crystal material and k the Hall-Petch slope. Eq. (2.1) is generally referred to as the Hall-Petch effect.

Although the Hall-Petch behaviour is observed frequently (bcc metals (Cracknell and Petch, 1955), fcc metals (Armstrong *et al.*, 1962; Phillips and Armstrong (1972)) and alloys (Shaw, 1967)), the underlying mechanism is still unclear. Here, several commonly cited explanations are reviewed briefly.

In addition, there has been a growing interest in nanostructured materials, where d is smaller than tens of nanometres. Currently, it is strongly argued that the experimental results on nano-crystalline materials reveal that the Hall–Petch

relationship ceases to be valid. However, it is not our main concern here; a full review can be found in Meyers *et al.* (2006).

1. Dislocation pile-up model of Hall-Petch effect

The earliest attempt to explain the Hall-Petch behaviour is the dislocation pile-up model by Hall (1951) with subsequent modifications by Petch (1953), Li (1963; 1970) and Cottrell (1964). This model assumes that at the grain boundary, there exist obstacles (e.g. locked dislocations), which will be overcome at a critical stress τ_c. Under an effective stress τ_e ($\tau_e = \tau - \tau_0$), dislocations nucleated in the grains will pile up along the slip plane against the grain boundary due to their mutual repulsion. When the stress concentration at the tip of pile up, τ_p, reaches the critical value τ_c, dislocations will cross the grain boundary and move to the next grain. Imagining the simplest pile up, i.e. single-layer pile up of a group of n dislocations, as illustrated in Fig. 2.1, the pile up force at the tip of the array is:

$$\tau_p = n\tau_e \tag{2.2}$$

If the pile up has a length of L_p (illustrated in Fig.2.1), from the analysis due to (Eshelby, 1951), n can be expressed as a function of the L_p:

$$\frac{\tau_e L_p b}{n} = \alpha \mu b^2 \tag{2.3}$$

where α is a coefficient and μ shear modulus. Now assuming that the pile-up length L_p equals to the grain size d, the stress is related to the grain size as:

$$\tau_y = \tau_0 + \sqrt{\frac{\alpha \tau_c \mu b}{d}} \tag{2.4}$$

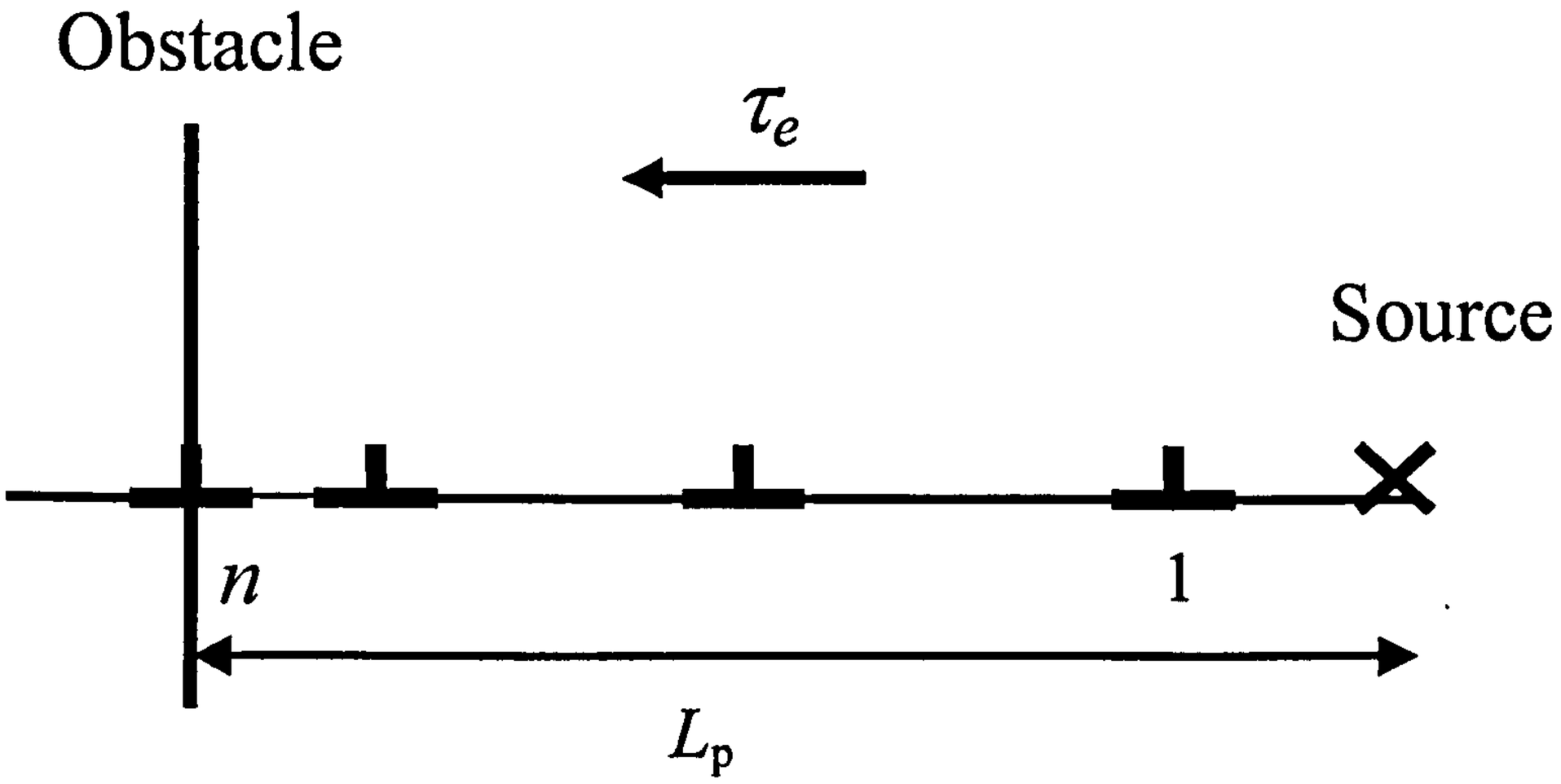

Figure 2.1 Dislocation pile-up model. Under effective shear stress τ_e, an array of identical dislocations piles up along the slip plane against an obstacle. The obstacle here represents the grain boundaries.

This theory explains the sharp yield point of low-carbon steels very well. However, this well defined model suffers the weakness that the pile up is rarely observed directly; especially in fcc metals (Li, 1963; 1970).

2. Grain boundary source model of Hall-Petch effect

Attempts to obtain mechanisms which do not require the presence of pile-ups were made by Li (1963, 1970), Crussard (1963) and Murr (1975). They proposed that irregularities at grain boundaries (steps or ledges) act as dislocation sources to provide a dislocation density near to the grain boundary (illustrated as Fig.2.2) as:

$$\rho = \frac{\beta m}{d} \tag{2.5}$$

where m is the ledges or steps density and β is a geometrical coefficient (In (Li, 1970), $\beta = 3$). Considering the Taylor's hardening law (Taylor, 1934) for forest dislocations hardening:

$$\tau = \tau_0 + \alpha\mu b\sqrt{\rho} \tag{2.6}$$

and substituting Eq. (2.5) into (2.6), shear stress is related to grain size as:

$$\tau = \tau_0 + \alpha\mu b\sqrt{\frac{\beta m}{d}} \tag{2.7}$$

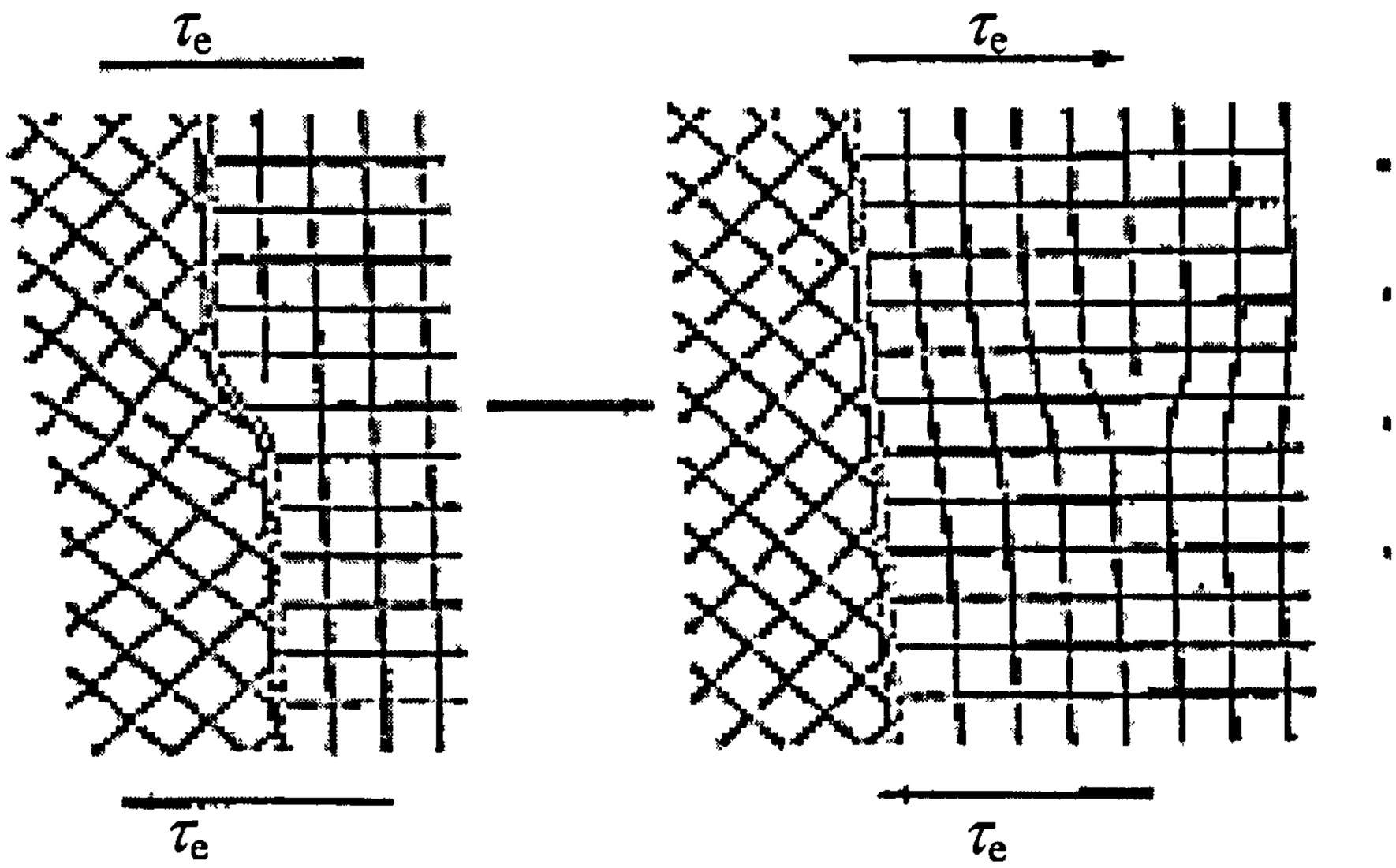

Figure 2.2 Schematic plot of grain boundary source model for Hall-Petch effect. Under the effective stress τ_e, grain boundary ledge act as a donor of dislocations (Li, 1963).

3. Slip-distance model of Hall-Petch effect

The main point of the slip-distance model proposed by Conrad *et al.* (1967) is that the presence of grain boundaries reduces the average dislocation moving distance s (illustrated in Fig. 2.3), and s is assumed to be linearly scaled with d. Under uniform

deformation, the dislocation density can be related to plastic strain ε_{pl} and slip distance as:

$$\rho = \frac{\chi \varepsilon_{pl}}{bd} \tag{2.8}$$

where χ is a coefficient. Considering the Taylor hardening law (Taylor, 1934) Eq. (2.6), the stress is related to grain size as:

$$\tau = \tau_0 + \alpha\mu\sqrt{\frac{\chi b \varepsilon_{pl}}{d}} \tag{2.9}$$

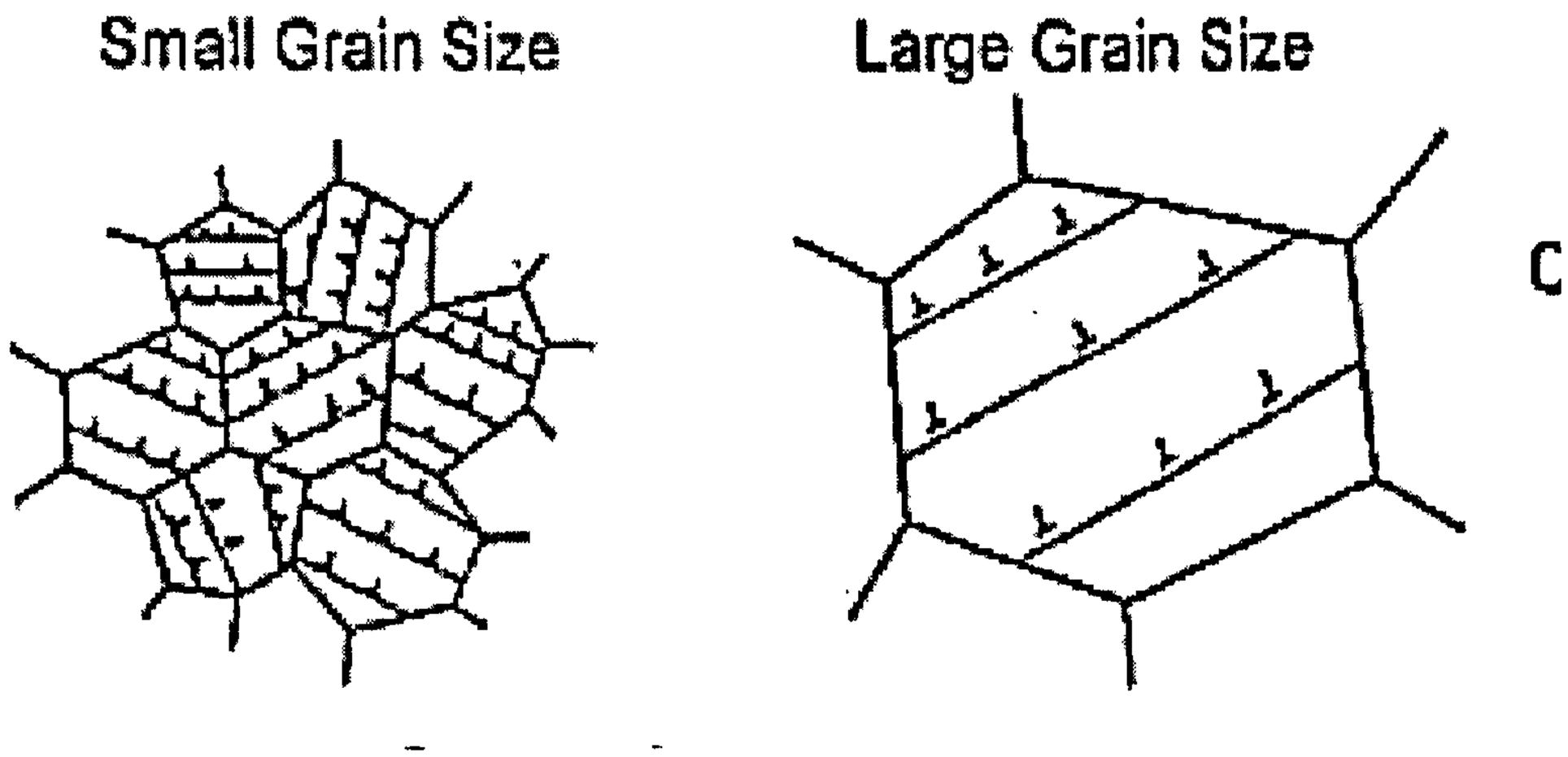

Figure 2.3 Illustration of dislocation mechanism in slip distance model. Dislocation free slip distance is decreased in smaller grain sizes. (Conrad, 1967, 2005)

4. Geometrically necessary dislocation model of Hall-Petch effect

The conventional models (Hall, 1951; Petch; 1953) of the plastic behaviour of crystalline metals is commonly based on the assumption that the resistance to dislocation glide is due mainly to the random trapping of dislocations by each other or boundaries during locally homogenous deformation. Such trapped dislocations are referred to as statistically stored dislocations (SSD) by Ashby (1970). They are

recognised as obstacles to further dislocation motion, which results in hardening, i.e., Taylor forest hardening (1934). However, as anticipated by (Nye, 1953; Ashby, 1970), an additional contribution to the density of immobile dislocations, and consequently to hardening, can arise when grains are caused to undergo non-uniform strain. These so-called geometrical necessary dislocations (GND) must occur at grain boundaries to prevent overlap and voids (illustrated as Fig. 2.4), i.e., to accommodate the deformation gradients. The density of GND can be related to the length scale as:

$$\rho_g = \frac{\varepsilon^*_{pl}}{b} = \frac{1}{b}\left(\frac{d\varepsilon_{pl}}{dx}\right) \tag{2.10}$$

where ε^*_{pl} denotes the plastic strain gradient.

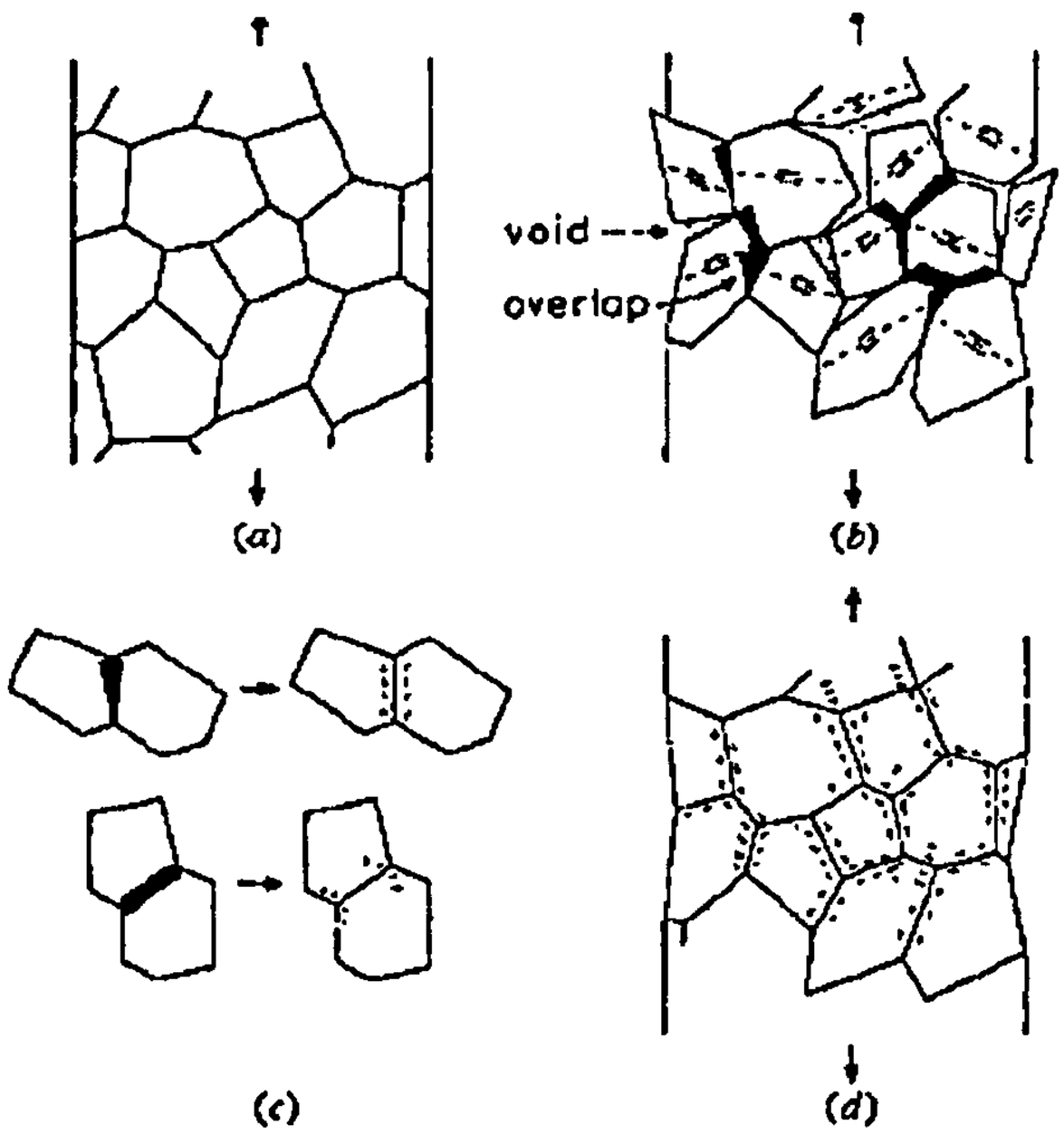

Figure 2.4 If each grain of a polycrystalline metals, shown at (a), deforms in a uniform manner, overlap and voids would appear (b), these can be corrected by introducing geometrically necessary dislocations, as shown at (c) and (d). (Ashby, 1970)

When the length (here the grain size d) is minimised, the density of the SSD is far smaller than that of the GND. Considering the Taylor hardening (Taylor, 1934) law of Eq. (2.6), the stress is related to the grain size d as:

$$\tau = \tau_0 + \alpha\mu\sqrt{\frac{b\varepsilon_{pl}}{d}} \tag{2.11}$$

From above, it can be seen that the Hall-Petch relationship Eq. (2.1) is generally true. However, various theories exist, and the underlying physics of the grain size effect is still not clear.

2.2.2 Particle strengthening in plasticity

Another common intrinsic length scale is the average particle spacing L in second-phase particle precipitation. In this case, particles are acting as obstacles hindering the dislocation movement. Plastic deformation happens when dislocations bow out to fully bypass the obstacles (the "Orowan mechanism" (Orowan, 1947)). The bypass condition is reached when:

$$d_d = L \tag{2.12}$$

where d_d is the dislocation loop diameter. It is a function of shear flow stress as:

$$d_d = \frac{\alpha\mu b}{\tau} \tag{2.13}$$

Subsequently, the stress is related to the average particle spacing as:

$$\tau = \frac{\alpha\mu b}{L} \tag{2.14}$$

This theory agrees well with experimental observations by Lloyd (1994) on A356-SiC.

2.3 Extrinsic size effect

2.3.1 Thin film strengthening in plasticity

Strong size effects have been observed in thin metal film coatings, when film thickness h_f is below hundreds of nanometres. Experiments carried out characterizing the mechanical properties under either thermal or mechanical loading (Shen *et al.*, 1998; Hommel and Kraft, 2001; Philps *et al.*, 2004) have shown that the plastic response depends strongly on h_f and on whether or not the films are passivated (Fig.2.5). The yield strength is found to be inversely scaled by h_f.

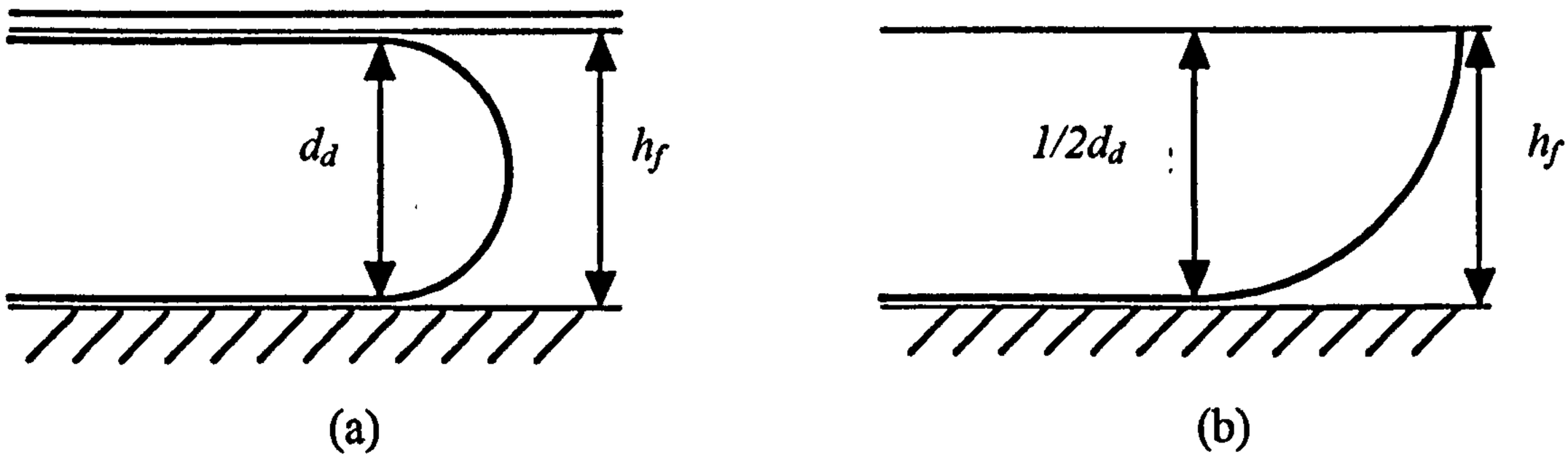

Figure 2.5 The dimensional constraint on plasticity in thin films: the yield stress can be estimated by requiring a dislocation loop to fit into the film (d_d= h_f). Case (a): impenetrable film surface; case (b): free film surface.

The size effect in thin film has been well explained by misfit dislocation channelling theory, which was firstly introduced by Frank and Van der Merwe (1949). Matthews *et al.* (1966) subsequently developed this idea to explain the epitaxial layer growth (critical thickness theory) in semiconductors. Finally, Freund (1987) and Nix (1989) applied detailed calculations for explaining metal thin-film coating strengthening.

A misfit dislocation is generated from the substrate, and passes through the film channel as schematically shown in Fig. 2.5. Plastic deformation occurs when the dislocation loop fits in the thin film channel (Fig. 2.5). According to the film surface condition, yield happens for (a) surface impenetrable, dislocation loop diameter equal to film thickness, $d_d = h_f$. (b) free surface, $1/2d_d \doteq h_f$. The yield strength is related to the film thickness,

$$\tau_y \propto \frac{\eta\alpha\mu b}{h_f} \tag{2.15}$$

The constant of proportionality, η for Eq. (2.15) varies according to the surface condition, either 1/2 or 1. In stead of simple shear modulus μ, the elastic modulus is much more complicated in the complete calculation (Nix, 1989). Details of this theory can be found elsewhere (Fitzgerald, 1991; Dunstan, 1997).

Recent experimental evidences for multilayer materials, when layer thickness is above hundreds of nanometres, shows that strength is scaled with reciprocal square root of layer thickness: $\tau_y \propto h_l^{-1/2}$ (Misra *et al.*, 2005; Hoagland *et al.*, 2005). Fang and Friedman (2005) rather than h_l^{-1} as given by Eq. (2.15) suggest a possible reason of this 'Hall-Petch' type behaviour: when the h_l is big enough (e.g., above hundred nanometres), the Frank-Read source is able to work many times in the layer; hardening is attributed to dislocation interaction, where the multilayer interfaces behave as obstacles for dislocation movement analogously to grain boundaries.

2.3.2 Compressive strengthening – micropillar experiments and their explanations

Micro-pillar compression experiments have attracted extensive interest during the last four years. Pillars with diameters ranging from 0.5 to 40μm have been machined from a bulk single crystal (including nickel (Rinaldi *et al.*, 2008), copper (Kiener *et al.*, 2005), gold (Volkert and Lilleodden, 2006; Greer *et al.*, 2005) and intermetallic Ni_3Al (Uchic *et al.*, 2004; Dimiduk *et al.*, 2007)) by using a focused ion beam (FIB) microscope then subjected to uniaxial compression in nanoindenter systems equipped with a flat diamond punch (Fig. 2.6). These experiments provide a simple geometrical loading system, without interfaces and strain gradient (Budiman *et al.*, 2008). However, FIB will cause a damaged surface layer on the outside of the pillars, which will influence the experiment. These issues are discussed in refs (Volkert and Lilleodden, 2006; Kiener *et al.*, 2005).

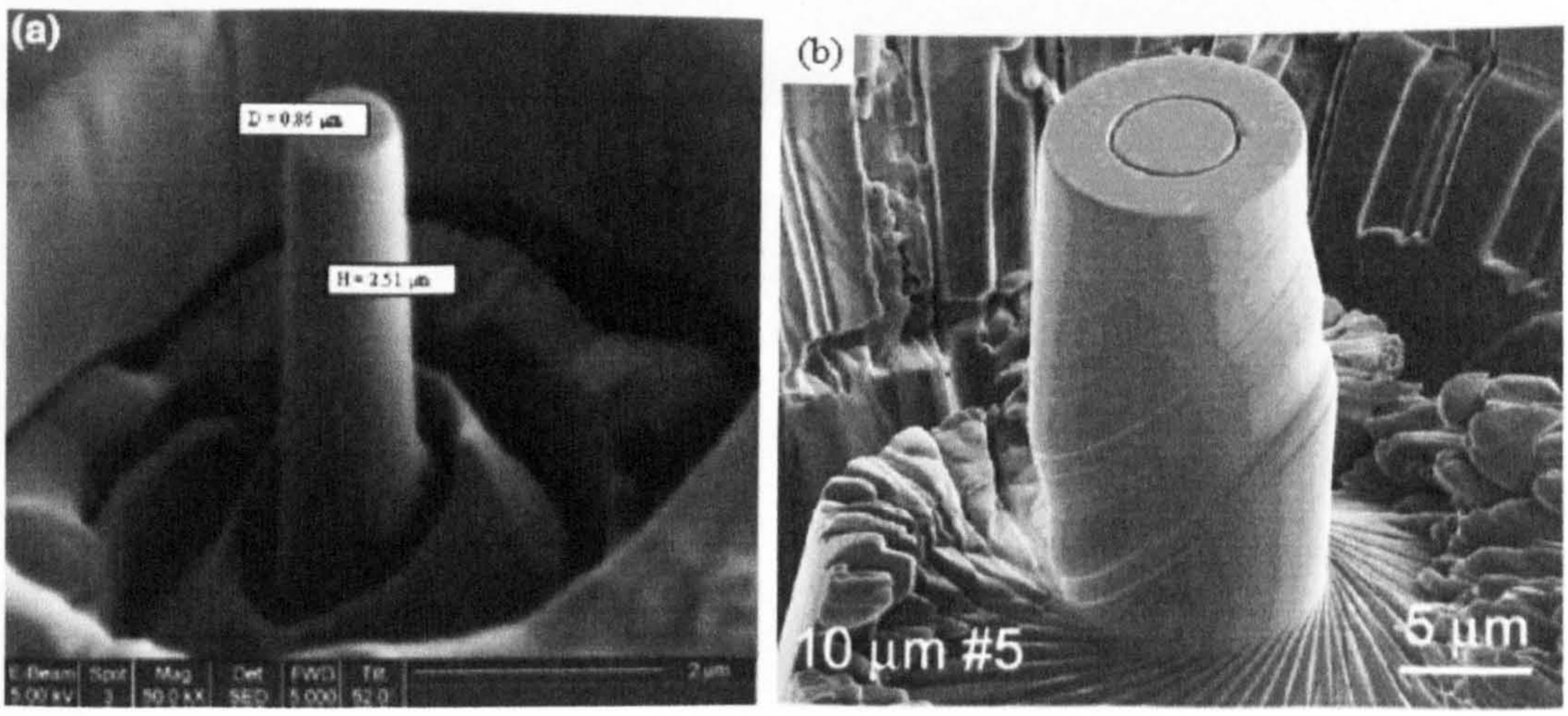

Figure 2.6 (a) FIB image of an 860 nm-diameter, 3.2 μm-tall (0 0 1) gold pillar (b) SEM images of a deformed pillars. Slip lines are clearly presented in the deformed states (Greer *et al.*, 2005).

For a variety of materials, the flow strength of these micron pillars exhibits a strong size effect, where decreasing pillar diameter leads to a higher stress. The yield strength (at 2% or 5% strain) was reported to be scaled with the reciprocal square root of the pillar diameter (Volkert and Lilleodden, 2006; Greer *et al.*, 2005)

One of the most commonly cited explanations for this size effect is the dislocation starvation mechanism. Dislocations leave the pillar before their multiplication (Shan *et al.*, 2008; Greer *et al.*, 2005). Correspondingly, higher stress will be required for dislocation nucleation in order to continue deformation. However, for this dislocation starvation mechanism, there is so far, no accurate mathematical description able to test the result numerically (Kiener *et al.*, 2006).

2.3.3 Crack size effect- Griffith theory

The famous crack size effect on brittle materials by Griffith (1920) might be the earliest size effect established in the literature. Griffith demonstrated experimentally that the failure stress of glass tubes is proportional to the inverse square root of the crack size. This behaviour was widely observed evidently afterwards (Lawn, 1975).

This phenomenon is well explained by a thermodynamic law (Griffith, 1920; Rack, 1946). Assuming a planar crack with length $2c$ in a homogeneous medium, the total energy U_t of the system is a sum of the mechanical contribution:

$$U_t = W_{External} + U_{Surface} \tag{2.16}$$

where $W_{External}$ is the strain energy caused by external loading and $U_{Surface}$ is a crack resistance term, originating from the material resistance to create a new free surface by breaking chemical bonds,

$$W_{External} = \frac{\pi c^2 \sigma^2}{E} \tag{2.17}$$

where E is the Young's modulus of the material. Also,

$$U_{Surface} = 4c\gamma_s \tag{2.18}$$

where γ_s represents the free surface tension at the cleavage surface. It is a material constant.

The critical condition (failure) happens at the smallest rate of the total energy change with crack extension: $\frac{dU_t}{dc} = 0$. Correspondingly, failure stress is scaled as the inverse square root of the crack length as: $\sigma_f = \sqrt{\frac{2E\gamma}{\pi c}}$.

2.3.4 Microbending and microtorsion size effects and their explanations

In 1994, Fleck *et al.* (1994) carried out microtorsion experiments (Fig.2.7 (a)) on thin polycrystalline copper wires with diameters ranging from 12 to 170μm and observed a very strong size effect. When the diameter of the wires is decreased, the strength (normalised torque) is increased significantly (Fig. 2.7 (b)). A similar phenomenon was observed by Stölken and Evans (1998) in microbending experiments (Fig. 2.7(c)) performed on thin nickel foils with thicknesses ranging from 12.5 to 100μm (Fig. 2.7 (d)). However, the data from Stölken and Evans (1998) shows relatively big error bars. Also, both of these two experiments present data at relatively high strain, i.e., there is a lack of data around the key region of elastic-plastic transition or yield point (in Fig. 2.7(b) and (d)).

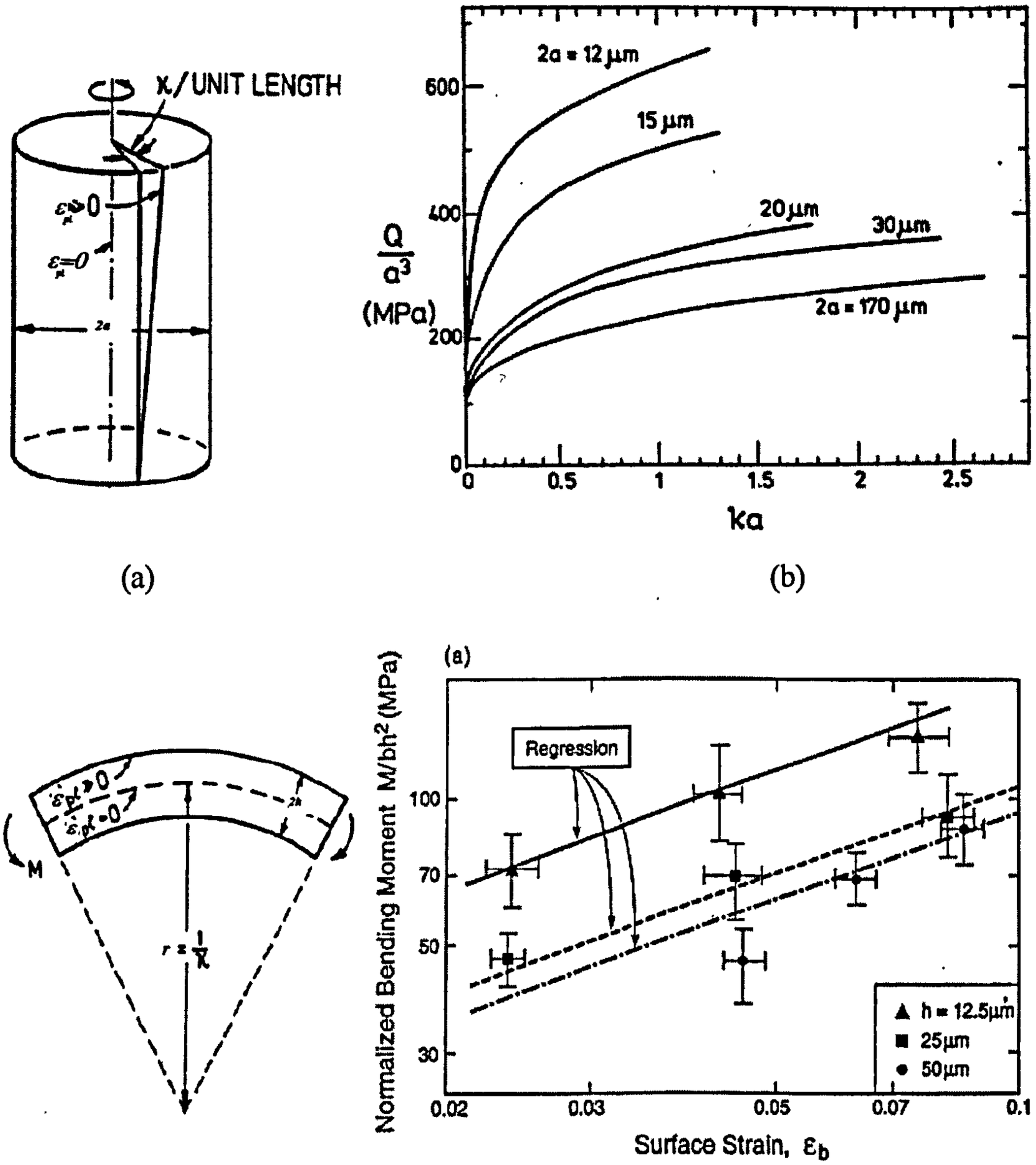

Figure 2.7 (a) Schematic plots of simple twisting of wires (Modified from Fleck *et al.*, 1994) (b) twisting size effects observed by Fleck *et al.* (1994); strength (normalised torque) is increased with decreasing radius of wire (c) Schematic plots of simple bending of foils (modified from Fleck *et al.*, 1994) (d) bending size effect obtained by Stölken and Evans (1998); strength (normalised moment) is increased with decreasing foil thickness.

2.3.4.1 Strain gradient plasticity theory

The original and most cited explanation of non-uniform size effects is the well-known strain gradient plasticity (SGP) theory (Fleck *et al.*, 1994; Fleck and Hutchinson, 1993; Stölken and Evans 1998). As mentioned in section 2.2.1(4), dislocations can store in two different ways. One is by dislocations trapping each other in a random way, which is referred to as statistically stored dislocations (SSDs). The other one referred to as geometrically necessary dislocations (GNDs), which are required to accommodate the plastic strain gradient. Illustrated in Fig.2.7 (a) and (c), the plastic strain ε_{pl} is null at the neutral planes (elastic planes) for both the wire and foil. However, the plastic strain becomes greater than zero at their free surfaces. When the sample size is minimised, a significant plastic strain gradient ε^{*}_{pl} in the system is introduced. Consequently, a high density of GND will be introduced in wires and foils and this corresponds to the strengthening in terms of the Taylor (1934) hardening law.

However, the exact form of the coupling between hardening due to SSDs and GNDs is always controversial, i.e., the combination of the uniform and gradient terms appears in different ways. Correspondingly, different formulas of SGP theories exist (Nix and Gao, 1998; Gao *et al.*, 1999 Fleck and Hutchinson, 1993; 1997; Duan *et al.*, 2001). Two of the most cited formula of SGP theories are presented here.

The first, (I), is the "mechanism-based" formulation suggested by Nix and Gao (1998). The densities of SSDs and GNDs are combined in a linear summation:

$$\rho_t = \rho_s + \rho_g \tag{2.19}$$

where ρ_t is the total density of dislocations, ρ_s the density of SSDs and ρ_g the density of GNDs. In this case Eq. (2.19), the interaction between SSDs and GNDs are not considered. By inserting Eq. (2.19) into the Taylor (1934) hardening law, the resulting shear stress is:

$$\tau = \tau_Y \sqrt{f^2(\varepsilon_{pl}) + \ell_{NG}^{*} \dot{\varepsilon}_{pl}} \tag{2.20}$$

where τ_Y is the macroscopic (or defined) yield shear strength. The uniform strain term: $f(\varepsilon_{pl})$, is associated with the density of SSDs and typically has a power law form,

$$f(\varepsilon_{pl}) = (\varepsilon_{pl} / \varepsilon_Y)^n \tag{2.21}$$

The extra characteristic length scale in the formalism (2.20) is related to the macroscopic yield strength by: $\ell_{NG}^{*} = \alpha^2 b(\mu / \tau_Y)^2$, where μ is the shear modulus and α the coefficient (Gao *et al.*, 1999; Huang *et al.*, 2004).

The second, (II), is suggested by Fleck and Hutchinson (1994), where they adopted the harmonic mean:

$$\rho_t = \sqrt{\rho^2_s + \rho^2_g} \tag{2.22}$$

of the dislocation density, then the resulting stress:

$$\tau = \tau_Y f\left(\sqrt{\varepsilon_{pl}^{\ 2} + (\ell^{*}_{FH} \dot{\varepsilon}_{pl})^2}\right) \tag{2.23}$$

However, all these combination methods for SSDs and GNDs are arithmetic. The physical meaning of these combinations is not clear. The existing data is not able to define the right formula.

2.3.4.2 Geometrical critical thickness theory

In the SGP theories, the high density of GNDs in the presence of a large plastic strain gradient is used to account for extra work hardening. However, as argued by Dunstan and Bushby (2004), the SGP theory cannot explain a size effect at the yield. At the onset of plasticity, there is no plastic strain gradient, hence no GNDs. Therefore, geometrically critical thickness theory (GCTT) was proposed for explaining the initial yield size effects in bending and twisting (Dunstan and Bushby, 2004). The underlying idea is that generation of the dislocation is a cooperative process involving many atoms in the crystal and this process necessarily involves a finite volume rather than beginning at a point. This geometrically required small deformation area or volume restricts the generation (or movement) of dislocations and hence a higher yield stress is required. The additional (geometrically required) yield strain:

$$\Delta\varepsilon \approx \frac{b}{h_c} \tag{2.24}$$

where h_c is the critical thickness for initial yielding, then the total yield strain is expressed as:

$$\varepsilon'_Y = \varepsilon_Y + \Delta\varepsilon = \varepsilon_Y + \frac{b}{h_c} \tag{2.25}$$

here ε_Y is the yield strain for bulk material. In this model, it was also claimed that if dislocation multiplication (significant relaxation) is considered, b in E.q. (2.25) is to be replaced by $5b$ (Dunstan, 1997; Dunstan and Bushby, 2004).

The calculated critical thickness h_c from (Dunstan and Bushby, 2004) is related to the length scale, e.g. radius of the wire a_w:

$$h_c = \frac{1}{\varepsilon_Y}\left(-1+\sqrt{1+\frac{2a_w}{b\varepsilon_Y}}\right) \tag{2.26}$$

Substituting Eq. (2.24) into (2.23), the yield strain is obtained. Details of the GCTT can be found in Dunstan and Bushby (2004).

The data of Fleck *et al.* (1994) and of Stölken and Evans (1998) is fitted equally well by geometrical critical thickness as by strain-gradient plasticity theory (Dunstan and Bushby, 2004). To improve the theory, data is required to be over a wider range of strain (e.g. around the key region of elastic-plastic transition or yield point) and to be more accurate.

2.3.5 Nanoindentation size effect

Indentation size effects have been shown repeatedly during last two decades. For pointed indenters, it is found that the hardness is inversely scaled by the square root of contact depth h_c (Ma and Clark, 1995; Nix and Gao, 1998), illustrated in Fig. 2.8 (a). For spherical indenters, Lim and Chaudhri (1999) first showed that the entire flow curve appears at higher contact pressures for smaller radius indenters in oxygen free copper (illustrated as in Fig. 2.8 (b)). Then, Swadener *et al.* (2002) presented that the hardness is scaled with the inverse square root of indenter radius R in Iridium. More recently, Spary *et al.* (2006) reported that the yield strength is increased linearly with the inverse cube root of R by using finite element analysis (FEA) together with spherical nanoindentation. However, since all the materials in

their study (Spary *et al.*, 2006) have very low strength, it is very hard to accurately determine the yield strength.

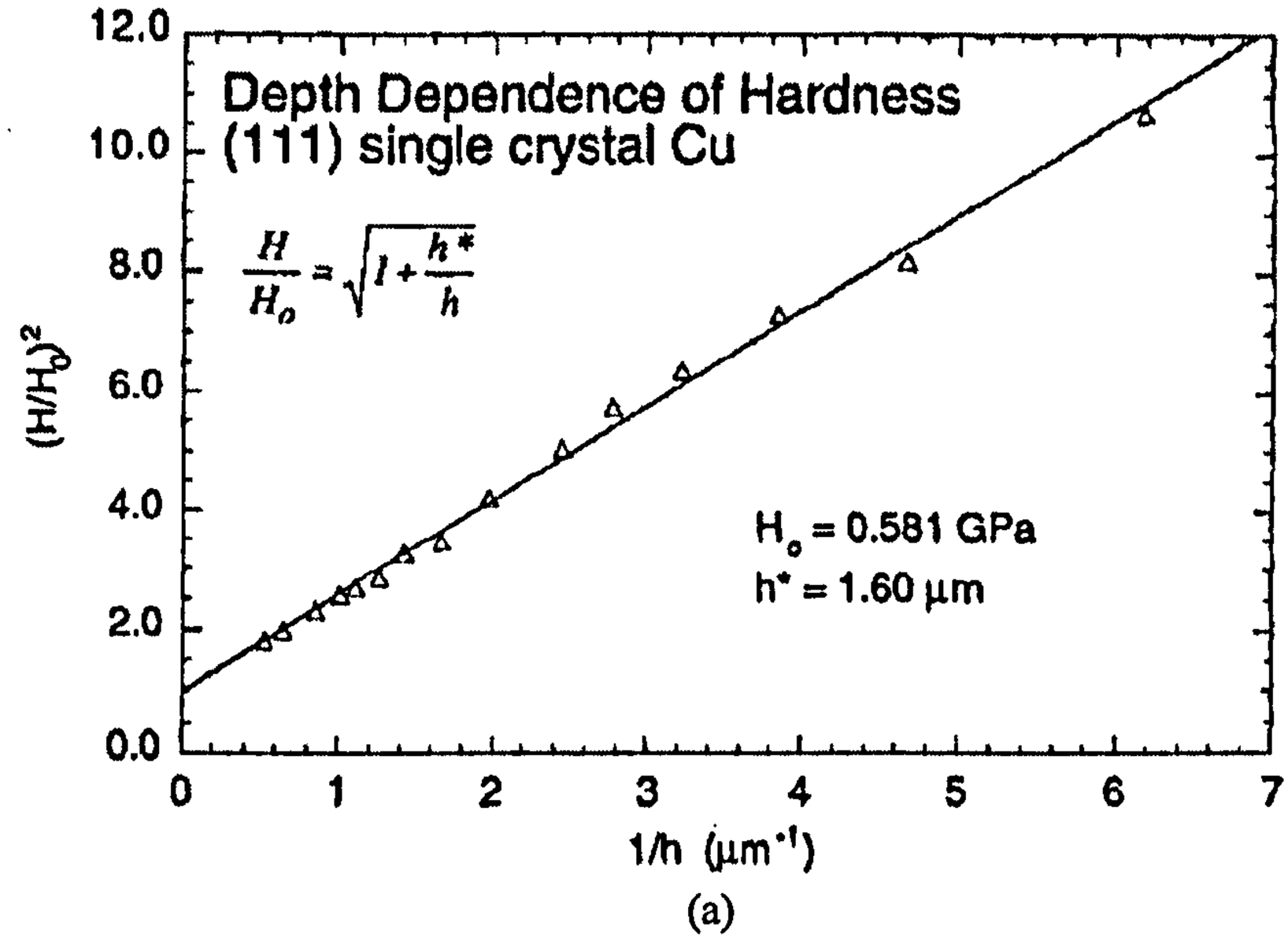

(a)

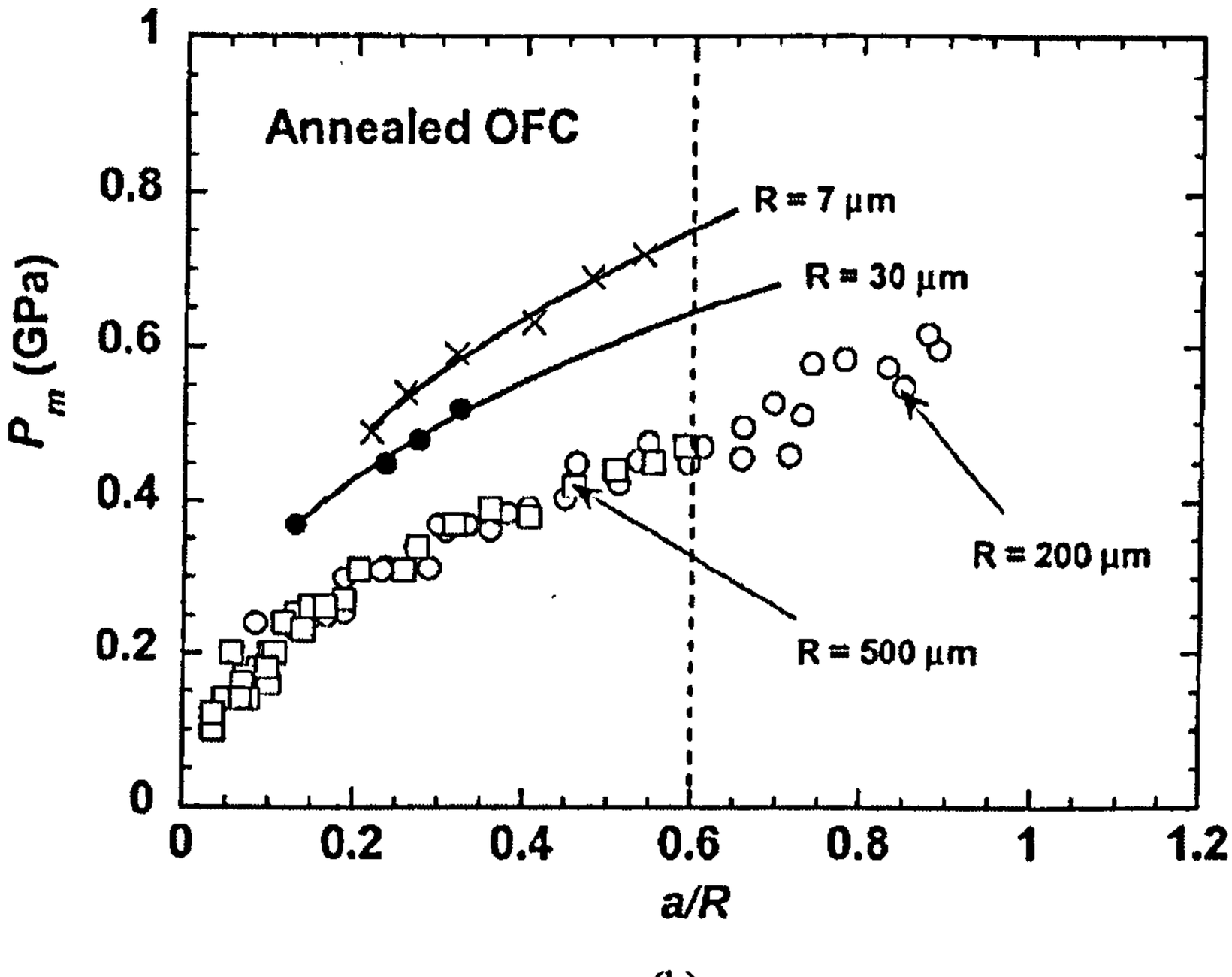

(b)

Figure 2.8 Indentation size effect (a) pointed indentation size effect, where the hardness is inversely scaled with the square root of contact depth. The solid line is the theoretical fit from SGP theory (Nix and Gao, 1998). (b) Spherical indentation size effect is observed by (Lim and Chaudhri, 1999); hardness is clearly increased with decreasing indenter radius. Solid curves are as guides.

These nanoindentation size effects are explained by different theories. The original and predominant theory is the SGP theory. Nix and Gao (1998) showed that the pointed indentation size effect agreed well with the SGP model (in Fig. 2.8(b)). Swadener *et al.* (2002) adopted the same SGP formula to explain their spherical indentation size effect. But the fit is not very good, especially for the smallest radius (R = 14μm). The SGP theory has been introduced and discussed in section 2.3.4.1. The application of the SGP theory for indentation size effect is presented in detail in refs (Nix and Gao, 1998; Swadener *et al.* 2002; Qu *et al.*, 2006; Qin *et al.*, 2007 and etc.).

An alternative approach used by several groups (Gerberich *et al.*, 2003; 2006; Zhang *et al.*, 2002; Kim *et al.*, 2007) considers the indentation size effect via an energy balance argument based on the observations of Horstemeyer and Baskes (2003) for a surface to volume ratio (A_c/ V) of the plastic deformation. They proposed that the work done by an applied indentation load contains both bulk and surface terms respectively:

$$Fdh_p = P_m dV + fdA_c \tag{2.27}$$

where F is the applied indentation force, h_p is the penetration depth, P_m is the indentation mean pressure, f is the surface stress, V is the deformation impression volume under the indenter and A_c is the contact area.

However, it is not very convincing that surface energy plays such an important role in the indentation plastic deformation. For instance, Nicola *et al.* (2007) inputted

bulk and surface dislocation sources into a discrete dislocation model and found that surface sources played a negligible role in their study.

2.4 Interaction between intrinsic and extrinsic size effects

The study of the interaction between intrinsic and extrinsic size effects is certainly an attractive topic, as they appeared frequently in the daily world. However, at present, studies are limited. Venkateswaran and Bravman (1992) studied Al films on silicon substrates and showed that the flow stress is inversely dependent on film thickness and grain size. However, they had only two grain sizes and were not able to distinguish between the Hall-Petch $d^{-1/2}$ dependence and the d^{-1} dependence that they considered more plausible. They assumed that the effects of h and d are separable. On the other hand, Keller *et al.* (1998) reported that observed yield stress size effect is a superposition of thickness and Hall-Petch effect.

Recently, Hou *et al.* (2008) reported a size effect in polycrystalline copper under spherical indentation (illustrated in Fig.2.9). They considered that the intrinsic and extrinsic size effects cooperated. The intrinsic (grain size d) and extrinsic (contact radius a in indentation) are combined in "quadrature" experimentally, where the indentation stress (mean pressure) is related to the a and d as:

$$P_m \propto D^{-1/2} = \sqrt{(1.5a)^{-1} + d^{-1}} \tag{2.28}$$

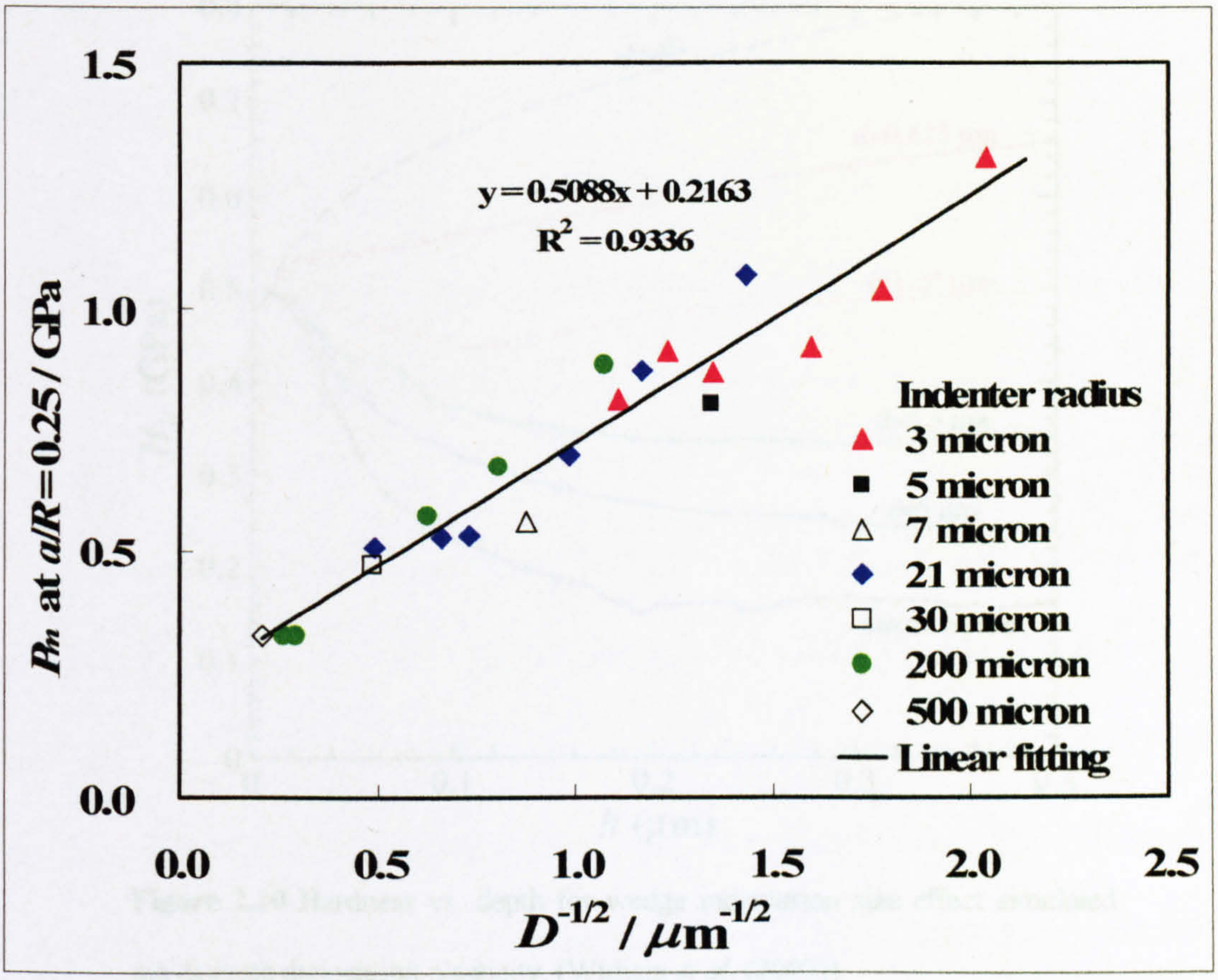

Figure 2.9 Indentation mean pressure P_m (at $a/R = 0.25$) for different radius indenters against the inverse square root of the fitting parameter D here, where $D^{-1} = (1.5a)^{-1} + d^{-1}$.

Widjaja *et al.* (2007) simulated the wedge indentation size effect via two-dimensional discrete dislocation plasticity. They found that both the grain and penetration depth affect the hardness (or mean pressure) as illustrated in Fig. 2.10. The hardness is clearly increased with decreasing grain size or penetration depth. However, they analysed the grain and indentation size effect independently. Interaction between d and a (or h) was not properly considered in their study (Widjaja *et al.*, 2007).

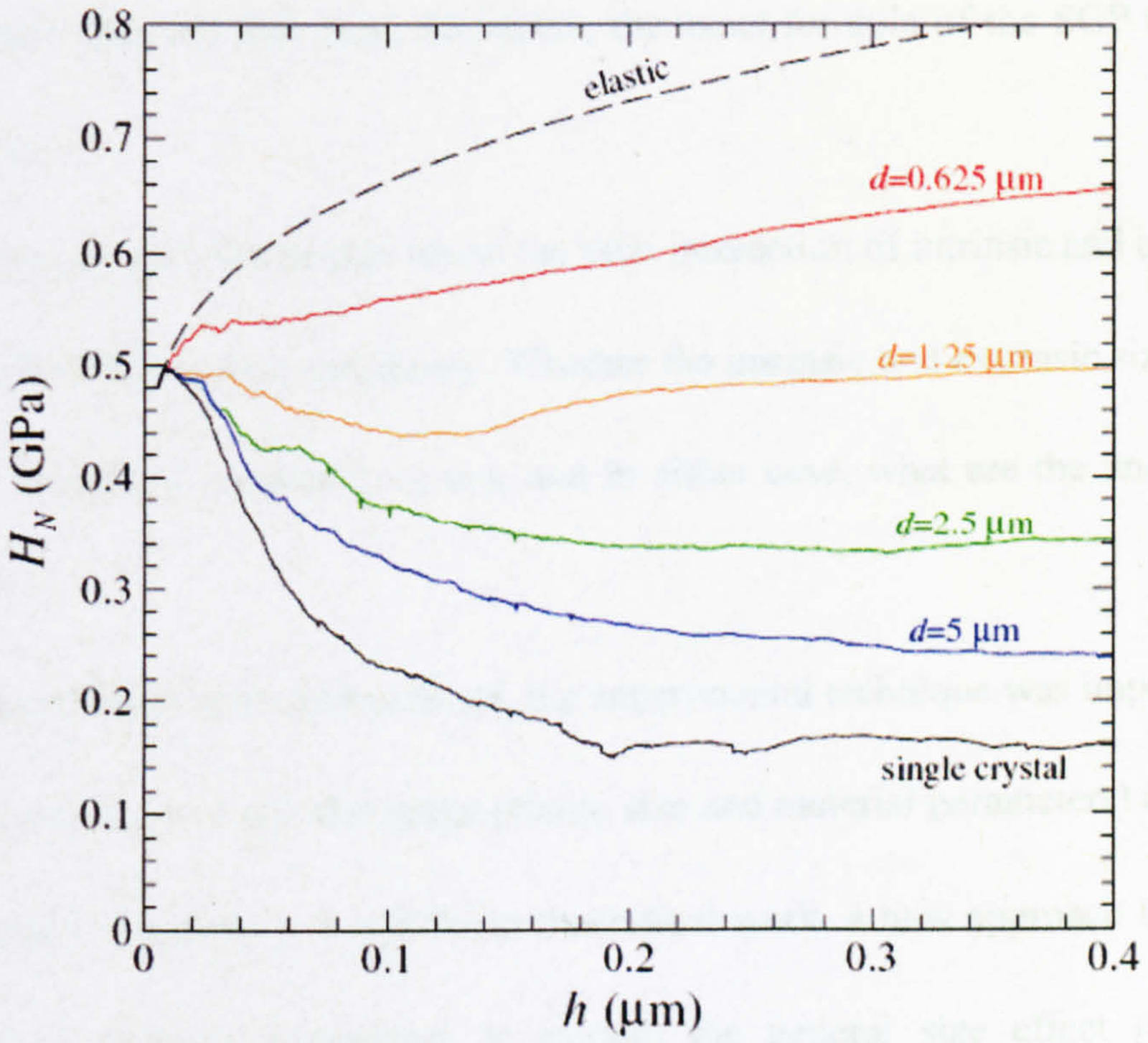

Figure 2.10 Hardness vs. depth for wedge indentation size effect simulated via discrete dislocation plasticity. (Widjaja *et al.* (2007))

2.5 Conclusions

From this review, it can be seen that plastic size effects have been observed and reported repeatedly in different loading geometries during the last five decades. However, there are still weaknesses both experimentally and theoretically. Experimentally, existing data does not cover a large enough range or with sufficient precision to test various theories (e.g., in sections 2.3.4 and 2.3.5). Theoretically, various theories exist. For instance, in section 2.2.1, there are several theories established for Hall-Petch size effects. Also, in sections 2.3.4 and 2.3.5, although the SGP theory are most predominant for explaining size effects involving plastic

gradient, other theories still exist. Moreover, the exact formula of the SGP theory is still not clear.

It is obvious that few people report the vital interaction of intrinsic and extrinsic size effects both in practice and theory. Whether the intrinsic and extrinsic size effect should be considered separately or not, and in either case, what are the underlying mechanics?

In experimental work in this thesis, the experimental technique was improved in order to get results over a wider range (strain, size and material parameters) and with more accuracy (chapters 3, 4 and 7). In theoretical work, a new approach based on Conrad *et al.* (1967) is proposed to explain the general size effect (different geometries; with and without strain gradient). The study of interaction between intrinsic (grain size d) and extrinsic (e.g., thickness h or contact radius a) size effects in experiments and theories (chapter 3, 5 and 8) is also addressed.

3 Microbending of thin nickel foils

(Part of this chapter has been published in Phil. Mag.)

3.1 Introduction

Two of the best experimental results on size effect studies from measurements of the stress-strain relationship are for thin copper wires in torsion (Fleck *et al.*, 1994) and for thin nickel foils in bending (Stölken and Evans, 1998). Strain gradient plasticity theory was applied to explain these results (Han *et al.*, 2005, Huang *et al.*, 2000). However, it has been found recently that these data are fitted equally well by critical thickness theory and by strain gradient plasticity theory (Dunstan and Bushby, 2004). In order to identify a more complete theory, accurate data over a sufficient range of strain is required. Especially, data around the key region of the elastic-plastic transition, or yield point is important. Moreover, the interaction between grain size d and dimensional (thickness) size h is certainly an interesting topic for engineering applications, but reported rarely in the literature (as reviewed in chapter 2).

For the above reasons, the nickel foil flexure (bending) method of Stölken and Evans (1998) was extended to a range of grain sizes d extending from less than the foil thickness h to more than h, and to a range of strains from below yield to values near 0.1. Compared with the previous work of Stölken and Evans (1998), the newly obtained data here are improved both in accuracy and range (strain and grain size). The yield and work hardening size effects are clearly observed. The yield strength and work hardening rate are both increased with decreasing foil thickness or grain size.

In this chapter, the improved bending techniques and experimental procedures are described in detail in sections 3.2 and 3.3. The results are presented and briefly discussed in section 3.4. The detailed fitting and analysis will be shown in chapter 5.

The bending devices were designed by my supervisor Prof. Dave Dunstan and built by Dr. Geoff Gannaway. The experimental works here were done together by my colleague Xiaodong Hou and me.

3.2 Materials preparation and characterisation

In order to study the thickness and grain size effect, the bending measurements were performed on high purity Ni foils over a range of thickness and grain size. Foils having three thickness (h = 10, 50 and 125μm) were obtained from Goodfellow (Cambridge Limited, UK), of purity 99.90, 99.95 and 99.99%, respectively. The 10μm and 50μm foils were electroformed. The 125μm ones were formed by rolling. Various grain sizes were attained by rapid thermal annealing under vacuum. The grain size, texture condition and surface roughness of all foils were characterized afterwards.

3.2.1 Annealing

A rapid thermal annealer (RTA) was used to control the microstructure of the foils (Fig.3.1). It was designed and built by Dr. Gillin from Physics department, Queen Mary University of London. It is a furnace capable of rapid high temperature ramp accurate to ±1°C and is programmed to ramp from room temperature to 1000°C

in 15 seconds. This advantage is important for reducing the surface roughening problem that comes from significantly different diffusion rates of the surface and bulk material (Wee *et al.* (1997)). Annealing is performed in an inert environment (Here, Helium was used) thus preventing oxidation of the samples.

As schematically shown in Fig. 3.1, the RTA's primary components consist of a vacuum chamber, graphite carbon strip elements and an optical pyrometer. The optical pyrometer monitors the radiated heat thereby accurately monitoring the temperature of the graphite strips. It is also supplemented by a standard K-type thermocouple that measures the ambient temperature of the electric terminals, a vacuum pump to provide a vacuum environment, an inert gas feed (nitrogen or helium, in this case, helium) and a water cooling system to prevent overheating of the chamber. See Wee *et al.* (1997) for further description of the RTA.

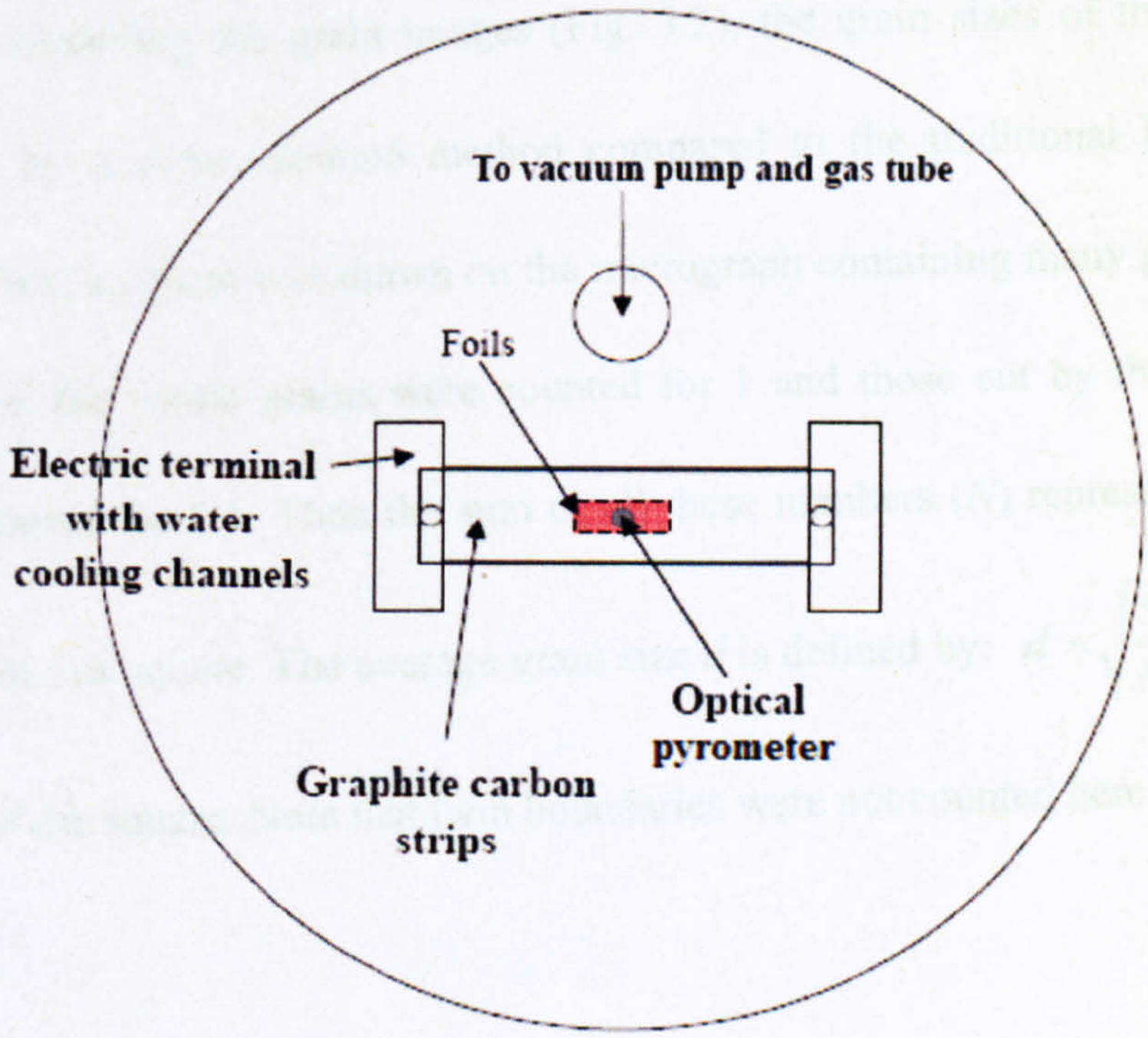

Figure 3.1 Schematic of Main components of the RTA, redraw from Moreau's report (2004).

3.2.2 Grain size characterisation

The grain size and structure resulted from various annealing conditions was revealed by etching the foils. The etching of the grain boundaries was carried out in a mixture of acetic (99.9%) and nitric acid (99.9%) at volume proportion five to one (Haynes 1984). The mixtures were freshly prepared and the foils were immersed in the solution for a short period, less than 2 minutes (Empirically, thicker ones require slightly longer time), until the grain boundaries could be revealed. After thorough washing in distilled water followed by acetone, the grain size was measured by optical microscopy (Leica DMLM equipped with a camera). Fig. 3.2 shows typical examples of grain images. Clear images were observed after proper etching.

The grain size does not change according to the etching time, but as this etching process damages the foil, the actual foils used for bending were not etched.

After obtaining the grain images (Fig. 3.2), the grain sizes of the foils were calculated by a more accurate method compared to the traditional line-intercept method. First, a square was drawn on the micrograph containing many grains. Inside this square, the whole grains were counted for 1 and those cut by the side of the square counted for 0.5. Then the sum of all these numbers (N) represents the grain numbers in this square. The average grain size d is defined by: $d = \sqrt{\frac{S}{N}}$, where S is the area of the square. Note that twin boundaries were not counted here.

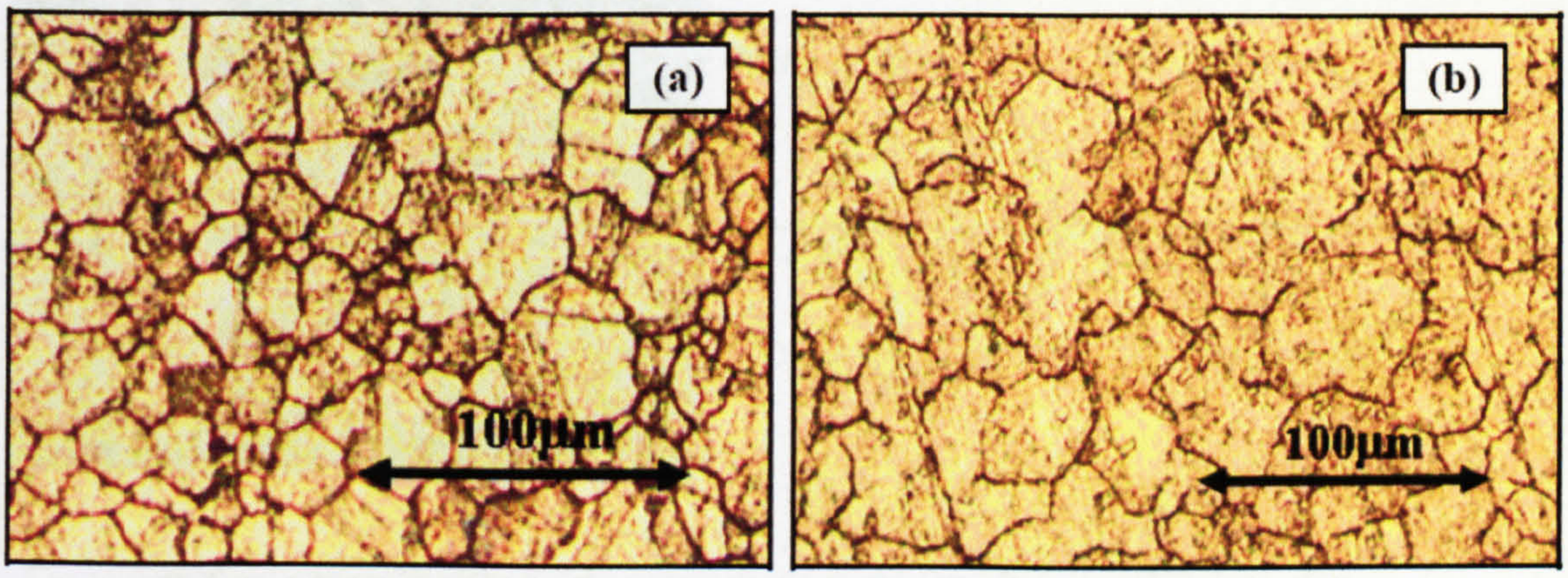

Figure 3.2 Optical microstructure pictures of Ni foils after etching: different thickness foils have the similar grain size $d \sim 30\mu m$. (a) 10μm foil thickness with grain size $d = 22\mu m$; (b) 125μm foil thickness with grain size $d = 27\mu m$.

In addition, the microstructure of the cross section of foils was characterized in the scanning electron microscope (SEM) (Carl Zeiss Supra-40 FEGSEM) by electron backscattered diffraction (EBSD, HKL5, Oxford Instruments, UK). This was done by my colleague X. Hou at the National Physics Laboratory (NPL). Typical examples of EBSD images are shown in Figs.3.3-3.5. The pole figures obtained by EBSD are shown besides the image figures (Figs.3.3-3.5).

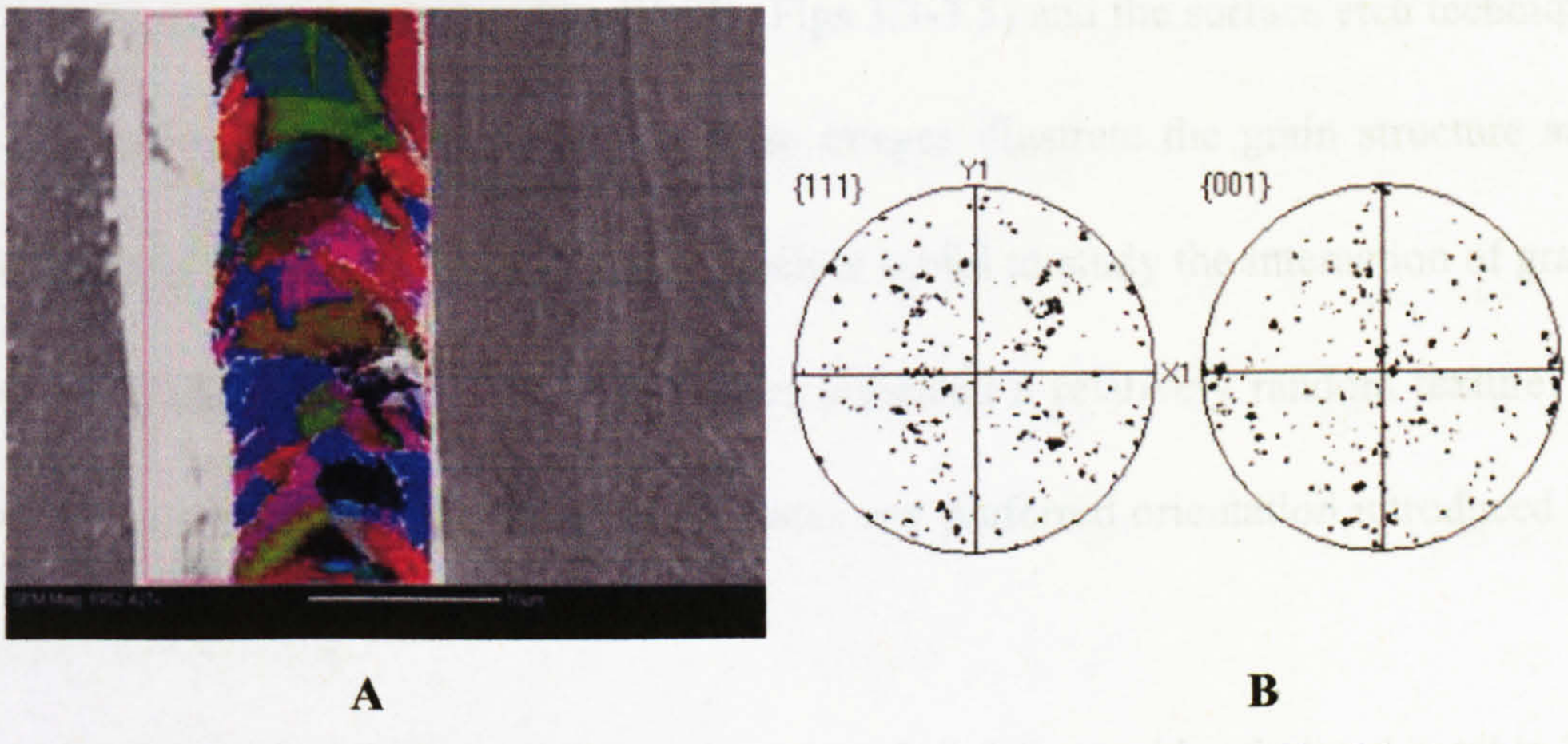

A B

Figure 3.3 (A) EBSD of the cross section of a 10μm nickel foil with 6μm average grain size; **(B)** Pole figures illustrating the texture in the 10μm foil.

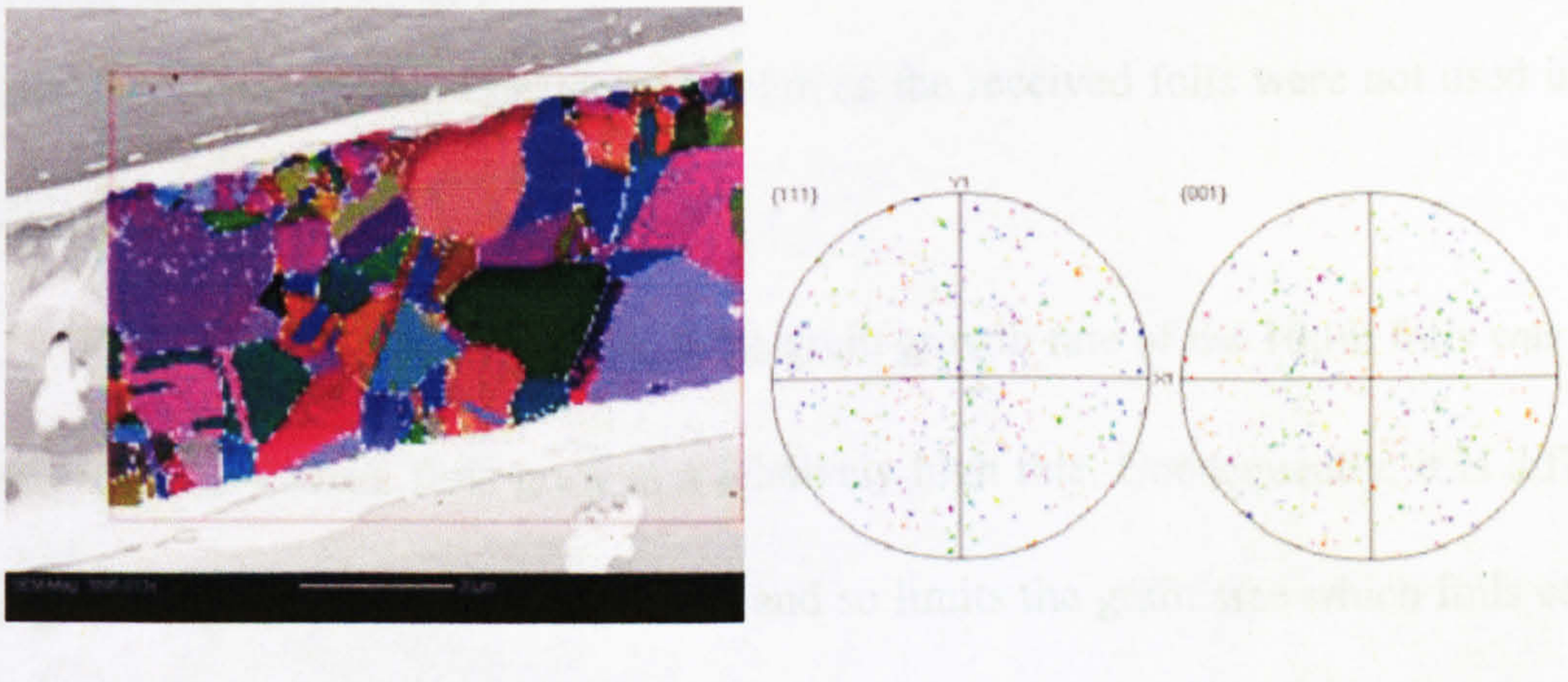

A B

Figure 3.4 (A) EBSD of the cross section of a 50μm nickel foil with 30μm average grain size; (B) Pole figures illustrating the texture in the 50μm foil.

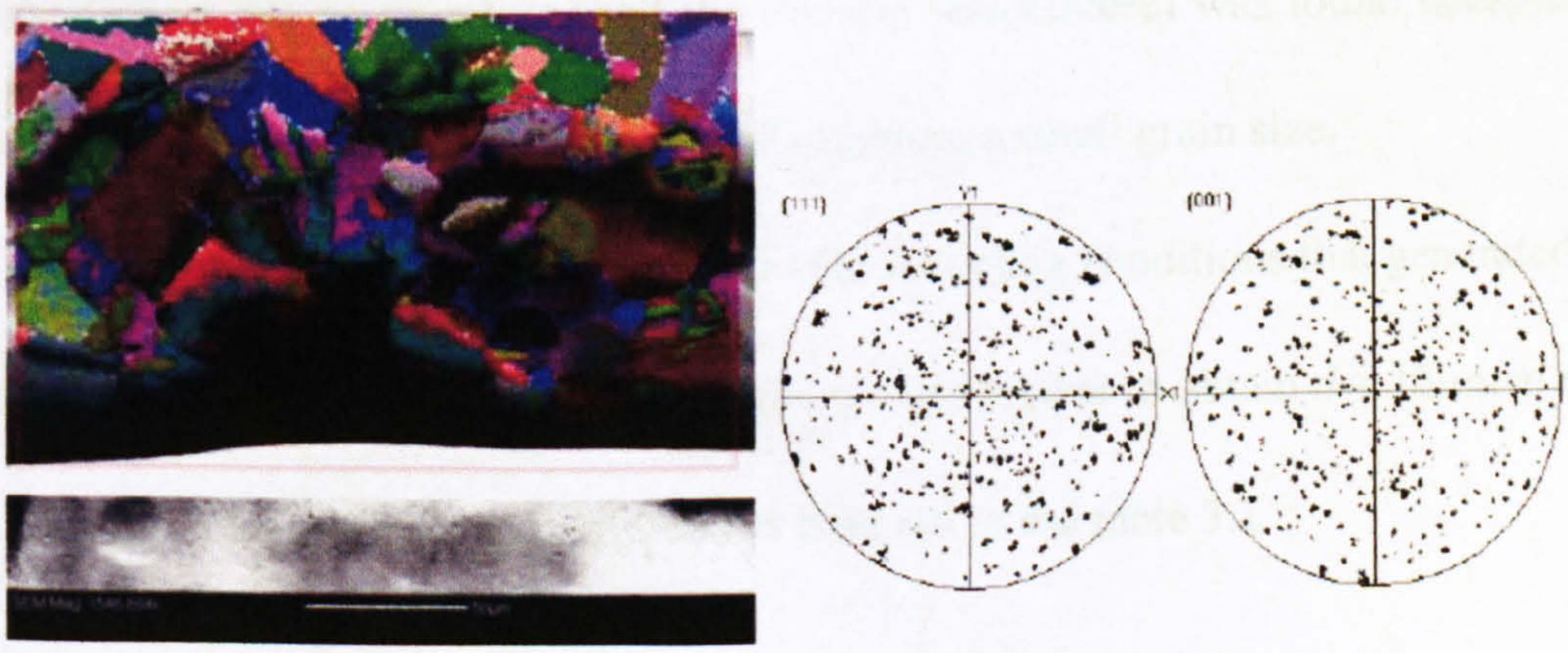

A B

Figure 3.5 (A) EBSD of the cross section of a 125μm nickel foil with 27μm average grain size; (B) Pole figures illustrating the texture in the 125μm foil.

The grain sizes measured by EBSD (Figs.3.3-3.5) and the surface etch technique (Fig.3.2) were consistent. Moreover, these images illustrate the grain structure and assembly in the cross section of foils, which is useful to study the interaction of grain and thickness size effect. The pole figures indicated a relatively random texture. In other words, the annealing process eliminates any preferred orientation introduced by previous processing.

The summary of the metallurgical results of all foils used is tabulated in table 3.1. It can be noted that there is no measurements of grain size for foils as received (in table 3.1). This was not considered useful, as the received foils were not used in the experiments.

Annealing the foils showed that the grain growth rate of the 10μm foils was very low, whereas 125μm foils grew at a relatively high rate. Consequently, it is difficult to grow large grains for the 10μm foil and so limits the grain size which foils can be grown. Thus, the grain sizes of the three different thickness foils were grown to have the same grain size as the initial grain size of the 125μm foil. For 125μm foils, annealing at low temperature (half the melting temperature) was found necessary to get rid of the work hardening effect, while keeping a small grain size.

Although it was not possible to choose annealing conditions that generated the same grain sizes, d, for each foil thickness, it was feasible to obtain $d \approx 30\mu m$ at each thickness. They have been highlighted as bold red in the table 3.1.

3.2.3 Surface roughness characterisation

The surface roughness was measured using a Dektak 3ST surface profilometer. Fig.3.6 shows a typical example of surface profile for a 50μm thickness nickel foil with grain size d = 14μm. Half of the difference between each neighbouring peak (e.g., $(h_1\text{-}h_2)/2$ shown in the Fig.3.6) is defined as the roughness of the foil at certain scan position (e.g., $(h_1\text{-}h_2)/2$ shown in the Fig.3.6, is defined as the roughness for scan length at about 410μm). The average roughness is calculated by averaging the roughness through a certain scan length (in this study, typically through 500μm)

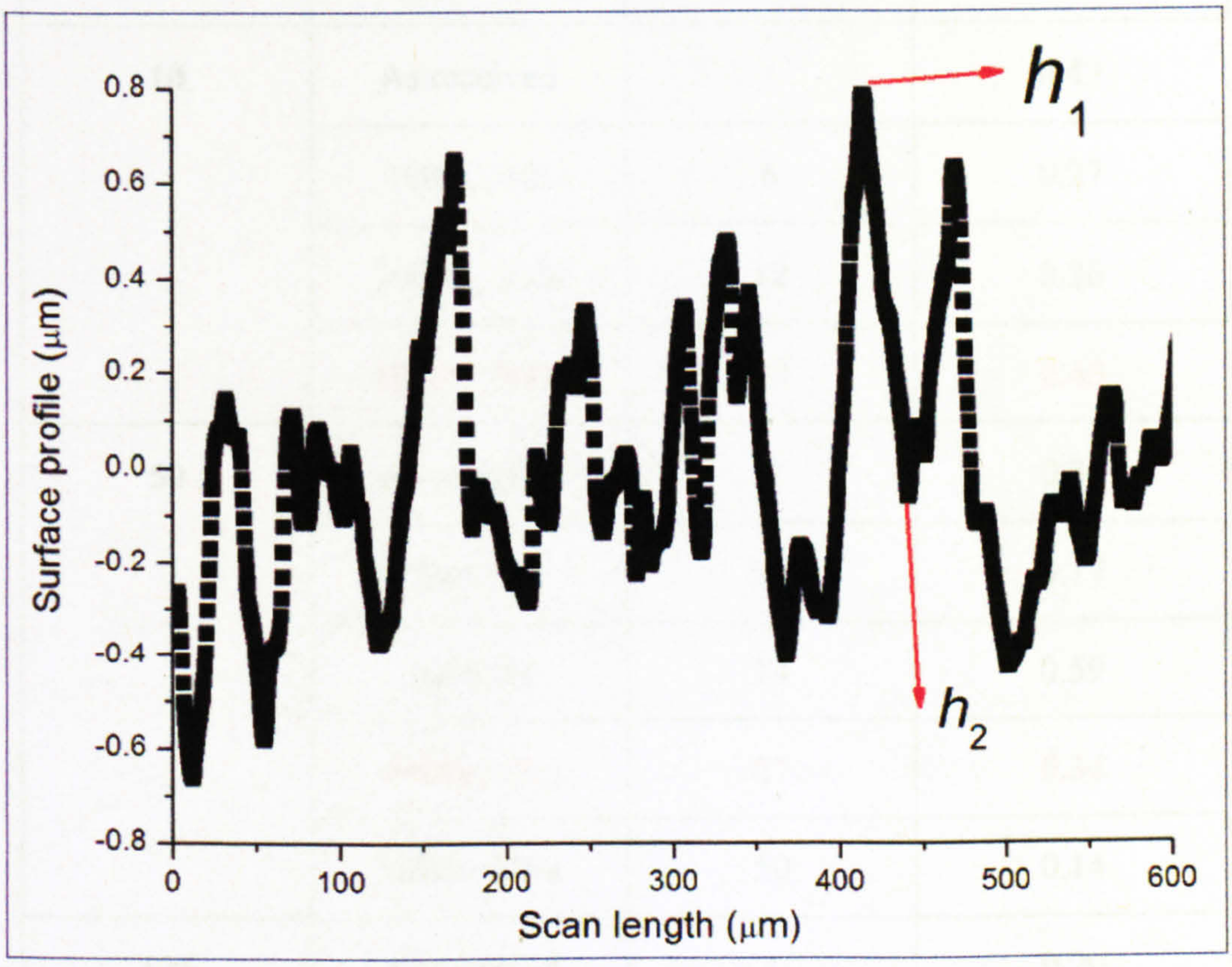

Figure 3.6 A typical surface profile (using a Dektak 3ST) for a 50μm foil, with grain size d = 14μm. The average surface roughness is about 0.6μm.

The surface roughness characterisation results are tabulated in table 3.1. Roughness is relatively small compared to the foil thickness (less than 5%). Also, it

can be observed that the roughness is slightly decreased for most foils after annealing. In conclusion, the roughness will not have much effect on the bending results.

Table 3.1 Annealing conditions and corresponding grain sizes of nickel foils. Bold red values were the chosen annealing conditions to obtain consistent grain sizes for h = 10, 50 and 125μm.

Thickness, *h* / μm	**Annealing Conditions (Temp & time)**	**Grain size, *d* / μm**	**Average Surface roughness / μm**
10	As received	/	0.42
	1000C, 10s	6	0.27
	1000C, 300s	12	0.36
	1000C, 900s	**22**	**0.45**
50	As received	/	0.31
	700c 30s	5.5	0.17
	1000, 5s	14	0.59
	1000c, 15s	**27**	**0.34**
	1000c, 120s	50	0.14
125	As received	/	0.20
	700c, 30s	**30**	**0.09**
	1000c, 5s	85	0.03
	1000c, 120s	220	0.04

3.3 Bending techniques

The load-unload technique was carried out, which is familiar in mechanical testing of materials. Flexure on thin metal foils was applied, as schematically shown in Fig.3.7.

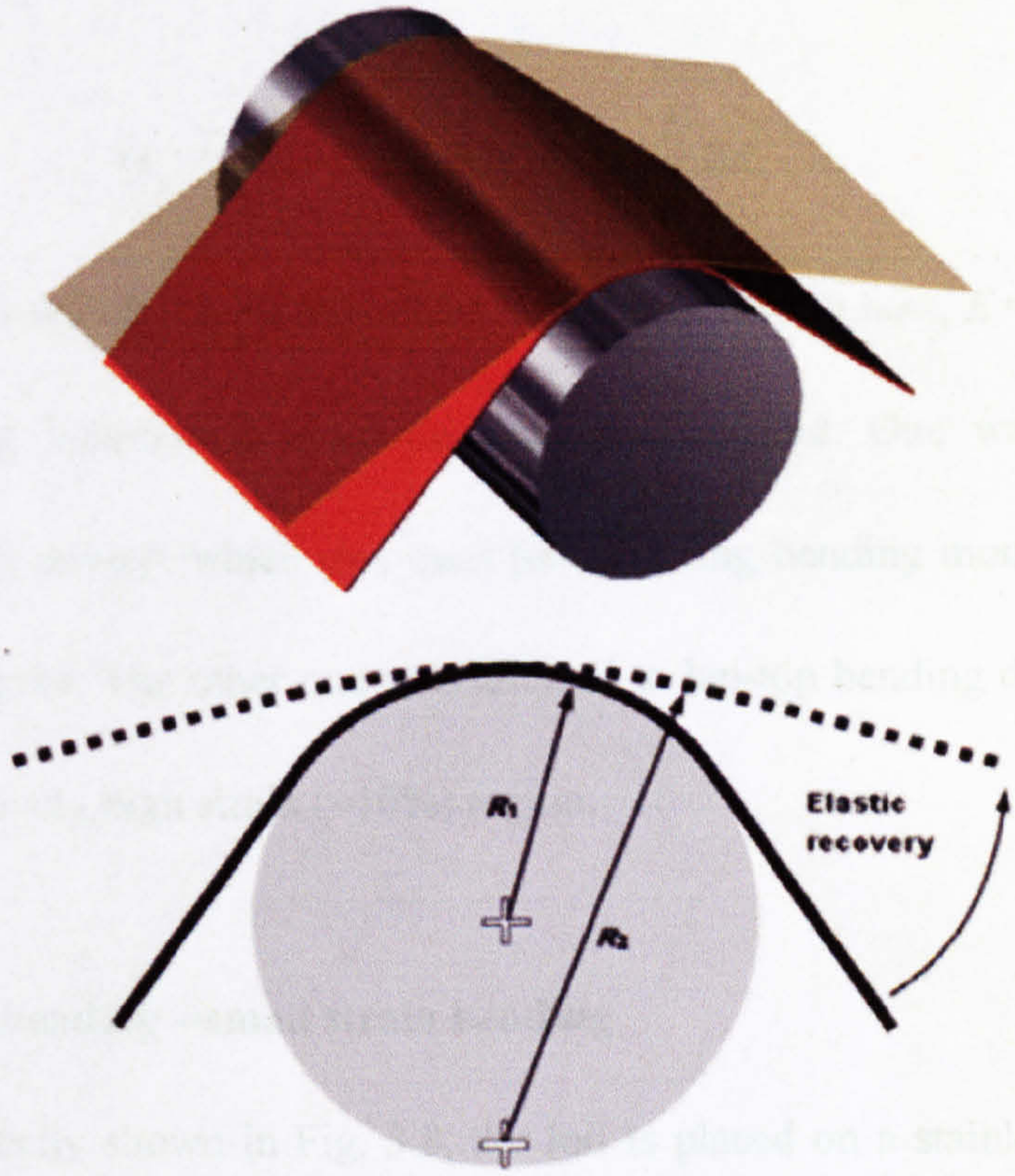

Figure 3.7 Schematic plot of the load-unload bending method. The solid line represents the foil loaded to conform to the mandrel; the dotted line represents the foil after elastic recovery to the unloaded state. Radii R_1 and R_2 are measured by optical, non-contact methods.

The principle of the design is to bend a foil of thickness h and width w, to a prescribed radius of curvature R_1 and this introduces a known strain, which is partly elastic and partly plastic, and which at the surface is

$$\varepsilon_s = \frac{h}{2R_1} \tag{3.1}$$

The foil is then unloaded, and it relaxes elastically to a larger, permanent radius of curvature R_2 (Fig. 3.7). The increase in radius provides a determination of the bending moment M at the radius R_1. At the radius R_2 the bending moment is zero. At the radius R_1 simple elastic beam theory gives, for the bending moment normalised by wh^2

$$M_n = \frac{M}{wh^2} = \frac{Eh}{12}\left(\frac{1}{R_1} - \frac{1}{R_2}\right) = \frac{E}{6}\Delta\varepsilon_s \qquad (3.2)$$

where E is the relevant elastic modulus for a wide beam (for Ni here, E = 220GPa).

Two bending instruments were designed and applied. One was named as four-point bending device, which was used for obtaining bending moment at small strain (~0.2%) region. The other one was referred to lap-top bending device, which was used for relatively high strain (~10%) region.

3.3.1 Four-point bending --small strain bending

As schematically shown in Fig. 3.8, the foil is placed on a stainless steel shim and constrained by two weighted rollers at both ends. A screw device drives a wedge that lifts the central rollers thereby setting the curvature κ_1 (loading curvature $\kappa_1 = 1/R_1$, where the radius of loading curvature is R_1) in the range 0 – 1cm^{-1}. One of the weighted rollers is then removed, unloading the foil, and allowing it to relax elastically to a smaller, permanent curvature, κ_2 (unloading curvature $\kappa_2 = 1/R_2$, where the radius of the unloaded foil is R_2). The numerical value of curvatures κ are measured by a non-contact optical profilometer (OTM3 from Wolf & Beck Sensorik, Germany) to scan the top of the foil (Fig. 3.8 (A)).

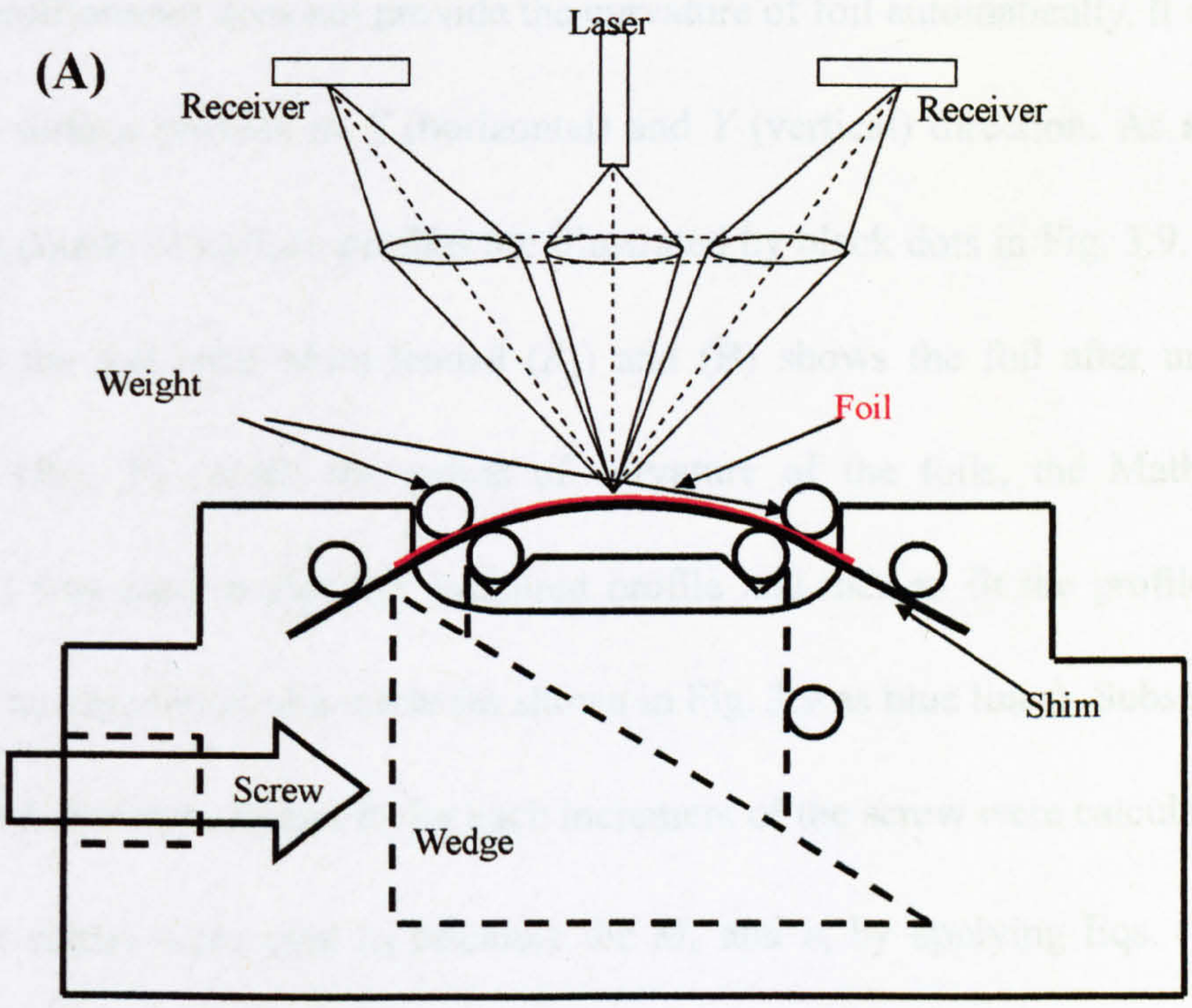

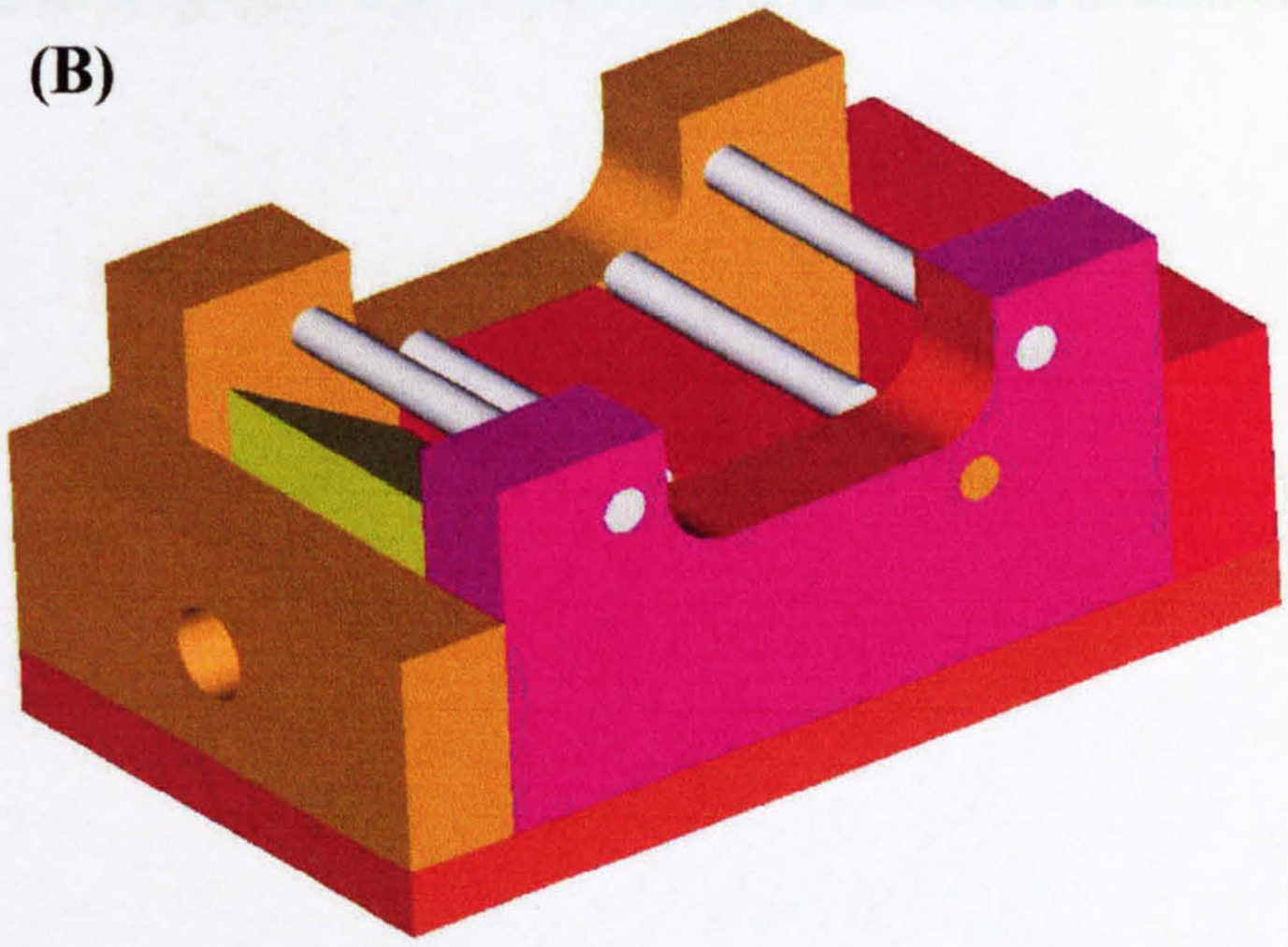

Figure 3.8 (A) Schematic plot of four-point bending machine, which is used for small strain (about 0-2%) bending. The foil is laid on a shim that is in a 4-point bend and constrained by two weighted rollers at both ends. The screw drives a wedge that lifts the middle two rollers. This increases the 4-point bend and thus decreases the radius of curvature on the foil. (B) The 3D isometric view of the four-point bend machine. Foil, shim and weighted bars are not shown for clarity. (Designed by Prof. Dunstan and redrawn from Dr. P'ng's PhD thesis)

The profilometer does not provide the curvature of foil automatically. It can only record the surface profiles in X (horizontal) and Y (vertical) direction. As a typical example, a couple of surface profiles are illustrated by black dots in Fig. 3.9. Fig. 3.9 (A) shows the foil with when loaded (R_1) and (B) shows the foil after unloading elastically (R_2). To obtain the radius of curvature of the foils, the Mathematica version 4.2 was used to plot the measured profile and then to fit the profile with a mathematical simulation of a circle (as shown in Fig. 3.9 as blue lines). Subsequently, the radius of curvature R_1 and R_2 for each increment of the screw were calculated.

These values were used to calculate the M_n and ε_s by applying Eqs. (3.1) and (3.2) respectively. Results will be presented and discussed in section 3.4.

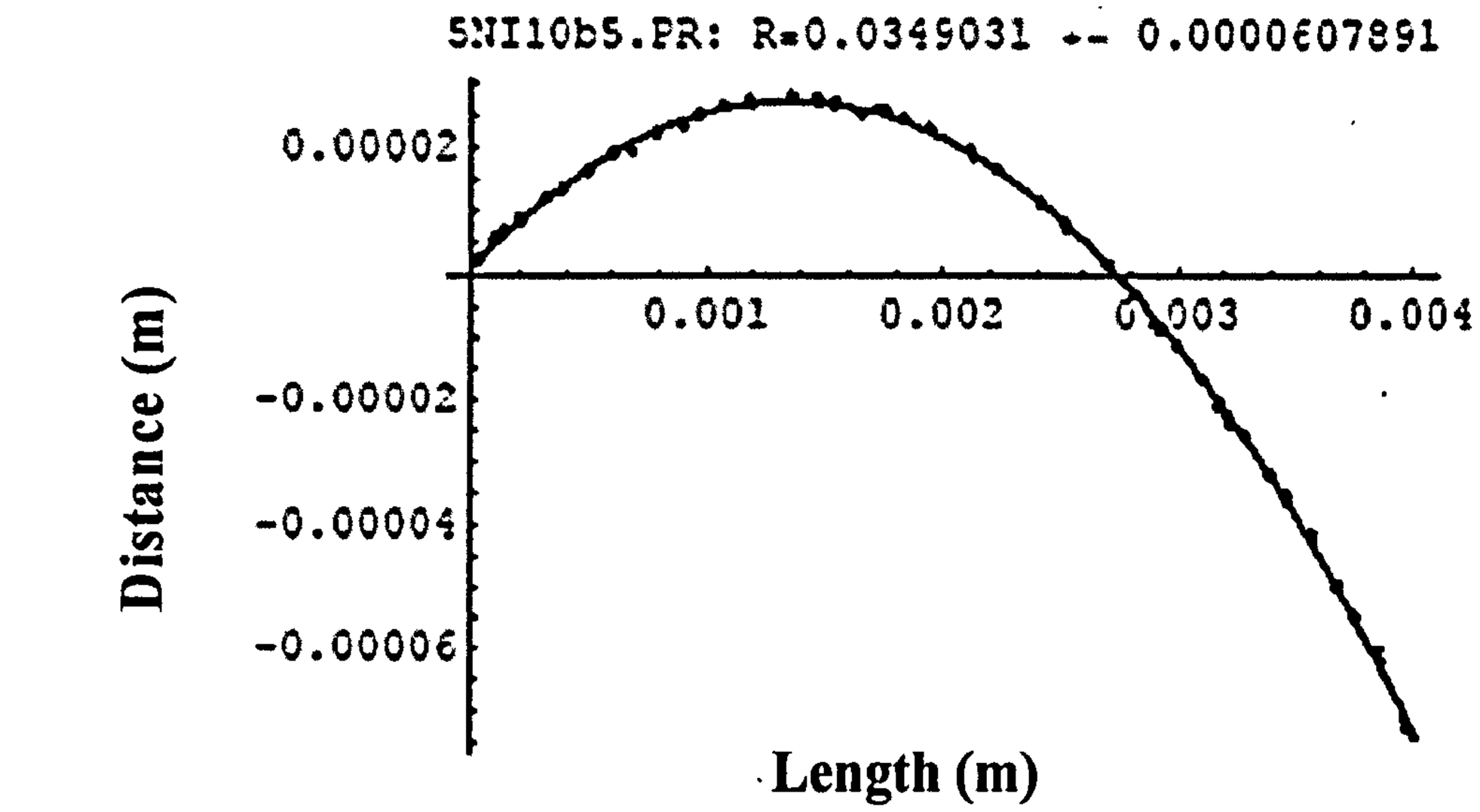

(A)

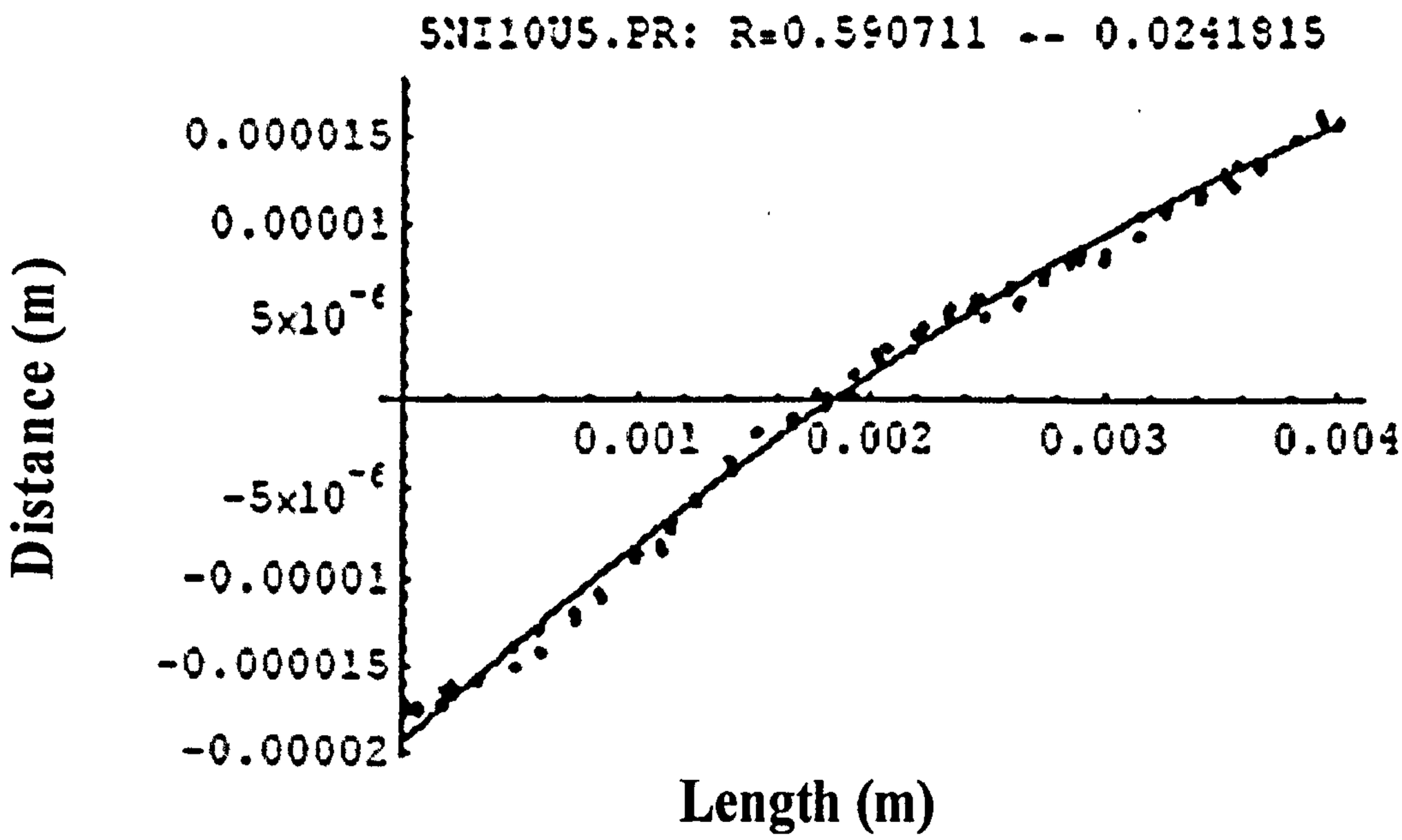

(B)

Figure 3.9 Typical examples of surface profiles for foils exported by Mathematica 4.2. Black dots are recorded surface profile data from optical profilometer. The blue line is the mathematical simulation as a circle for the surface profile. (A) A 10μm foil is bent and corresponds to $R_1 \approx 0.035$m (B) The foil is unbent and corresponds to $R_2 \approx 0.59$m.

3.3.2 Lap-top bending--high strain bending

Apparatus shown in Fig. 3.10 provided for the foils to be bent by a metal plate (yellow card shown in Fig.3.10) around a mandrel (drill blanks) of radius from 3mm to 100μm, covering the range of curvature κ from $3cm^{-1}$ to $100cm^{-1}$. In this apparatus, a laser beam was reflected from the straight part of the foil beyond the mandrel, and the deflection of the laser beam was used to deduce the loaded and unloaded curvature κ of the foil. The tracks of laser beam were recorded on a chart roll.

For each size mandrel, foils were bent to a series of angles θ_1 (Fig. 3.11) to minimize (average out) the errors. The angles were controlled by stoppers on the working bench.

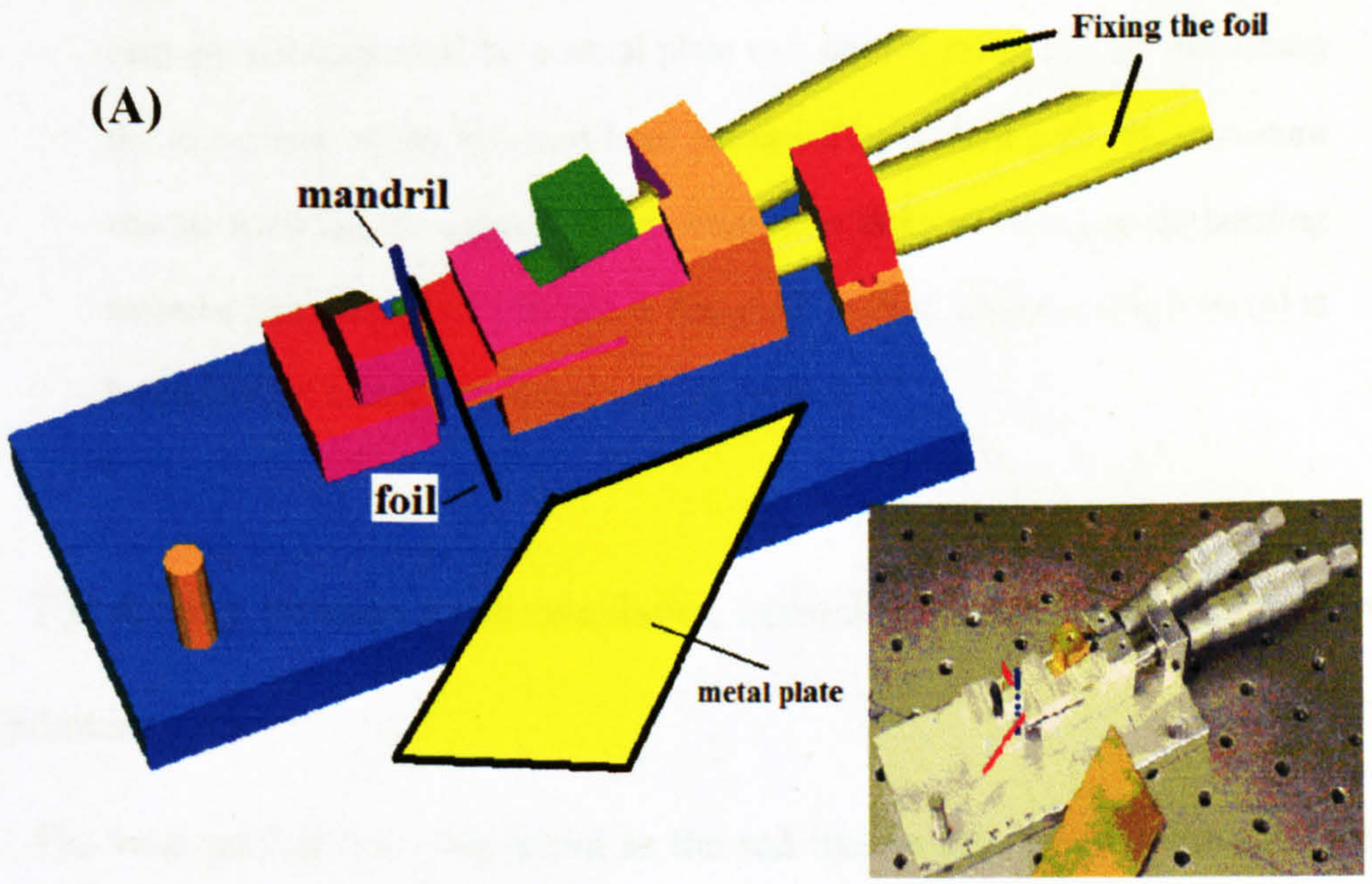

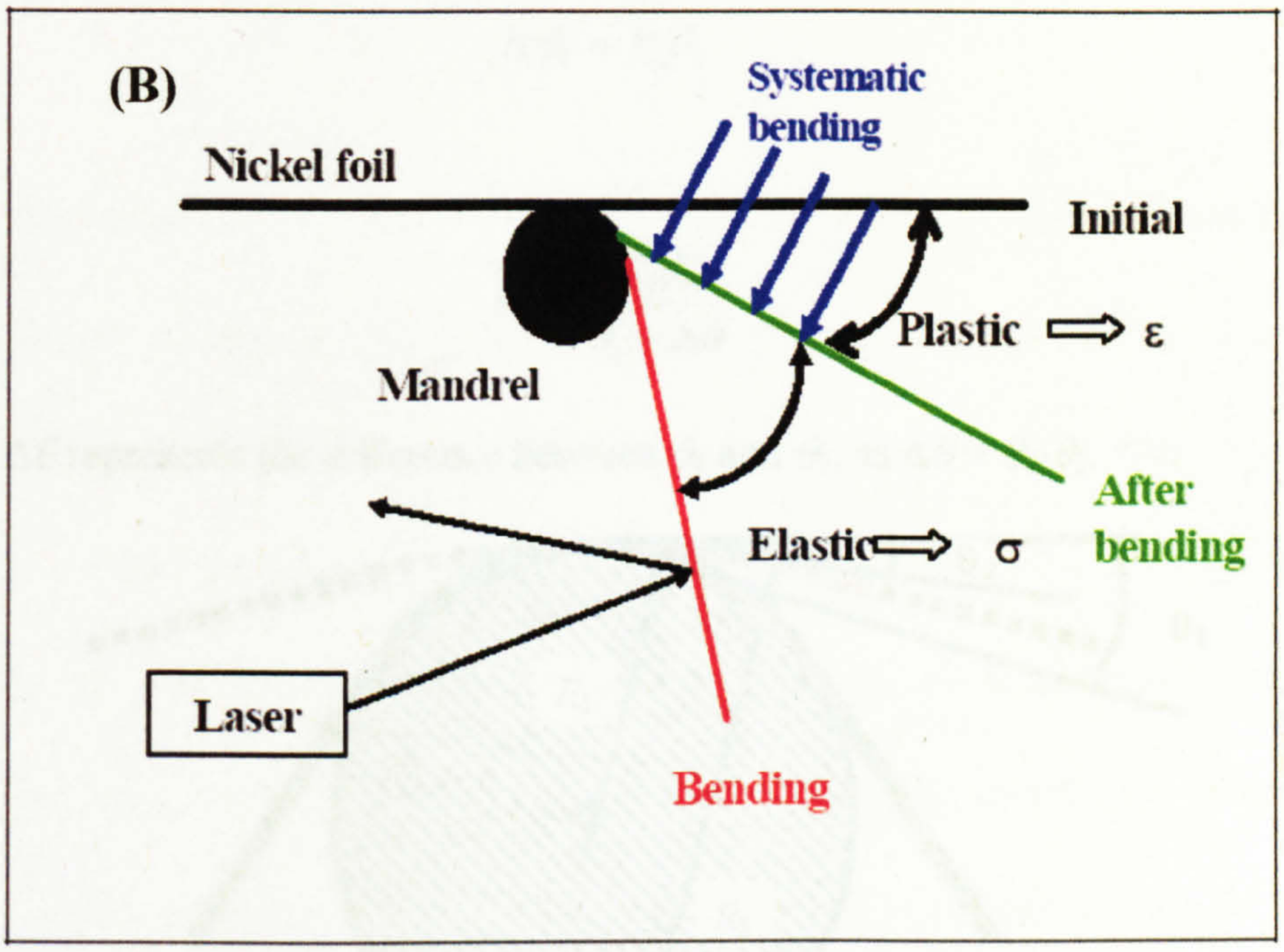

Figure 3.10 (A) Schematic diagram of lap-top bending. The foil, mandrel and stopper are illustrated. Laser beam and chart roll are not included in this picture. The picture of the equipment is inserted at the bottom right corner. (B) Schematic plot of working principle of the equipment, which is used to measure flexure behaviour at relatively high strain (up to 10%). The foil is bent around a mandrel by a metal plate to a known radius R_1. By measuring the movement of the reflected laser (recorded by a chart roll), the curvature change from load to unload can be obtained in order to calculate the bending moment from Eq. (3.2). (Device is designed by Prof. Dunstan; Fig.3.10 (a) is helped by Dr. Gannaway, who built this device)

The detailed procedure and calculation method for obtaining M_n and ε_s is shown as following.

The bent part of foil (illustrated as the red line in Fig. 3.11) is the same before and after bending, and it is possible to calculate the arc of bent part of the foil (highlighted as red in Fig.3.11) by using radius times centre angle. So,

$$R_1\theta_1 = R_2\theta_2 \tag{3.3}$$

Then,

$$R_2 = \frac{R_1\theta_1}{\theta_1 - \Delta\theta} \tag{3.4}$$

where $\Delta\theta$ represents the difference between θ_1 and θ_2, as $\Delta\theta = \theta_1 - \theta_2$.

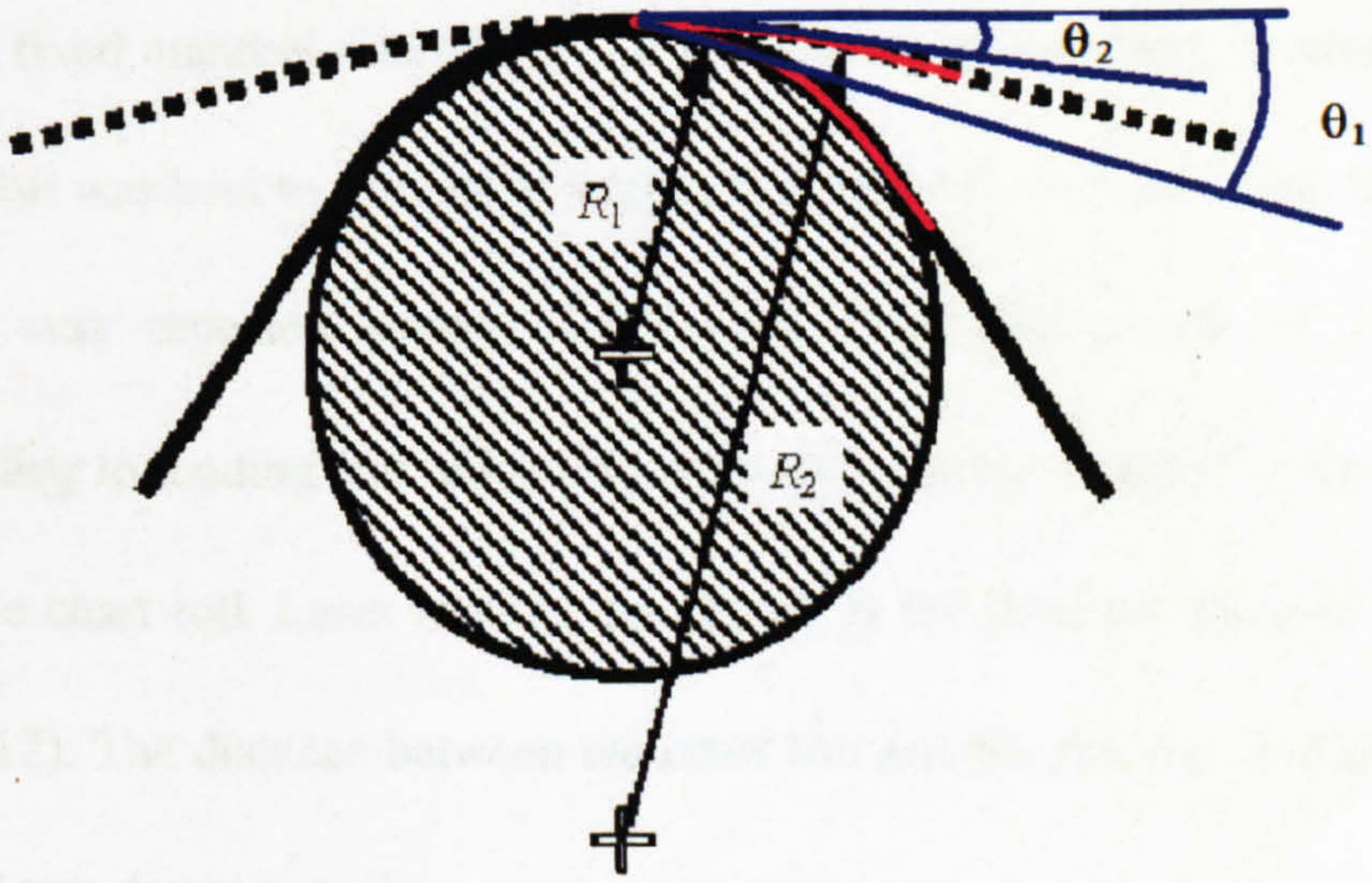

Figure 3.11 Schematic plot of lap-top bending measurement. Foil is bent to a certain angle θ_1 around a mandrel with radius R_1 and released to a permanent radius R_2, with angle θ_2. The red lines illustrate the bent part of foil.

The normalised moment, M_n, is calculated by substituting Eq. (3.4) into (3.2):

$$M_n = \frac{Eh}{12R_1}\left(\frac{\Delta\theta}{\theta_1}\right) \tag{3.5}$$

Since $\Delta\theta$ is relatively small, mathematically,

$$\Delta\theta = \frac{1}{2}tg^{-1}\frac{l_L}{l_{CF}} \approx \frac{l_L}{2l_{CF}} \tag{3.6}$$

where l_L is the average moving distance of the laser beam before and after bending; l_{CF} is the distance between chart roll and foil. For better understanding, these parameters are illustrated in Fig.3.12. Then, substitute Eq. (3.6) into (3.5),

$$M_n = \frac{Eh}{12R_1}\left(\frac{l_L}{2l_{CF}\theta_1}\right) \tag{3.7}$$

where the distance l_L is calculated from the difference between the loading and release point on the chart roll. R_1 is the mandrel radius; l_{CF} is measured by ruler; θ_1 is controllable by the stopper on the working bench. Thus, it is able to obtain M_n.

For a fixed mandrel size (R_1), i.e. a fixed strain, to minimize (average out) the error, the foil was bent to a series of angles, θ_1 (Fig 3.11). At each angle, loading and unloading was repeated several times. The deflection points of laser beam corresponding to loading and unloading were recorded as P1 and P2 (Fig.3.12) each time on the chart roll. Laser moving distance l_L is the distance between P1 and P2 (in Fig.3.12). The distance between the chart roll and the foil l_{CF}, is also illustrated in Fig.3.12 two dimensionally.

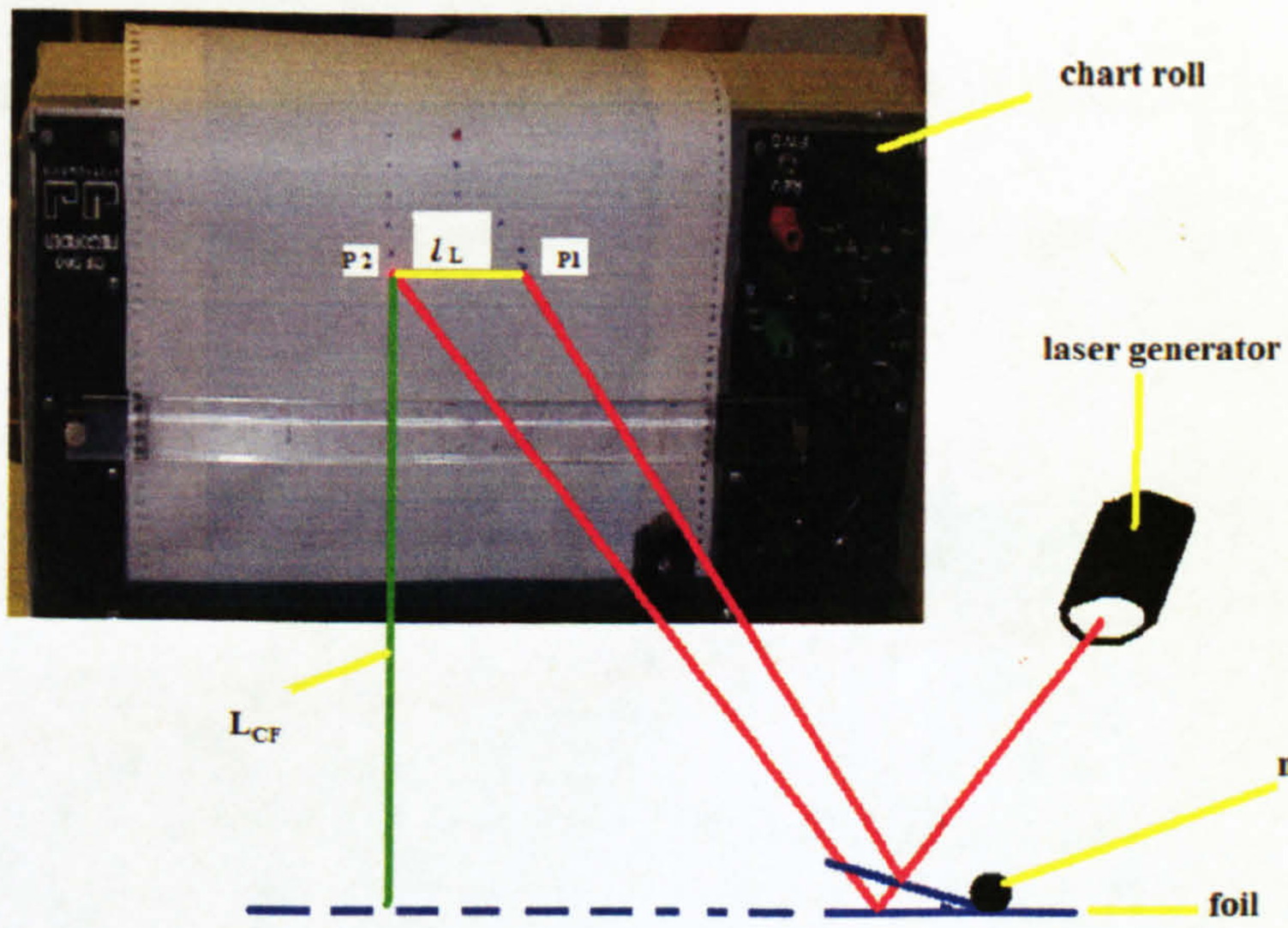

Figure 3.12 Schematic diagram of lab-top bending experiment. Foil was bent to a certain angle; the deflection of laser is recorded on the chart roll as P1. Then the foil is released; the deflection of laser is recorded as P2. The distance between P1 and P2 is l_L. The distance between chart roll and foil is l_{CF}.

Fig. 3.13 shows a typical example of lap-top bending result for a 50μm thickness foil wrapping around a mandrel with radius R_1= 0.5mm. The foil was bent to a series of angles θ_1, from 10° to 60°. Loading points (P1) were recorded as 'circle' and unloading point (P2) were recorded as 'cross' (raw data in Fig 3.13(a)). The distance between P1 and P2 is the laser moving distance l_L. (In addition, the red lines on the chart roll paper are just showing the paper is nearly the end of the current roll). Corresponding results were plotted as l_L against θ_1 in Fig 3.13. Then, a linear function was applied to fit through the data. The term l_L / θ_1 in Eq. (3.7) was obtained as the slope of the straight line. In Fig.3.13, slope is in unit of mm/degree. For calculation in Eq. (3.7), it has to be changed to unit of mm/rad. Subsequently, M_n was obtained from Eq. (3.7) by inputting the obtained value of l_L / θ_1. The surface strain is calculated from Eq. (3.1).

In other words, all the points measured in Fig.3.13 results in a single point in the final stress (bending moment)-strain curve (Figs. 3.14 and 3.15).

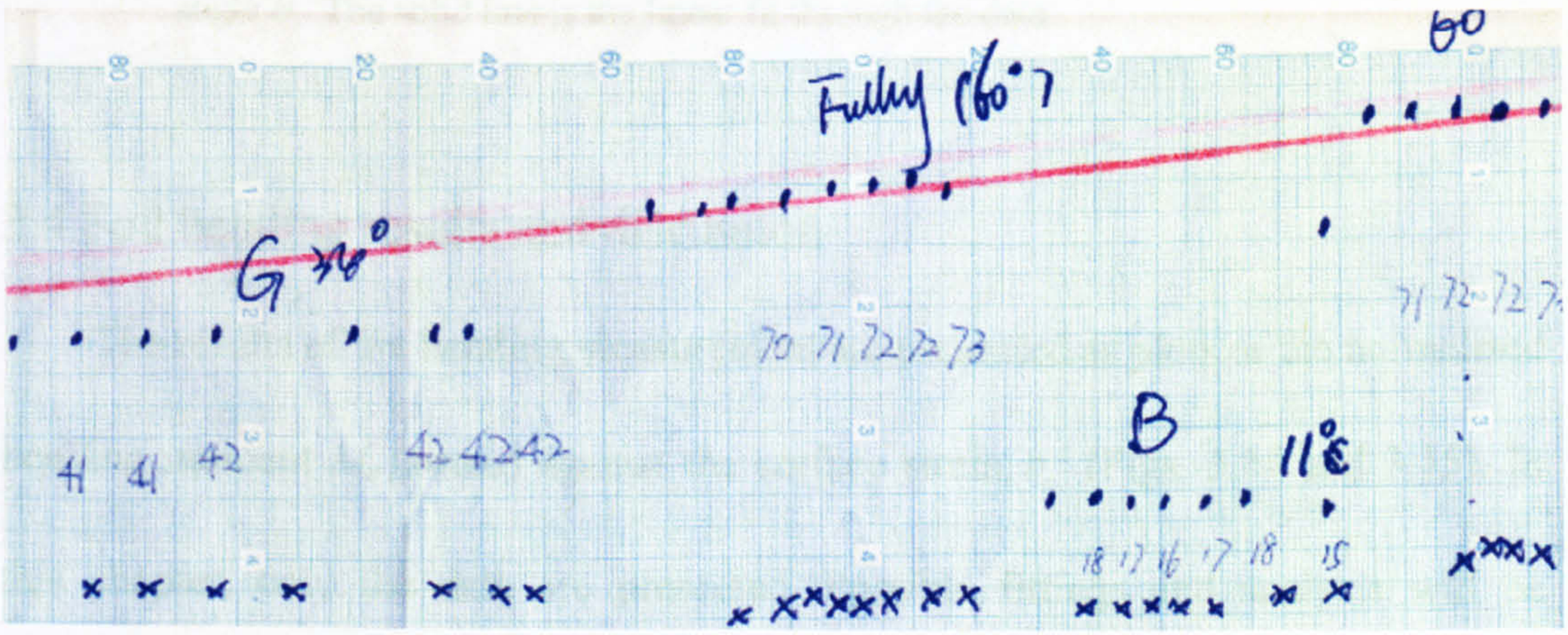

(a)

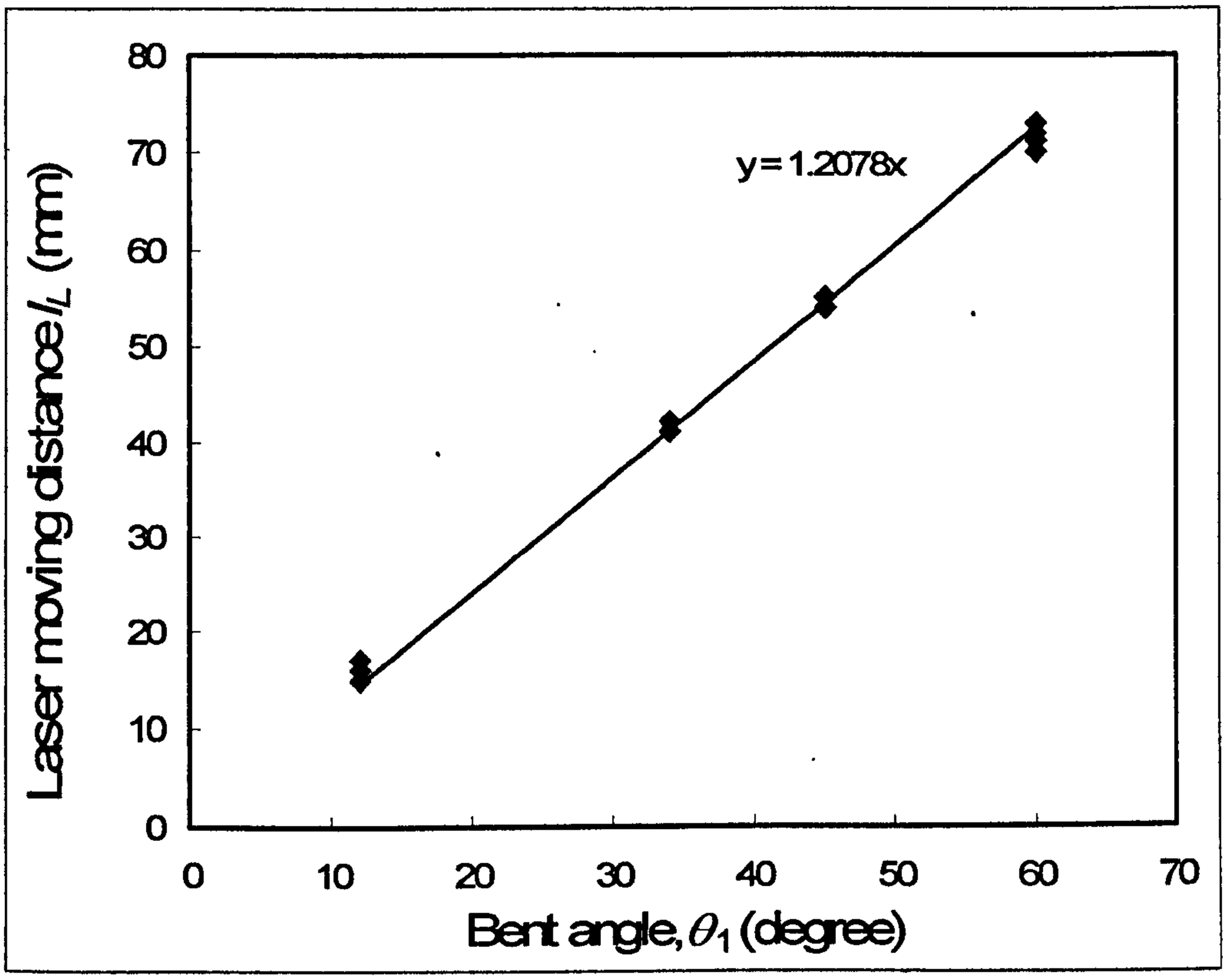

(b)

Figure 3.13 A 50μm foil wrapped around a mandrel with radius R_1 = 0.5mm, was bent to a series of angles θ_1 ranging from 10° to 60°. (a) Part of raw data recorded on the chart roll. Loading points (P1) were recorded as 'circle'; unloading points (P2) were recorded as 'cross'. The distance between P1 and P2 is laser moving distance l_L. (b) Corresponding l_L was plotted against bent angle θ_1. The solid line is the linear fit through the data.

3.4 Foil bending results and discussion

The results of the bending measurement are presented as plots of the normalised bending moment M_n (stress) against the surface strain, ε_s (Figs. 3.14 and 3.15). In this chapter, only the data are presented. Possible fittings and analysis will be discussed in chapter 5. It can be seen that many more strain points were obtained on the bending stress-strain curves over a wider range of strain and grain size (Figs.

3.14 and 3.15), compared with the existing data obtained by Stölken and Evans (1998).

The results are presented in a manner that highlights the separate dependencies on foil thickness and grain size. Those summarized on Fig. 3.14 are for foils having similar grain size but differing thickness. Whereas, the corresponding results on Fig.3.15 are for foils having the same thickness but four different grain sizes.

Firstly, the thickness size effect is studied by comparing foils having similar grain size ($d \approx 30\mu m$) but different thickness (h = 10, 50 and 125μm) as in Fig.3.14 (a) and (b). In Fig.3.14 (a), the increase of M_n with decreasing thickness is clearly observed. For example, at 0.05 surface strain, the M_n of the 10μm foil is over 140MPa, where the 125μm one has M_n only 40MPa. Also, the slope of the stress-strain curve in the plastic region (e.g. between 0.01 to 0.05 strain) is increased in thinner foils. For 10μm foil, the slope is about 3000MPa, where the 125μm foil has the slope of 600MPa. If the linear work hardening is considered here and the bending work hardening rate is defined as the slope of stress-strain curve in the plastic region, i.e. between 0.01 to 0.05 strain, it is apparent that the work hardening rate is increased with decreasing thickness at fixed grain size. Fig. 3.14(b) highlights the small strain region which is obtained from 4-point bending (Fig.3.8). The clear departure from the theoretical elastic line (yielding) can be observed. If yield is defined as a significant departure from the elastic line, in Fig. 3.14(b), the yield strength is increased as decreasing thickness. Detailed fittings and analysis are presented in chapter 5.

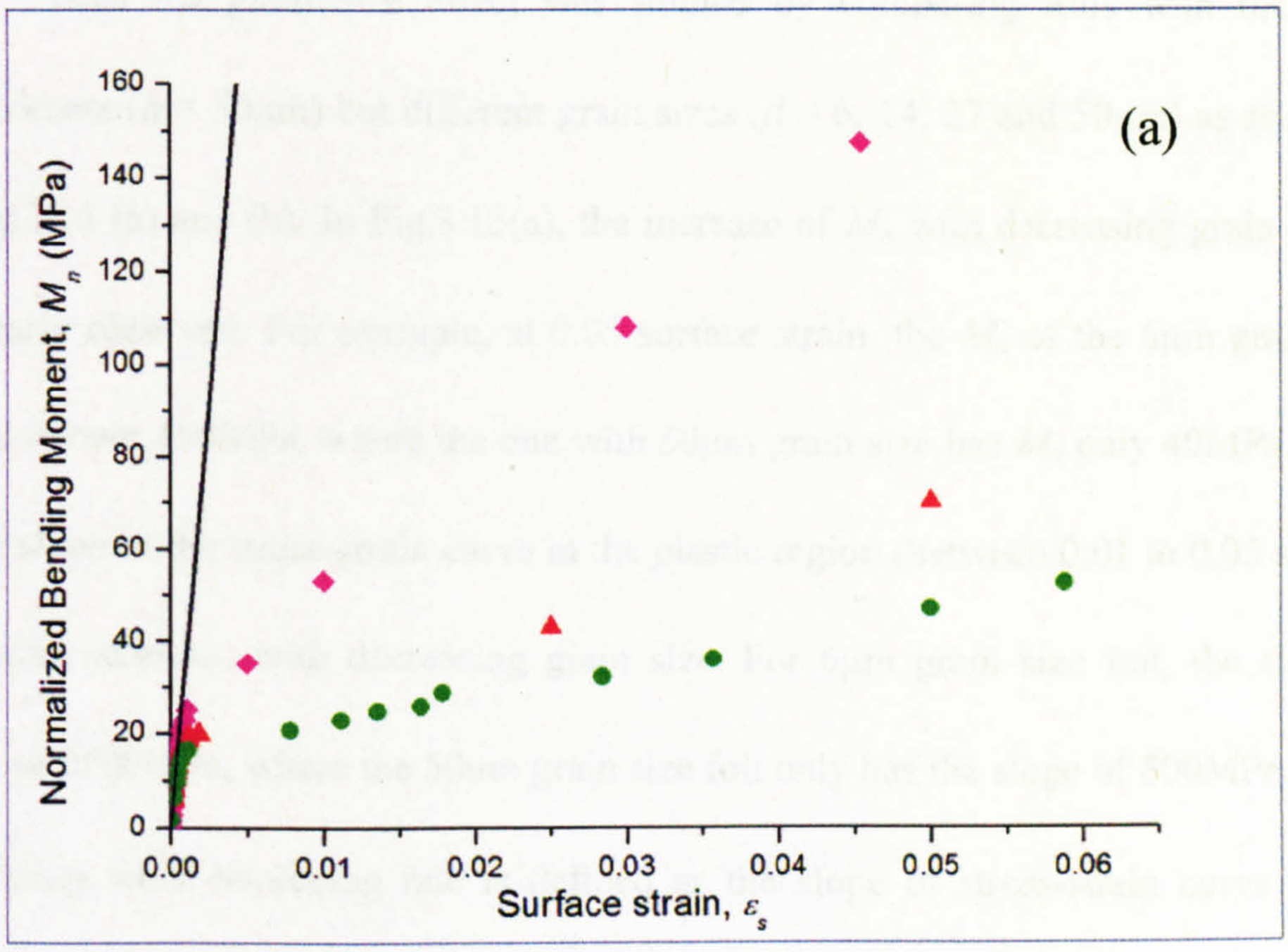

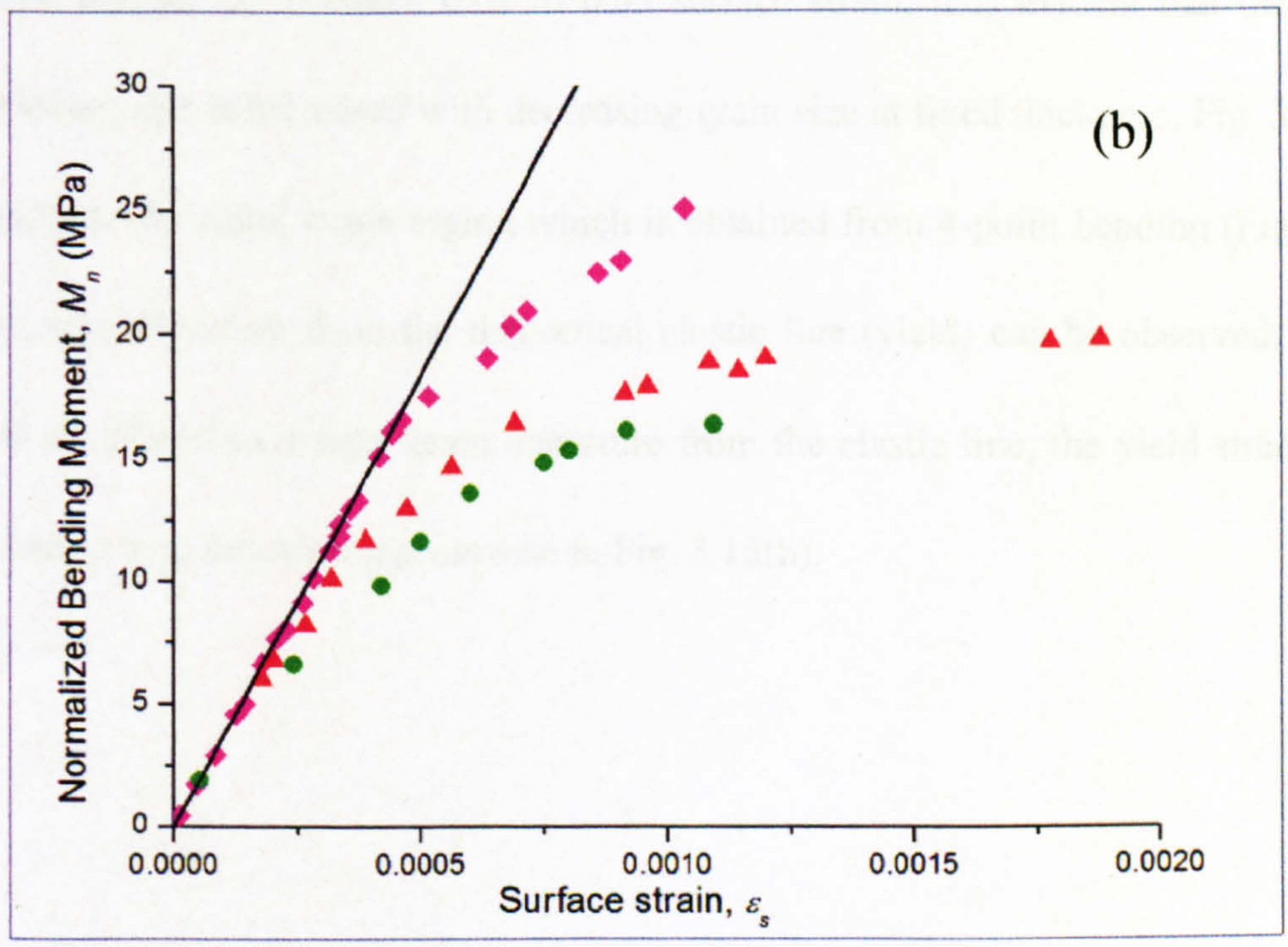

Figure 3.14 Normalised bending moment M_n vs. surface strain ε_s for the foil thicknesses: pink diamond: 10μm, red triangle: 50μm and green sphere: 125μm. Grain sizes are approximately 30μm in all three foils. Solid line is the theoretical elastic line. (a) Full strain range (b) The region at low strain is shown in more detail. Departure from the elastic line is clearly observed and increased in thinner foils.

Then the grain size effect was studied by comparing foils with the same thickness (h = 50μm) but different grain sizes (d = 6, 14, 27 and 50μm) as shown in Fig.3.15 (a) and (b). In Fig.3.15(a), the increase of M_n with decreasing grain size is clearly observed. For example, at 0.05 surface strain, the M_n of the 6μm grain size foil is over 150MPa, where the one with 50μm grain size has M_n only 40MPa. Also, the slope of the stress-strain curve in the plastic region (between 0.01 to 0.05 surface strain) increases with decreasing grain size. For 6μm grain size foil, the slope is about 2500MPa, where the 50μm grain size foil only has the slope of 500MPa. If the bending work hardening rate is defined as the slope of stress-strain curve in the plastic region, i.e. between 0.01 to 0.05 surface strain, it is evident that the work hardening rate is increased with decreasing grain size at fixed thickness. Fig. 3.15(b) highlights the small strain region which is obtained from 4-point bending (Fig. 3.8). The clear departure from the theoretical elastic line (yield) can be observed. If the yield is defined as a significant departure from the elastic line, the yield strength is increased with decreasing grain size in Fig. 3.15(b).

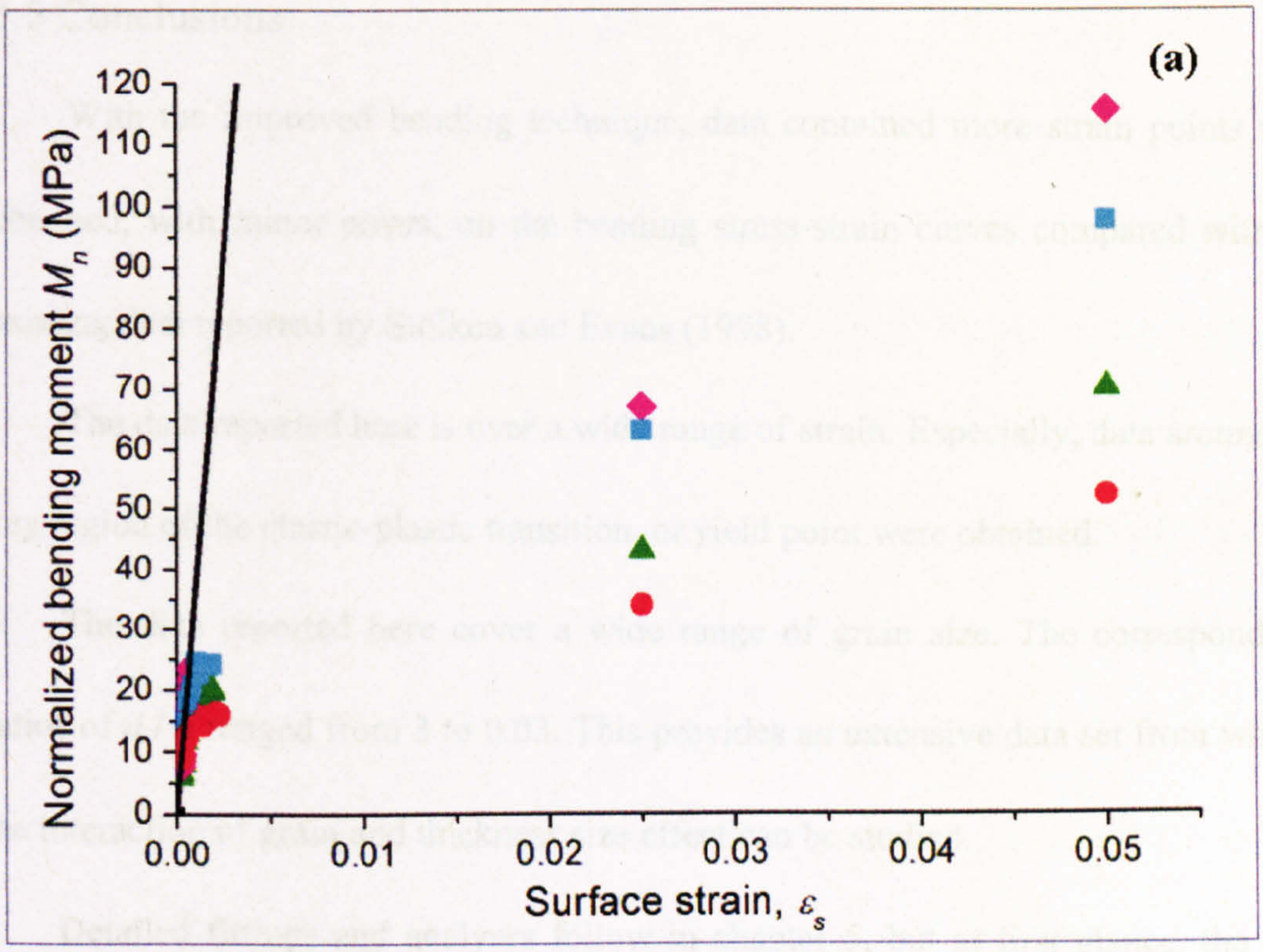

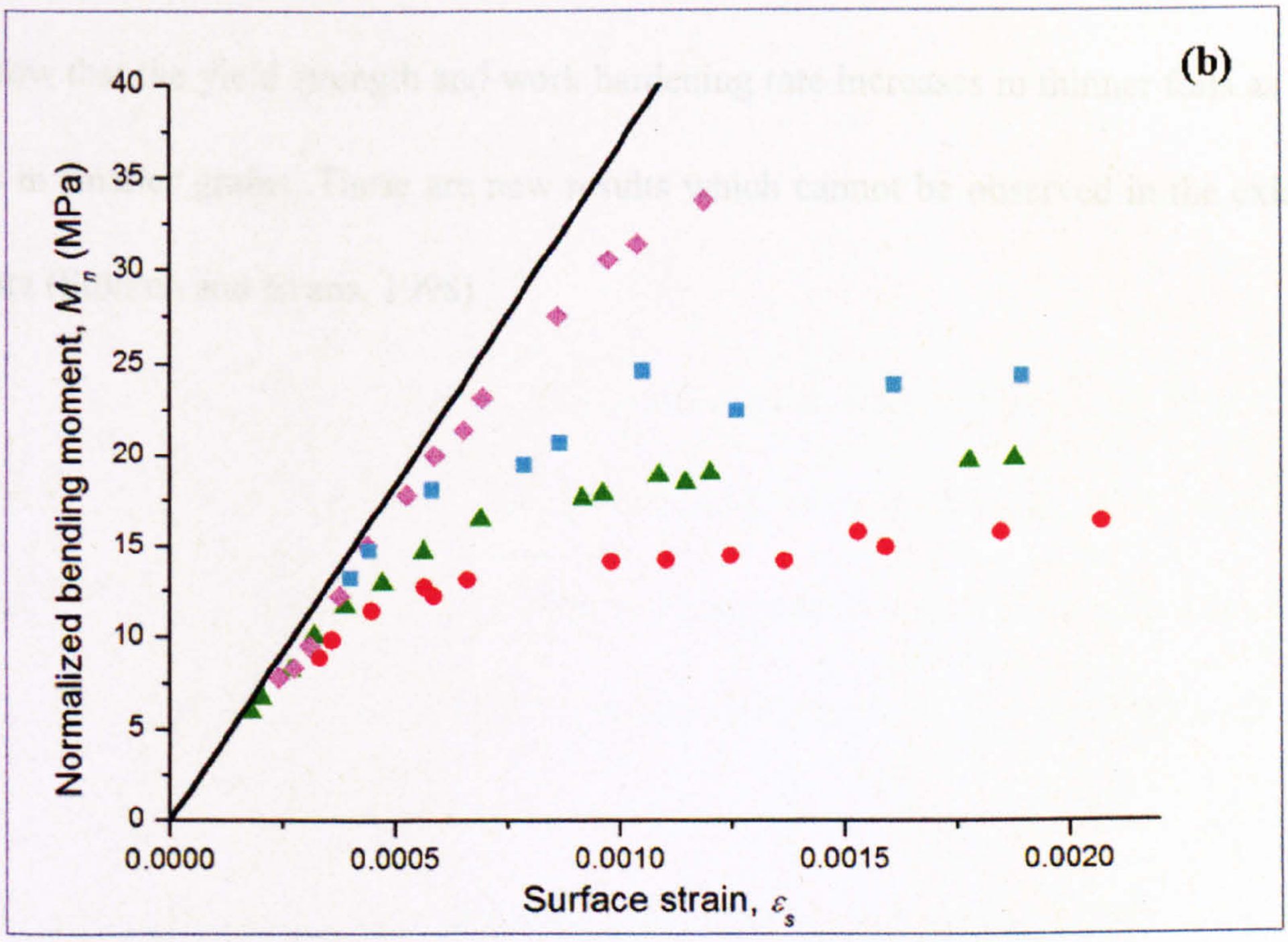

Figure 3.15 M_n Vs. ε_s, for h = 50μm foil with different grain sizes. Pink diamond: d = 5.5μm; blue square: d = 14μm; green triangle: d = 27μm and red circle: d = 50μm. Solid line is the theoretical elastic line. (a) Full range of strain (b) The small strain range is shown in more detail. The departure point from elastic line is observed and increases in smaller grain sizes.

3.5 Conclusions

With the improved bending technique, data contained more strain points were obtained, with minor errors, on the bending stress-strain curves compared with the existing data reported by Stölken and Evans (1998).

The data reported here is over a wide range of strain. Especially, data around the key region of the elastic-plastic transition, or yield point were obtained.

The data reported here cover a wide range of grain size. The corresponding ratios of d / h ranged from 3 to 0.03. This provides an extensive data set from which the interaction of grain and thickness size effect can be studied.

Detailed fittings and analyses follow in chapter 5, but at first glance, the data show that the yield strength and work hardening rate increases in thinner foils as well as in smaller grains. These are new results which cannot be observed in the existing data (Stölken and Evans, 1998).

4 Microbending of thin copper foils

4.1 Introduction

Understanding the influence of material properties on size effect is certainly crucial for materials science and engineering applications. Therefore, the improved bending technique was performed on thin copper foils to study the influence of material properties on size effect. Both copper and nickel possess the same structure (face centred cubic (fcc)) but very different moduli (e.g. the elastic modulus of copper is about half that of nickel). Correspondingly, by comparing the bending results of nickel and copper, the effect of material properties on size effect will be revealed. In this chapter, the bending results for copper foils are presented and discussed.

4.2 Materials and methods

The bending measurements were performed on high purity copper foils over a range of thickness and grain size. Foils having three thicknesses (h = 10, 50 and 125μm) were obtained from Goodfellow (Cambridge Limited, UK), of purity 99.9% or higher. The foils were known to be electrodeposited with very small grain sizes.

Foils were annealed to obtain various grain sizes. The grain sizes are characterized by etching in alcoholic ferric chloride and optical microscopy (Leica DMLM equipped with a camera). The method has been explained in detail in chapter 3. The etching time for copper foils was about 30s to 120s, mostly depending on foil thickness. The thicker the foils the longer time it required. Typical optical grain size

images of copper foils are shown in Fig. 4.1, which are of foils with thickness $h = 10$ and 50μm but similar grain size $d \approx 60$μm. It can be seen that grains are clearly observed after proper etching. Grain size calculation method has been described in chapter 3. Twin boundaries were not counted.

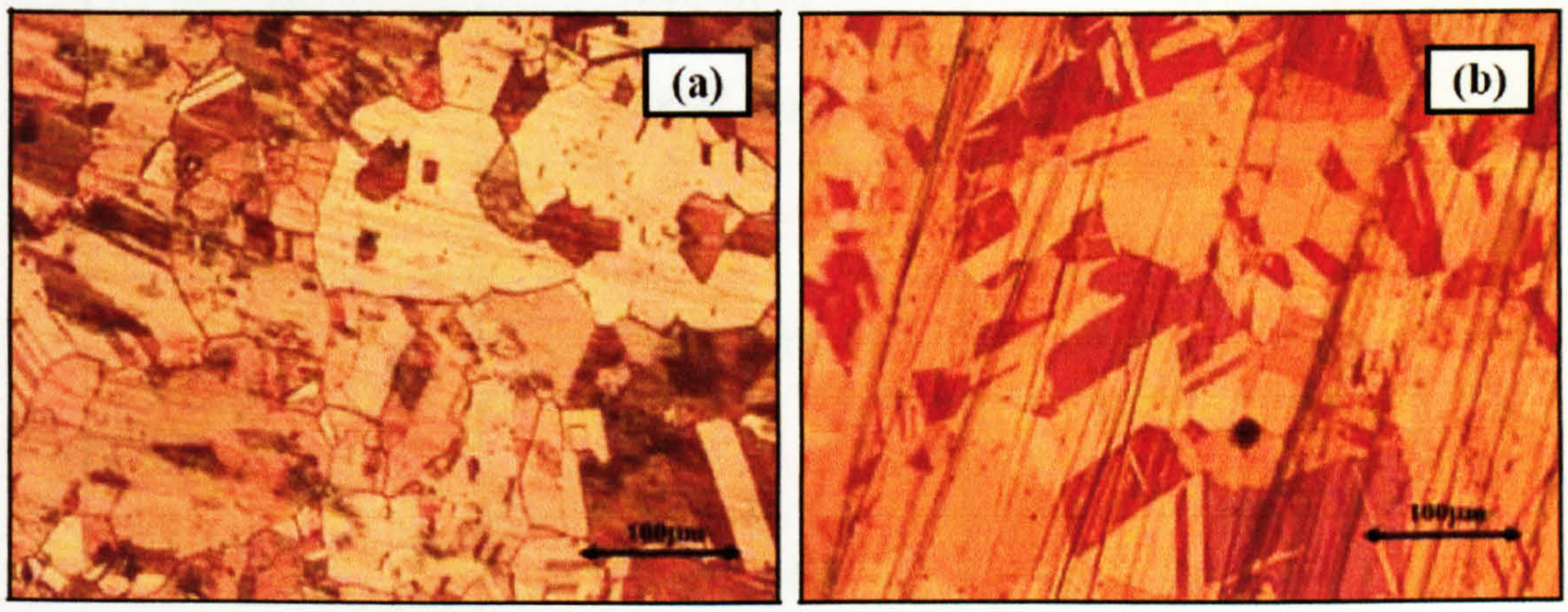

Figure 4.1 Optical microstructure pictures of Cu foils with different thickness but similar grain size $d \sim 60$μm. (a) 10μm foil with grain size $d = 60$μm, (b) 50μm foil with grain size $d = 58$μm.

The summary of annealing conditions and corresponding grain sizes of all foils used is tabulated in table 4.1.

Table 4.1 Annealing conditions and the corresponding grain sizes of copper foils. Bold red values were the chosen annealing conditions to obtain consistent grain sizes for h = 10, 50 and 125μm.

Thickness, *h* **/ μm**	**Annealing Conditions (Temp & time)**	**Grain size, *d*** **/ μm**
10	700°C, 5s	17
	700°C, 30s	27
	1000°C, 300s	**57**
50	700°C, 30s	23
	1000°C, 10s	**57**
	1000°C, 120s	80
125	700°C, 5s	26
	1000°C, 5s	**65**
	1000°C, 120s	155

Annealing the foils (table 4.1) shows that the grain growth rate of the copper foils is much higher than that of nickel foils (table 3.1). For instance, for 10μm thickness foil, the largest grain size is approximately six times of the thickness (table 4.1). This suggests that copper bending is highly suitable for use in the study of the interaction between grain and thickness size effect, since it is easier to obtain a wide ratio of d/h in copper foils.

The developed bending techniques (described in chapter 3) were applied here on copper thin foils including four-point bending (small strain region, ~0.2%) and

lap-top bending (relatively high strain region, ~10%). The calculation method of normalised bending moment M_n and surface strain ε_s was described in chapter 3. For copper, the relevant elastic modulus for a wide beam in bending (plane strain Young's modulus) was $E = 125$GPa.

4.3 Bending results and discussion

4.3.1 Grain and thickness size effects in copper bending

The results of the bending measurements are presented as plots of the normalised bending moment (stress) M_n against the surface strain ε_s in Figs.4.2 & 4.3. These are presented in a manner that highlights the separate dependencies on foil thickness and grain size. Those summarized on Fig.4.2 are for foils having the same grain size but different thickness. Whereas, the corresponding results on Figs.4.3 are for foils with the same thickness but different grain size.

Firstly, the thickness size effect was studied by comparing foils having fixed grain size ($d \approx 60\mu$m) but different thickness (h =10, 50 and 125μm) in Fig. 4.2 (a) and (b). In Fig. 4.2 (a), the increase of whole stress-strain curves with decreasing thickness is clearly observed. For example, at 0.05 surface strain, the normalised bending moment of the 10μm foil is over 80MPa, whereas the 125μm one has normalised bending moment only 10MPa. Thinner foils are stronger than thicker ones. Fig.4.2(b) highlights the small strain area, which is obtained from 4-point bending (Fig.3.9). The departure of data from the theoretical elastic line is observed. If the yield is defined as a significant departure from the elastic line, in Fig.4.2(b), the yield

stress increases in thinner foils. The M_n is about 7MPa for 10μm foil and below 2MPa for 125μm foil.

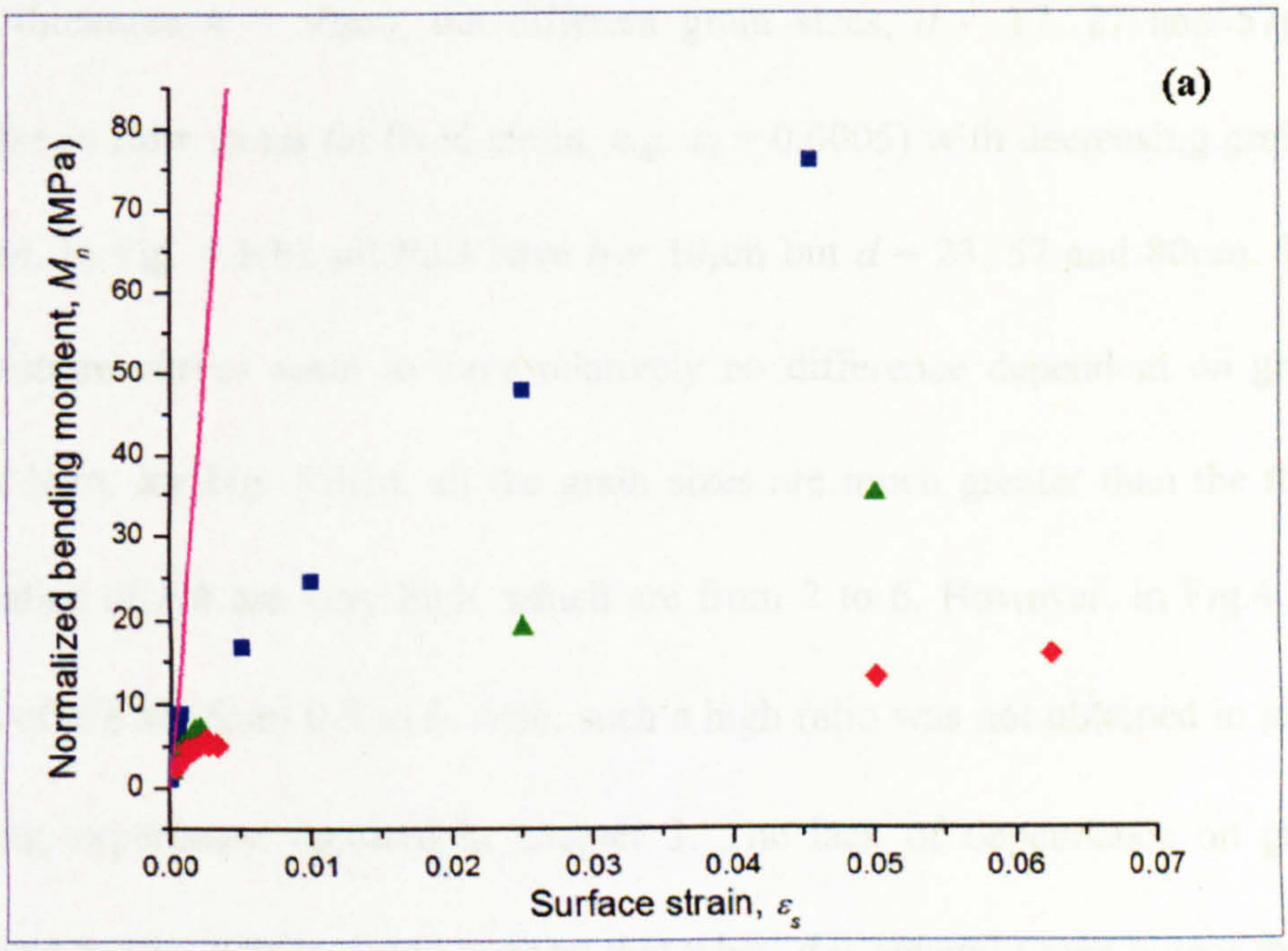

Figure 4.2 M_n Vs. ε_s, for foils: h = 10μm (blue cubic), h = 50μm (green triangle) and h = 125μm (red diamond). $d \approx 60$μm in all three foils. Solid line is the theoretical elastic line. (a) Full range of strain is shown. Work hardening rate increases in thinner foils. (b) The data at small strain is shown in detail. The clear departure from elastic line is observed and increases in thinner foils.

Then, the grain size effect was studied by comparing foils with the same thickness but different grain sizes as in Figs. 4.3. In Fig. 4.3(a), all foils are having same thickness h = 50μm, but different grain sizes, d = 17, 27 and 57μm. The increase in flow stress (at fixed strain, e.g. ε_s = 0.0005) with decreasing grain size is evident. In Fig. 4.3(b), all foils have h = 10μm but d = 23, 57 and 80μm. The flow stress-strain curves seem to have relatively no difference dependent on grain size. Noted here, for Fig. 4.3(b), all the grain sizes are much greater than the thickness. The ratios of d/h are very high, which are from 2 to 6. However, in Fig.4.2(b), the ratios of d/h are from 0.5 to 6. Also, such a high ratio was not obtained in nickel foil bending experiment reported in chapter 3. The lack of dependence on grain size observed in Fig. 4.3(b), could suggest that when d is several times bigger than h, the grain size effect vanishes. It is certainly reasonable. Assuming $d >> h$, the situation is the same as bending a single crystal thin film, where there is no grain size effect and only a thickness effect. However, the exact ratio at which grain size effect disappears has not yet been determined in this study. Foils having a wider ratio of d/h are certainly useful for the study of the exact interaction between d and h. This would be an interesting future work.

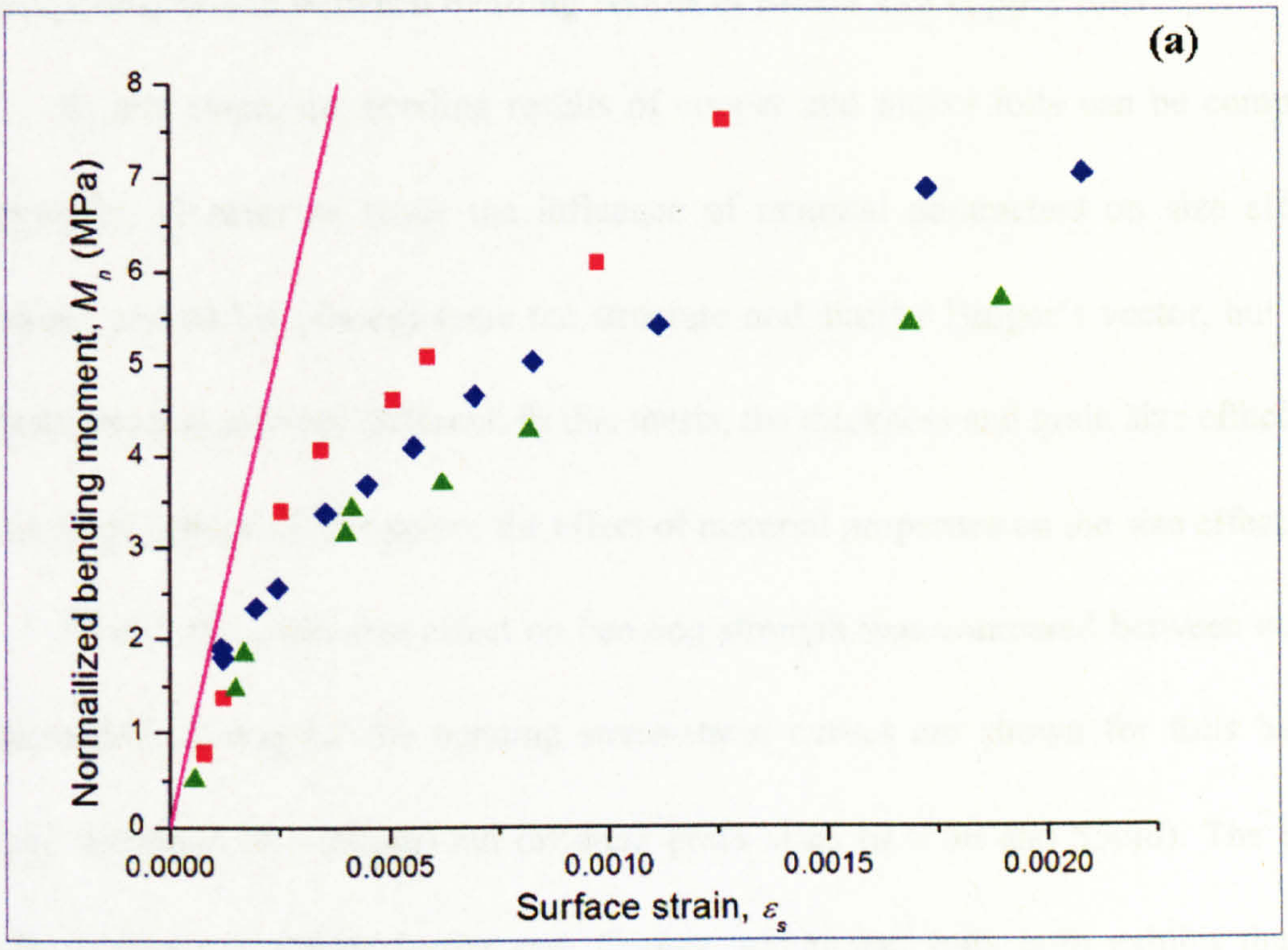

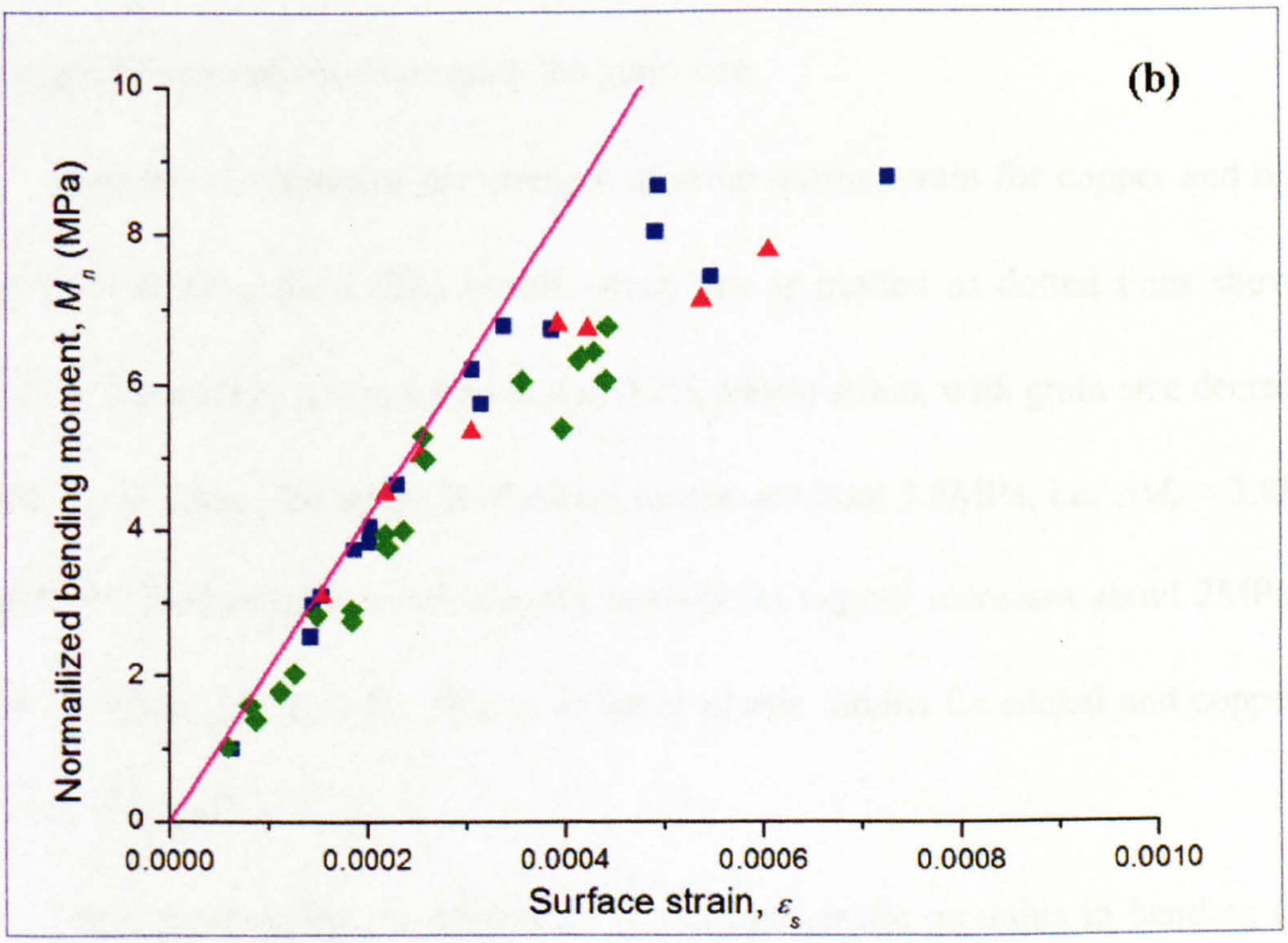

Figure 4.3 M_n Vs. surface strain ε_s. Solid pink line is the theoretical elastic line. (a) For h = 50μm foils with different grain sizes: d = 23μm (red cubic), d = 57μm (blue diamond) and d = 80μm (green triangle) (b) For h = 10μm foils with different grain sizes: d =17μm (red triangle), d =27μm (green diamond) and d =57μm (blue cubic).

4.3.2 Comparison between bending results of nickel and copper foils

At this stage, the bending results of copper and nickel foils can be compared primarily, in order to study the influence of material parameters on size effects. Copper and nickel possess same fcc structure and similar Burger's vector, but their elastic moduli are very different. In this thesis, the thickness and grain size effects are compared separately to explore the effect of material properties on the size effect.

Firstly, the grain size effect on bending strength was compared between copper and nickel. In Fig.4.4 the bending stress-strain curves are shown for foils having same thickness (h = 50μm) but different grain sizes ($d \approx$ 30 and 55μm). The black solid curves are guides to the eye. Copper and nickel foils both exhibit that the strength is increased as decreasing the grain size.

In order to determine the strength at same plastic strain for copper and nickel, e.g. ε_{pl} = 0.02%, the 0.02% plastic strain line is plotted as dotted lines shown in Fig.4.4. For nickel, it was found that at 0.2% plastic strain, with grain size decreasing from 55 to 30μm, the strength of nickel increases about 3.8MPa, i.e. $\Delta M_n \approx$ 3.8MPa. However, for the same condition, the strength of copper increases about 2MPa, i.e. $\Delta M_n \approx$ 2MPa (in Fig.4.4). ΔM_n at different plastic strains for nickel and copper are shown in Fig.4.5.

Then, considering the difference of relevant elastic modulus in bending (plain strain Young's modulus) between nickel (E = 220GPa) and copper (E =125GPa), the enhancement of strength is normalised by the elastic modulus respectively. The corresponding normalised enhanced strengths $\Delta M_n / E$ against different plastic strains

of nickel and copper are shown in Fig. 4.5. The solid curves are guides for the eye. From Fig. 4.5, it is seen that the normalised strength $\Delta M_n / E$ of copper and nickel are nearly the same over a range of plastic strain. This expresses the size effect in terms of strain rather than stress. In this form the grain size effect seen in bending does not depend on elastic modulus. This suggests it is a geometrical effect.

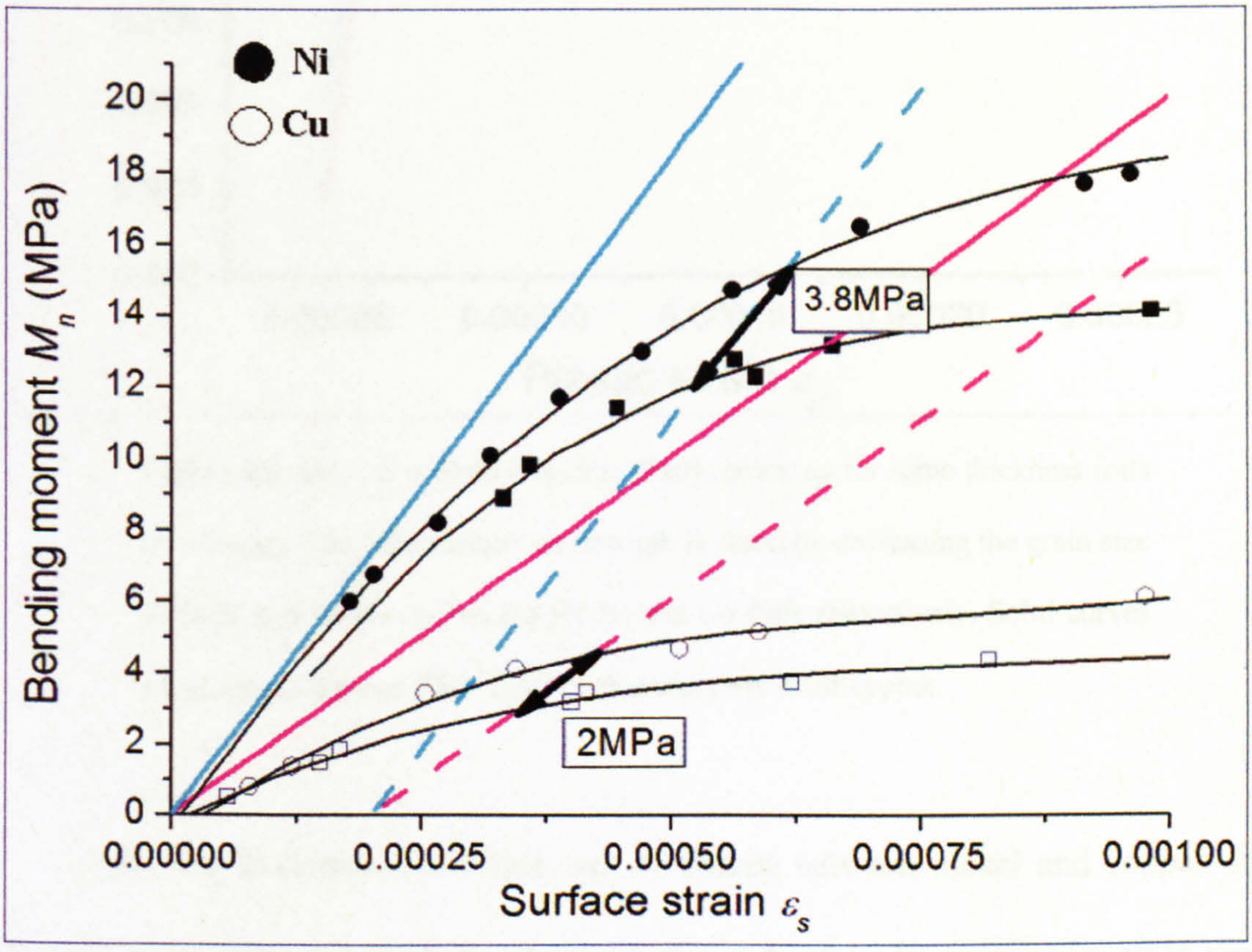

Figure 4.4 M_n Vs. ε_s for foils all having same thickness h = 50μm. Solid and hollow points are for Ni and Cu respectively: d ~ 30μm (circle), d = 55μm (square). Blue line is the theoretical elastic line for Ni. Pink line is the theoretical elastic line for Cu. The black solid curves are guides to the eye.

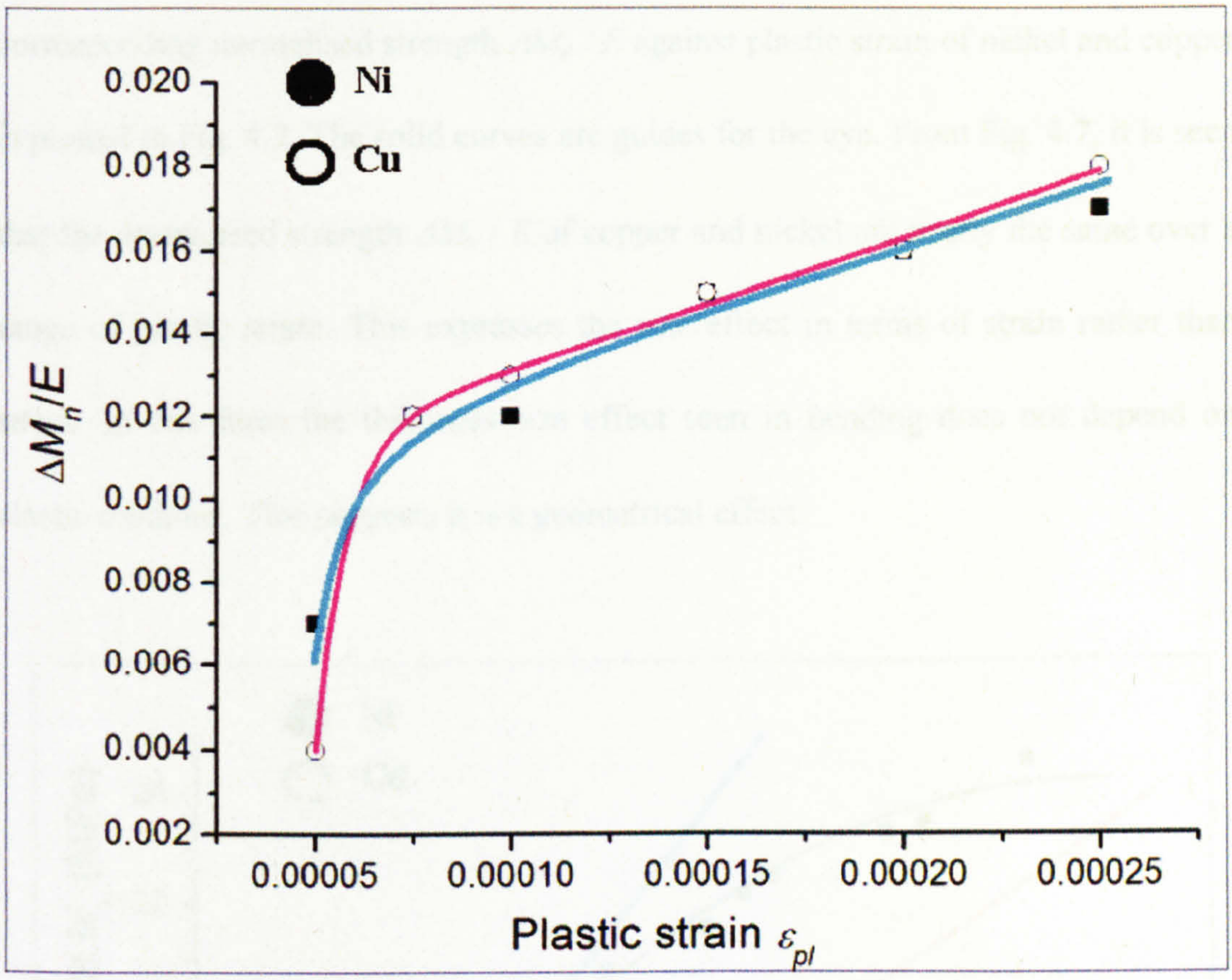

Figure 4.5 $\Delta M_n / E$ is plotted against plastic strain ε_{pl} for same thickness foils ($h = 50\mu m$). The enhancement of strength is cased by decreasing the grain size d. Solid and hollow points are for Ni and Cu foils respectively. Solid curves are guides to the eye. Blue is for Nickel and pink is for copper.

Then, the thickness size effect was compared between nickel and copper. In Fig.4.6, the bending stress-strain curves are shown for foils having similar grain size ($d \approx 30\mu m$) but different thickness (h = 10 and 125μm). The black solid curves are guides for the eye. Copper and nickel foils both show that the strength is increased with decreasing foil thickness.

Now, considering the difference of relevant elastic modulus of bending (i.e., plain strain Young's modulus) between nickel (E = 220GPa) and copper (E =125GPa), the enhancement of strength is normalised by the modulus. The

corresponding normalised strength $\Delta M_n / E$ against plastic strain of nickel and copper is plotted in Fig. 4.7. The solid curves are guides for the eye. From Fig. 4.7, it is seen that the normalised strength $\Delta M_n / E$ of copper and nickel are nearly the same over a range of plastic strain. This expresses the size effect in terms of strain rather than stress. In this form the thickness size effect seen in bending does not depend on elastic modulus. This suggests it is a geometrical effect.

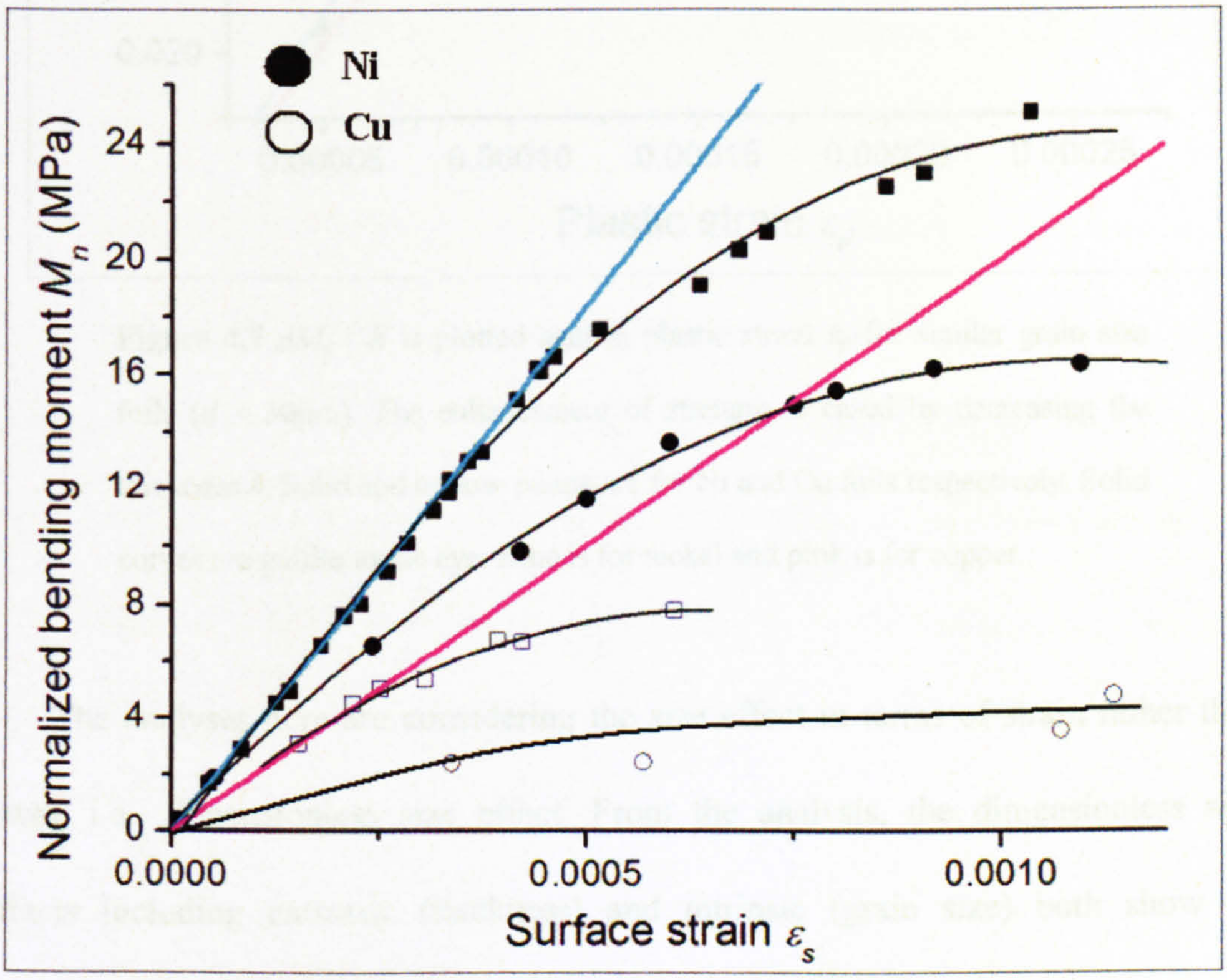

Figure 4.6 M_n Vs. ε_s for foils all having similar grain size d~30μm. Solid and hollow points are for Ni and Cu respectively: h = 10μm (square) and h = 125μm (circle). Blue line is the theoretical elastic line for Ni. Pink line is the theoretical elastic line for Cu. The black solid curves are guides to the eye.

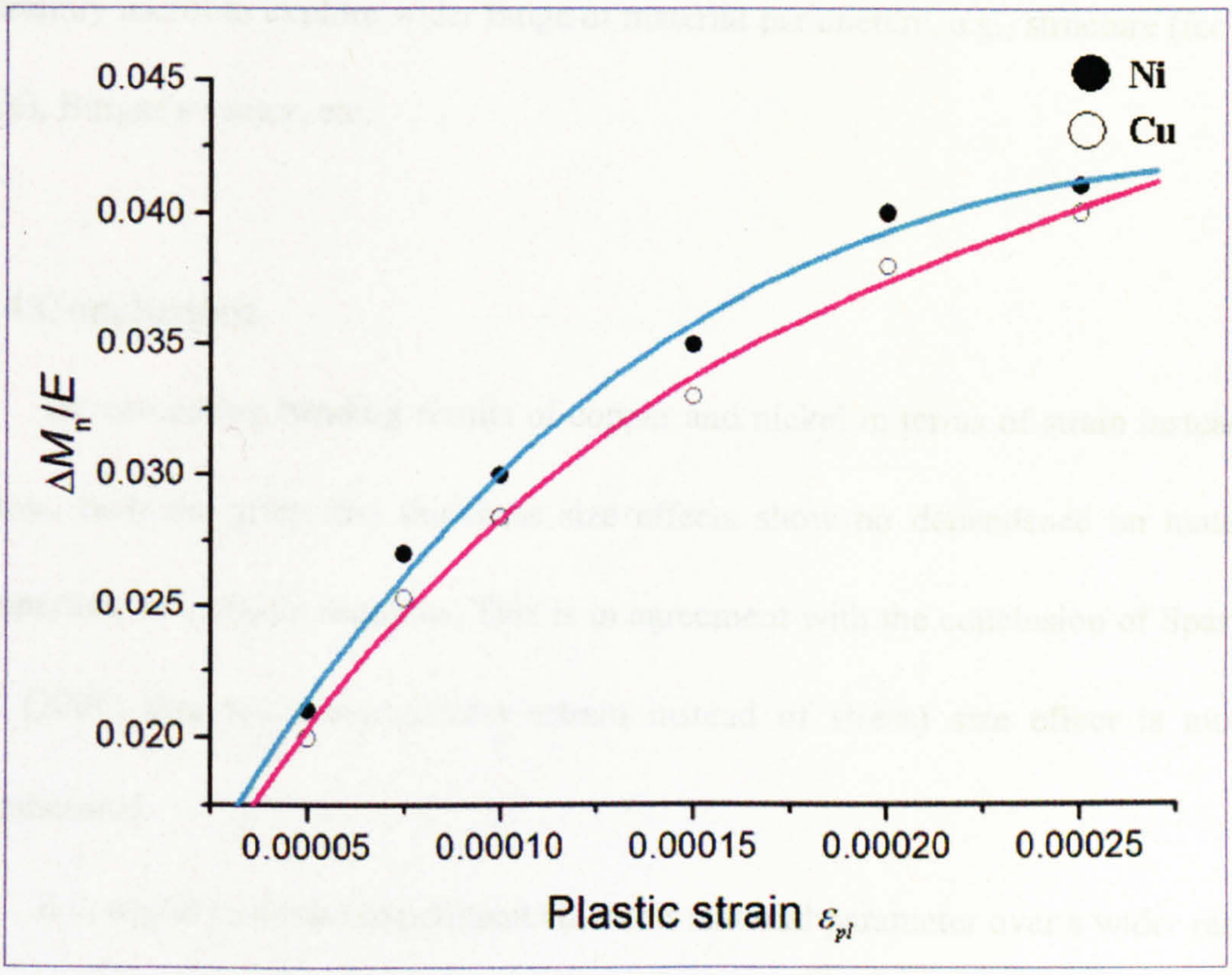

Figure 4.7 $\Delta M_n / E$ is plotted against plastic strain ε_{pl} for similar grain size foils ($d \approx 30\mu m$). The enhancement of strength is cased by decreasing the thickness h. Solid and hollow points are for Ni and Cu foils respectively. Solid curves are guides to the eye. Blue is for nickel and pink is for copper.

The analyses here are considering the size effect in terms of strain rather than stress, i.e., dimensionless size effect. From the analysis, the dimensionless size effects including extrinsic (thickness) and intrinsic (grain size) both show no dependence on the material properties. They are geometrical effects. This result is in good agreement with Spary *et al.* (2006), who studied indentation size effect in metals. However, both our bending and their indentation (Spary *et al.*, 2006) experiments are on soft fcc metals. Hence, these cases may only be able to indicate that the size effects are independent on the elastic modulus of materials. So it is

certainly useful to explore wider range of material parameters, e.g., structure (fcc and bcc), Burger's vector, etc.

4.4 Conclusions

By comparing bending results of copper and nickel in terms of strain instead of stress, both the grain and thickness size effects show no dependence on material properties, i.e., elastic modulus. This is in agreement with the conclusion of Spary *et al.* (2006) that the dimensionless (strain instead of stress) size effect is mostly geometrical.

It is useful to devise experiments that test material parameter over a wider range, e.g., ceramics and metals. However, bending a ceramic foil is difficult. For this reason, indentation is performed to study the size effect in ceramics and metals, where they have very different Burger's vector (about two times difference) and yield strain (about ten times difference). The details will be presented and discussed in chapter 7.

5 Bending stress-strain curves analysis

(This part is published in Phil. Mag.)

5.1 Introduction

The new nickel bending stress-strain curves described in chapters 3, were motivated by the observation that the data of Fleck *et al.* (1994) and of Stölken and Evans (1998) was fitted equally well by critical thickness theory as by strain-gradient plasticity theory (Dunstan and Bushby, 2004). However, there was no data around the key region of the elastic-plastic transition, or yield point; that is important for distinguishing the two different theoretical approaches.

Another motivation was to study the interaction between grain size (intrinsic) and dimensional (e.g. thickness) size effect, which is crucial for the engineering applications, but reported rarely in the literature both in experiments and theories (as reviewed in section 2.4). The Hall-Petch (grain size) effect has not been systematically studied in small structures (i.e. structures with a characteristic length (thickness) $h \sim$ (grain size) d). Venkateswaran and Bravman (1992) studied Al films on silicon substrates and obtained the flow stress and its dependence on film thickness. However, they had only two grain sizes and were not able to distinguish between the Hall-Petch $d^{-1/2}$ dependence and the d^{-1} dependence that they considered more plausible. They assumed that the effects of h and d are separable. Thompson explained their results using critical thickness theory (and introducing a critical grain size as well as a critical thickness) but the theory necessarily yields a d^{-1} dependence

rather than the Hall-Petch $d^{-1/2}$ (Thompson, 1992). Other than this, critical thickness effects have not been studied as a function of grain size. Strain-gradient plasticity has not been studied as a function of grain size, nor through the yield point. Mechanistic explanations or theoretical explanations for these effects do not consider interaction between them.

New nickel foil bending data have been presented in chapter 3. In this chapter, these data are analysed in detail. The yield and work hardening size effects are studied. Careful consideration of interaction between grain and thickness size effects is taken. In conclusion, even with the improved data obtained here, it is clear that better data around the elastic-plastic (yield) point is still required. However, in the plastic region, the data shows that the strain-gradient or critical thickness effects and the Hall-Petch effect on the work-hardening and the flow stress are intimately linked. This implies a reconsideration of the mechanisms both of the Hall-Petch effect and of strain-gradient plasticity. The result also implies that the grain boundary and free surface may have the same effect on material strength.

5.2 Bending stress-strain curve analysis and results

Nickel foil bending data reported in chapter 3, are fitted using classical plasticity theory (solid lines in Fig. 5.1), with linear work-hardening, using

$$\begin{cases} \sigma(\varepsilon) = E\varepsilon & \sigma \le \sigma_0 \\ \sigma(\varepsilon) = \sigma_0 + k\varepsilon_p & \sigma \ge \sigma_0 \end{cases} \tag{5.1}$$

where E is the relevant elastic modulus (plain strain Young's modulus) in bending, σ_0 is the yield stress, k is the rate of linear work hardening, and $\varepsilon_p = \varepsilon - \sigma_0/E$ is used

as a close approximation to the true plastic strain, $\varepsilon - \sigma(\varepsilon) / E$. In classical plasticity theory, plastic yield occurs when the stress reaches the yield stress. The beam is deformed elastically from the centre, $z = 0$, to $z = \pm z_0$ where z_0 is defined by $Ez_0 / R_1 = \sigma_0$. From $\pm z_0$ to the free surfaces at $z = \pm \frac{1}{2}h$ the deformation is plastic. This gives the following expression for the bending stress when plasticity occurs,

$$\begin{aligned} M_n &= \frac{1}{h^2}\int_{-1/2h}^{1/2h} z\sigma(\varepsilon)dz = \frac{2}{h^2}\int_0^{z_0}\frac{z^2E}{R_1}dz + \frac{2}{h^2}\int_{z_0}^{1/2h} z\left(\sigma_0 + k\frac{(z-z_0)}{R_1}\right)dz \\ &= \left(\frac{\sigma_0}{4} - \frac{\sigma_0^3}{12E^2\varepsilon_s^2}\right)\left(1-\frac{k}{E}\right) + \frac{k\varepsilon_s}{6} \end{aligned} \tag{5.2}$$

and this is the function fitted to our data in Fig. 5.1. Linear work hardening is adequate to describe the data as can be seen from Fig. 5.1 at large strains. This fitting (Fig. 5.1) is done by post doc in our group Dr. Chris Walker. Close inspection around the yield point (Fig.5.1 inset) shows that the onset of yield is more complicated than the model assumes. There can be some plastic yield at as little as half the bending stress corresponding to σ_0. In what follows, therefore, σ_0 is referred to as the 'fitted yield stress' – this can be considered to represent the onset of gross or macroscopic plasticity.

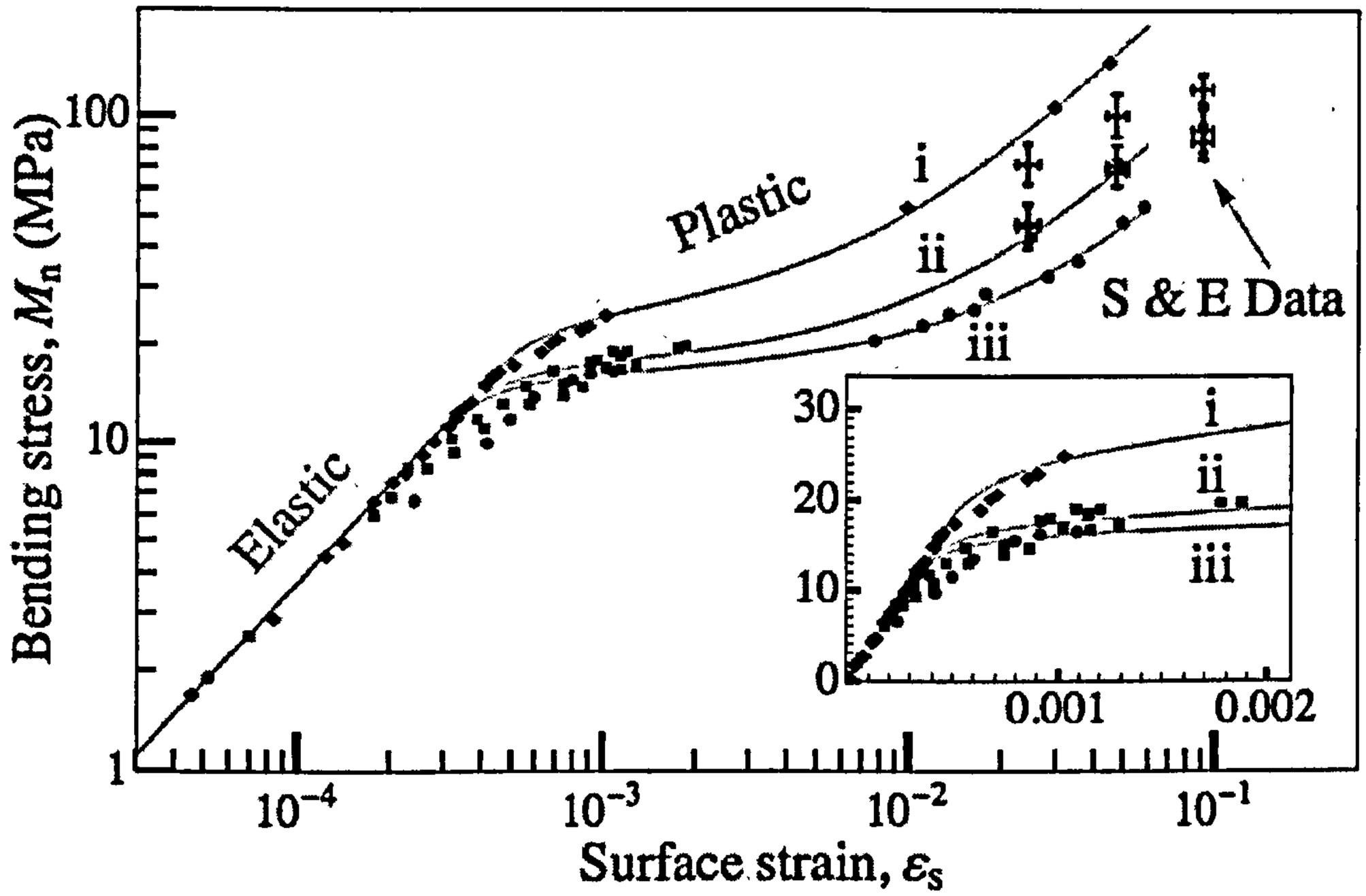

Figure 5.1 The data are plotted as normalised bending stress M_n against surface strain ε_s over the full range of our experiments, for the foil thicknesses (i) 10 μm, (ii) 50 μm and (iii) 125 μm. Grain sizes are approximately 30μm in all three foils. The data of Stölken and Evans (1998) is shown with their error bars (┼). In the inset (linear scale) the region at low strain is shown in more detail. The solid curves are fits using classical plasticity theory, Eq. (5.2), with the two fitting parameters σ_0 and k.

It is clear from Figs. 5.2 and 5.3 that both σ_0 and k depend upon both d and h, increasing as the grain size and foil thickness are decreased. Traditionally these are separate effects (Venkatraman and Bravman, 1992). The data in Fig. 5.2 for σ_0 are consistent with this. The fitted yield stress data agree with

$$\sigma_0(d,h) = \frac{330}{\sqrt{d}} + \frac{430}{h} = \frac{\sigma'_{HP}}{\sqrt{d}} + \frac{\sigma'_{CTT}}{h} \tag{5.3}$$

with σ_0 in MPa and d and h in microns (solid lines in Fig 5.2), that is, additive effects for h and d, and – perhaps surprisingly – with no breakpoint between $d<h$ and $d>h$. The first term may be interpreted as the Hall-Petch effect (the inverse square root of grain size) (Hall, 1951; Petch, 1953) with the constant $\sigma'_{HP} = 0.33\text{MPa m}^{1/2}$, independent of foil thickness. Values of σ'_{HP} for bulk nickel from 0.16 to 0.45MPam$^{1/2}$ have been reported (Ebrahimi *et al.*, 1999; Hansen, 2004). Our value is in this range, in accordance with the classical Hall-Petch behaviour at the yield point. The second term is an additive term for the critical thickness effect which increases the yield stress in the thinner foils, independent of grain size. The critical thickness term has been previously observed by Moreau *et al.* (2005) and the full theory was given in Dunstan and Bushby (2004).

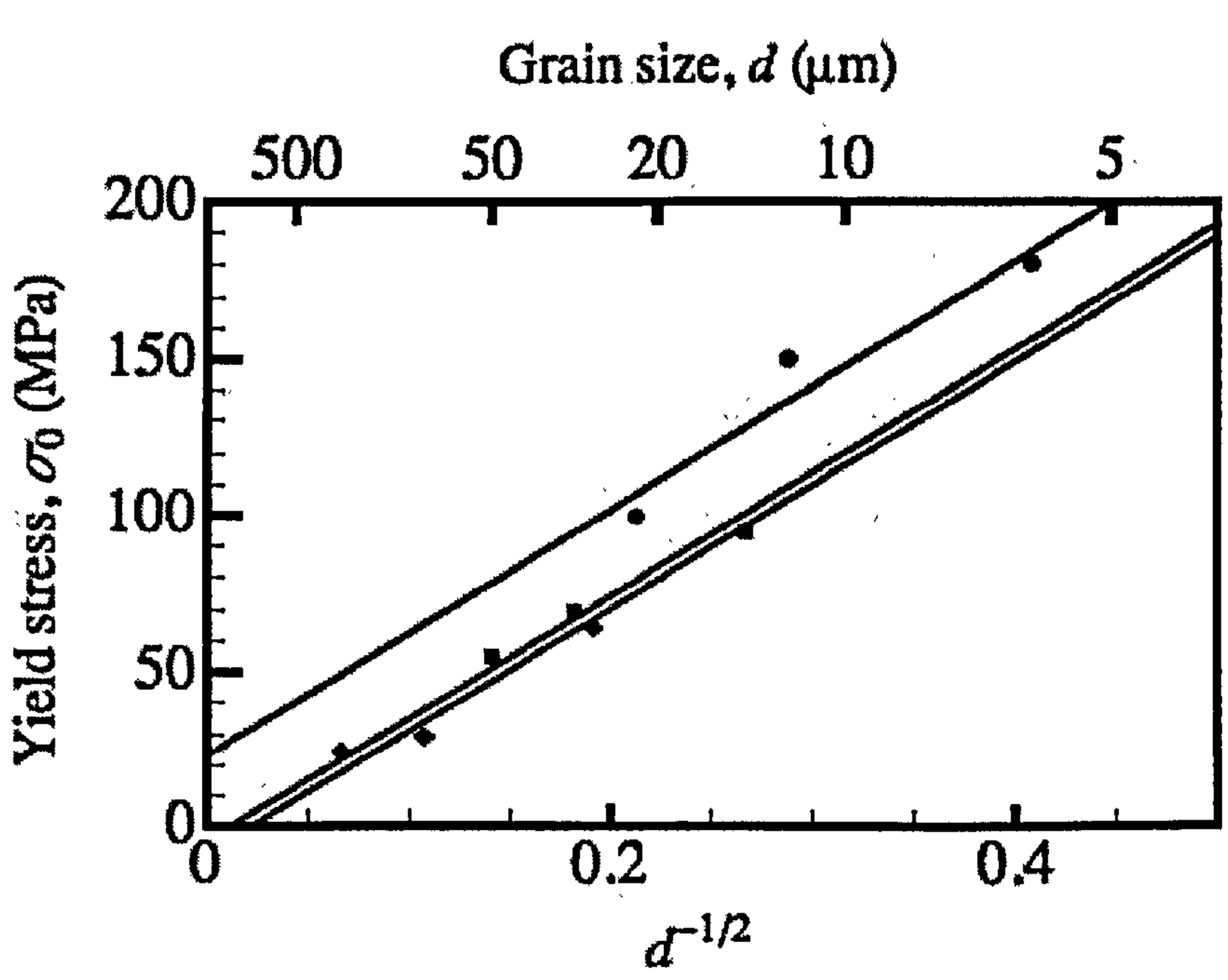

Figure 5.2 The fitted yield stress σ_0 is plotted against the inverse square root of the grain size for the three foil thicknesses 10μm (■), 50μm (●), and 125μm (▲). The solid curves are the fits of Eq. (5.3).

In contrast to the yield-point data, the work-hardening data in Fig. 5.3(a) for k, the effects of d and h are multiplicative. The work-hardening data fit well to

$$k(d,h) = \frac{120}{\sqrt{d}\sqrt{h}} \tag{5.4}$$

with k in GPa and d and h in microns. Normalising by multiplying by $\sqrt{h}$, the nine data points fall on a single straight line (Fig.5.3(b)). From the data of Stölken and Evans (1998), the k values are estimated of 1GPa for their 50μm foil with 71μm grain size, and 2.5GPa for their 12.5μm foil with 31μm grain size. Our equivalent k values, from Eq.(5.4), are 2GPa and 6GPa respectively, consistent within their error bars.

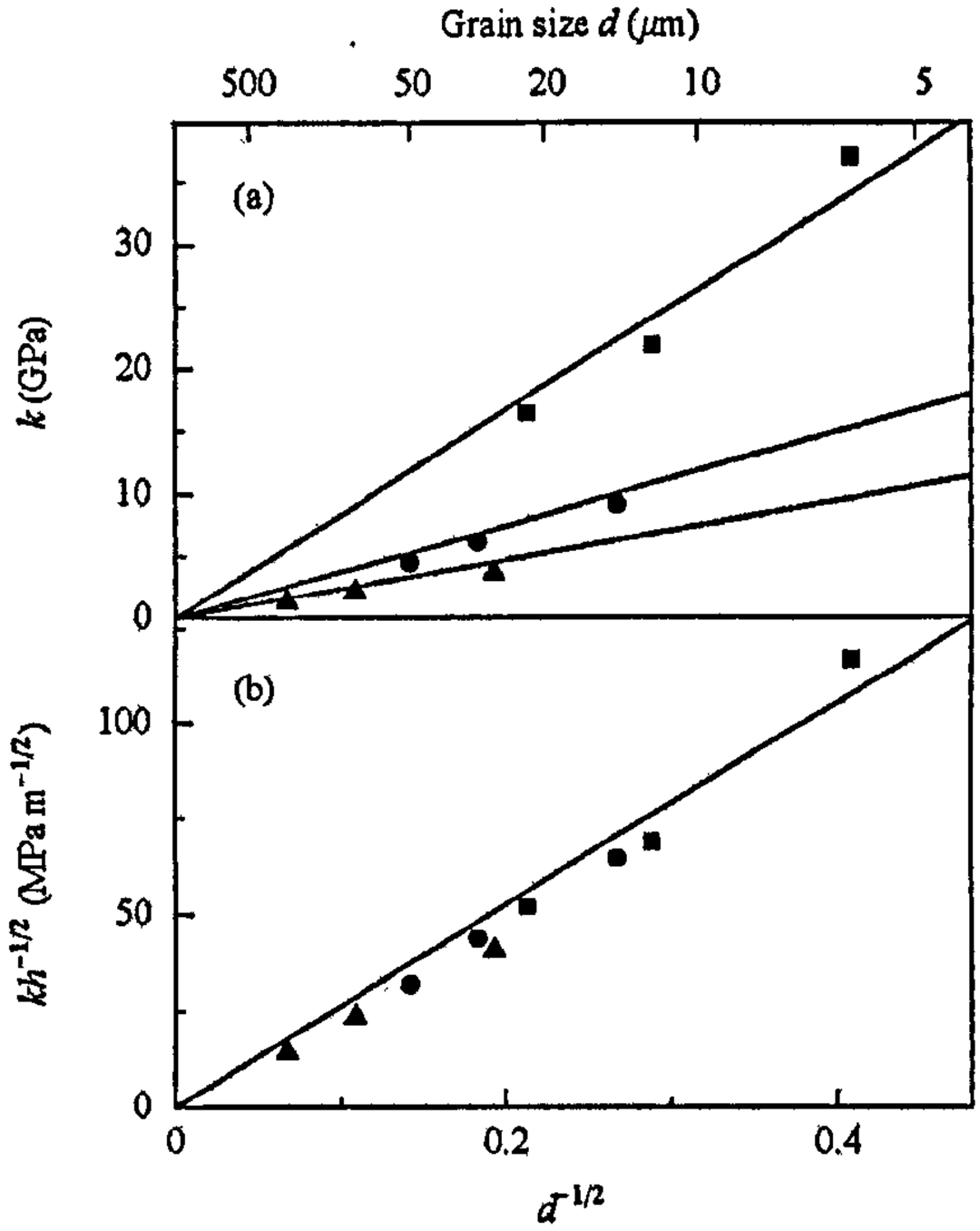

Figure 5.3 In (a), the work-hardening parameter k is plotted against the inverse square root of the grain size, for the three thicknesses 10μm (■), 50μm (●), and 125μm (▲). The solid curves are the fits of Eq. (5.4). In (b), the work-hardening parameter is normalised by multiplying by $\sqrt{h}$ and the solid line is a fit to the data for all three foil thicknesses.

However, other fits are possible. A square-root work-hardening law might be used at small plastic strains instead of the linear work-hardening of Eq. (5.1). This fitting (Fig. 5.4) of stress–strain curves was done by the undergraduate student with our group: Bruno Ehrler. This square-root work hardening would fit the data around the elbow in Fig.5.1 more accurately and it would yield different values for the fitted yield point σ_0 (values of σ_0 are much smaller than in the linear work-hardening fit but not zero, as illustrated in Fig. 5.4).

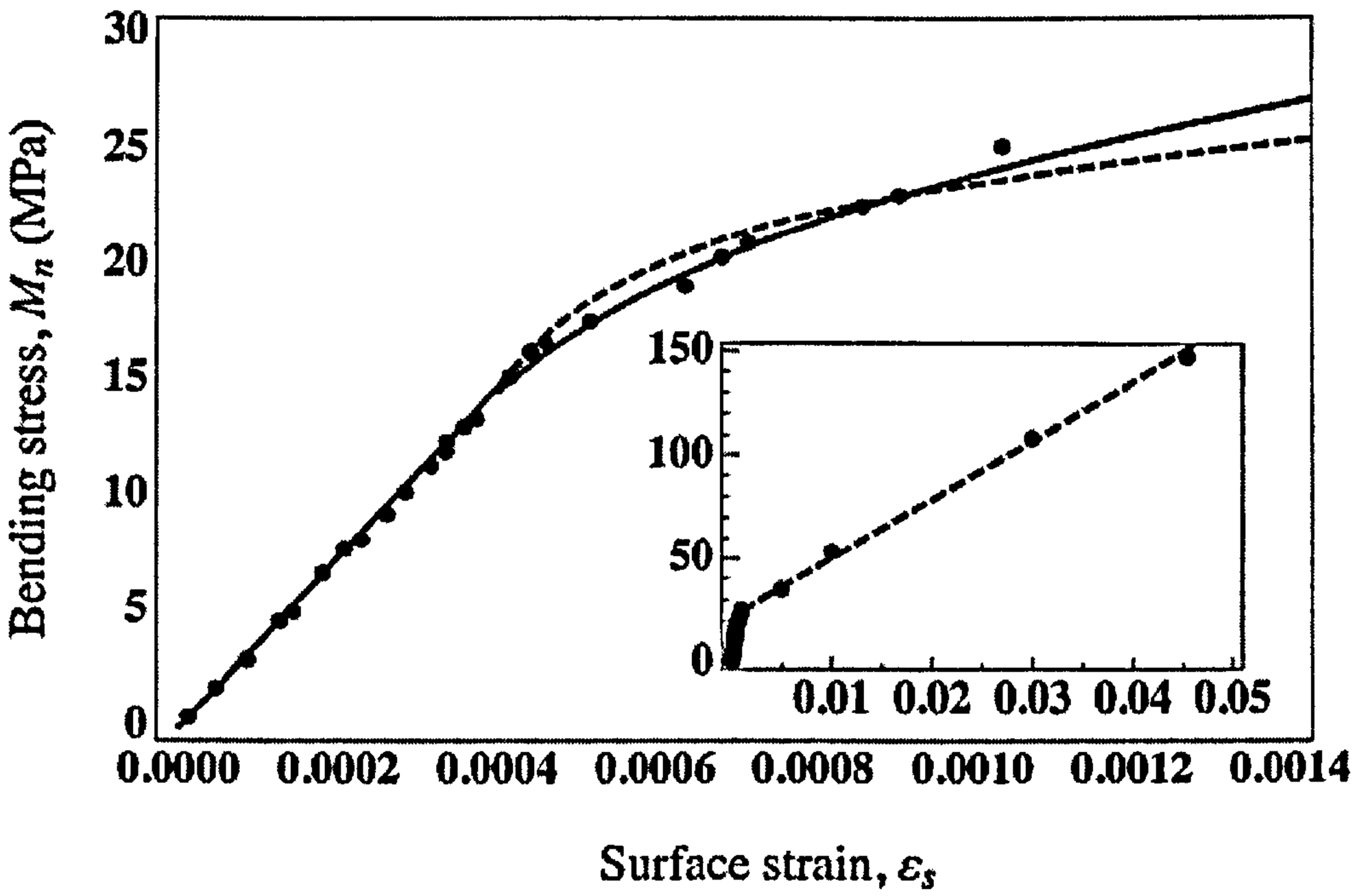

Figure 5.4 The normalised bending moment M_n against surface strain ε_s for a 10μm foil with grain size $d \approx 30$μm. The solid line is the fit by square root hardening. And the dotted line is the fit by Eq. (5.1). In the inset (linear scale) the region at high strain is shown with dotted line fitted by Eq. (5. 1).

Going further, one may be doubtful of the physical meaning of a yield stress in a soft metal. What is observed may be interpreted not as a yield stress but as the flow stress at the lowest resolved plastic strain. Then it may be more instructive to plot the

raw data differently rather than plot the fitted σ_0. Following Thompson (1992), the flow stress should depend upon grain size and structure size as $d^{-1} + h^{-1}$. Fig. 5.5 shows a log-log plot of bending moment at a wide range of strains against an effective length or size l_{eff} given by $\ell^{-1}_{eff} = d^{-1} + h^{-1}$. At all strains, the data are consistent with straight-line fits. However, at low strains, where square-root work hardening fits better, the gradients are very close to '-1/2', indicating a square-root dependence on the effective size ℓ_{eff}.

At high strains, where linear work hardening fits better, the gradients are very close to '–1' as in Thompson's theory. This is interesting, as Thompson's (1992) theory would be expected to be valid at small plastic strains rather than at high. The theory certainly does not predict the power $\ell^{-1/2}_{eff}$ observed here at small strains.

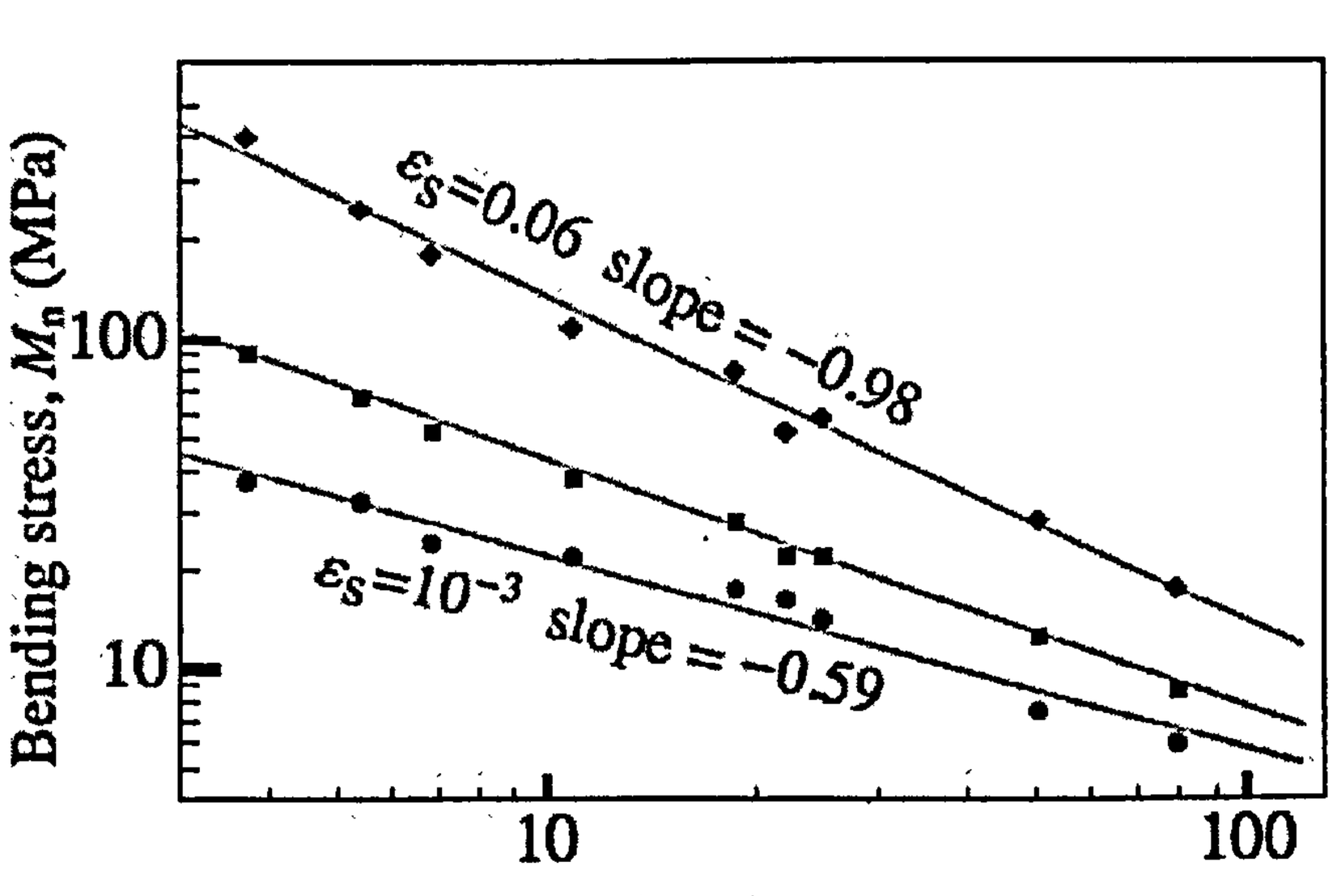

Figure 5.5 The data for the bending stress at three different values of strain and all nine combinations of grain size d and foil thickness h are plotted against the effective size defined by: $\ell^{-1}_{eff} = d^{-1} + h^{-1}$. On the log-log plot the data show little scatter and are consistent with slopes varying from '–1/2' at low strain to '–1' at high strain.

5.3 Discussion

In order to study the yield and work hardening size effect, linear and square-root work hardening analysis were applied to fit the nickel bending data respectively. The results show that the square-root work hardening fits better at small strain region (elbow of the stress-strain curve, i.e. elastic-plastic transition region), whereas linear work hardening fits better at relatively high strain region. The yield strength are different (but none of them zero) from these two different fits. Even with the data-set which covers wide range of strain that reported here on Ni foil-bending, better data around the elastic-plastic point is still desirable before the decision can be made as to whether a yield point is a valid and useful concept or not and whether critical thickness theory is relevant to it.

The clear symmetry shown between d and h in work hardening coefficient k (Fig.5.3) and flow strength in Fig. 5.5, and the absence of any breakpoint in the data or the fits between $d < h$ and $d > h$, may suggest that different ways of delimiting a finite volume or thickness have the same effect on the strength, whether the strained volume is delimited by grain boundaries or by the free surface.

5.4 Conclusions

The yield study has not yet been completed. Better data around the elastic-plastic point (elbow of the stress-strain curve) is still required.

The clear symmetry shown between d and h in work hardening coefficient k (Fig.5.3) and flow strength in Fig. 5.5, and the absence of any breakpoint in the data or the fits between $d < h$ and $d > h$, may suggest that the grain boundary and free surface have similar effect on material strength.

No existing theories predict the totality of the results reported here. Understanding the underlying mechanics is certainly a crucial future work, for instance, the meaning of effective length l_{eff}, which combine the intrinsic and extrinsic effect.

A possible explanation of effective length l_{eff} will be presented in chapter 8.

6 Nanoindentation calibrations

(This part has been published in Journal of Mechanics and Physics of Solids)

6.1 Introduction

Indentation testing is one of the most popular means for measuring the mechanical properties of materials at small length scales. It is essentially that a hard tip, whose mechanical and geometric properties are known, is pressed into a sample whose properties are unknown. The tip is usually made of diamond. As for nanoindentation, it is simply an indentation test in which the length scale of the penetration is measured in nanometres. It is popular, because the size of the specimen can be extremely small and the procedure is usually non-destructive. More general introductions can be found in Fisher-Cripps (2001).

There are various shapes of indenter tip. They can generally be divided into pointed and spherical indenters. Pointed indenters include: Vickers, Berkovich, Knoop and conical and so on, in which the shape is self-similar with depth. They are relatively easy to produce. A spherical indenter has the advantage that it can induce a large area of contact at a given depth, and provide the smooth transition from an elastic region to a plastic one. This is useful in studying the fully elasto-plastic relationship of the material.

Careful calibration of the indenter tip shape is a prerequisite to any nanoindentation test, because the mechanical properties are highly related to the tip geometry (Johnson, 1987; Fisher-Cripps, 2001). There are primarily two methods

for calibrating tips: AFM direct imaging and reference-material methods (Bushby and Jennett, 2001). According to Bushby and Jennett (2001), these two calibration methods are in good agreement. In this work, for convenience and consistency, all indenters (Berkovich and spherical indenters) were calibrated by indenting into reference materials (Bushby and Jennett, 2001). Multiple reference materials were applied, since there were too many unknowns for using a single material.

For this work, the main aim for applying spherical indentation, is to study the initial yield size effect, i.e., the elastic-plastic transition. Hence, different size indenters were required. Also, it is necessary to have the low uncertainty in indenter effective radius, at the depth when yield happens. Berkovich indentation was also applied to enable to the comparison to be made with the spherical indentation size effect (in chapter 7).

This chapter will describe and discuss the experimental details and results of indentation calibration (both Berkovich and spherical indentation). Before going into the experimental details of calibration, basic concepts of spherical and Berkovich nanoindentation are introduced. These are referred to a lot in the following calibration and chapter 7 (study on indentation size effect).

Spherical indenters were applied for most of this work. Therefore, spherical indentation concepts will be the focus of this chapter.

6.2 Spherical indentation calibration

All the spherical indenters used in this work are made of diamond, due to its high hardness and elastic modulus. However, the diamond indenter often deviates from an ideal spherical shape due to the difficulty of polishing an anisotropic crystal into a spherical shape. Hence, careful calibration of the tips is necessary before using them.

All spherical indenters were calibrated by indenting into several reference materials using the multiple partial-unload method.

6.2.1 Multiple partial unload indentation

The multiple partial unloading indentation technique was developed by Field and Swain (1993, 1995). It permits the elastic and plastic components of indentation to be separated and hardness and elastic modulus to be calculated at each step as a function of penetration and/or contact.

The material response is detected throughout the loading cycle by continuously recording the force F and penetration depth h_p. The indentation loading proceeds incrementally. Following each load increment to a force F_i, the load is reduced (partial unloading) by a small amount (in our experiments, to $0.75F_i$) before proceeding to the next higher load increment, F_{i+1}. Force and penetration are recorded at each load and partial unload step. Details are in Bushby, (2001).

Using the partial unloading technique, the shape of the unloading curve can be calculated for each pair of load (point 1) and unload (point 2) data (F_1, h_1; F_2, h_2)

using Hertzian mechanics (Fig.6.1). This approach assumes that the unloading is wholly linear elastic.

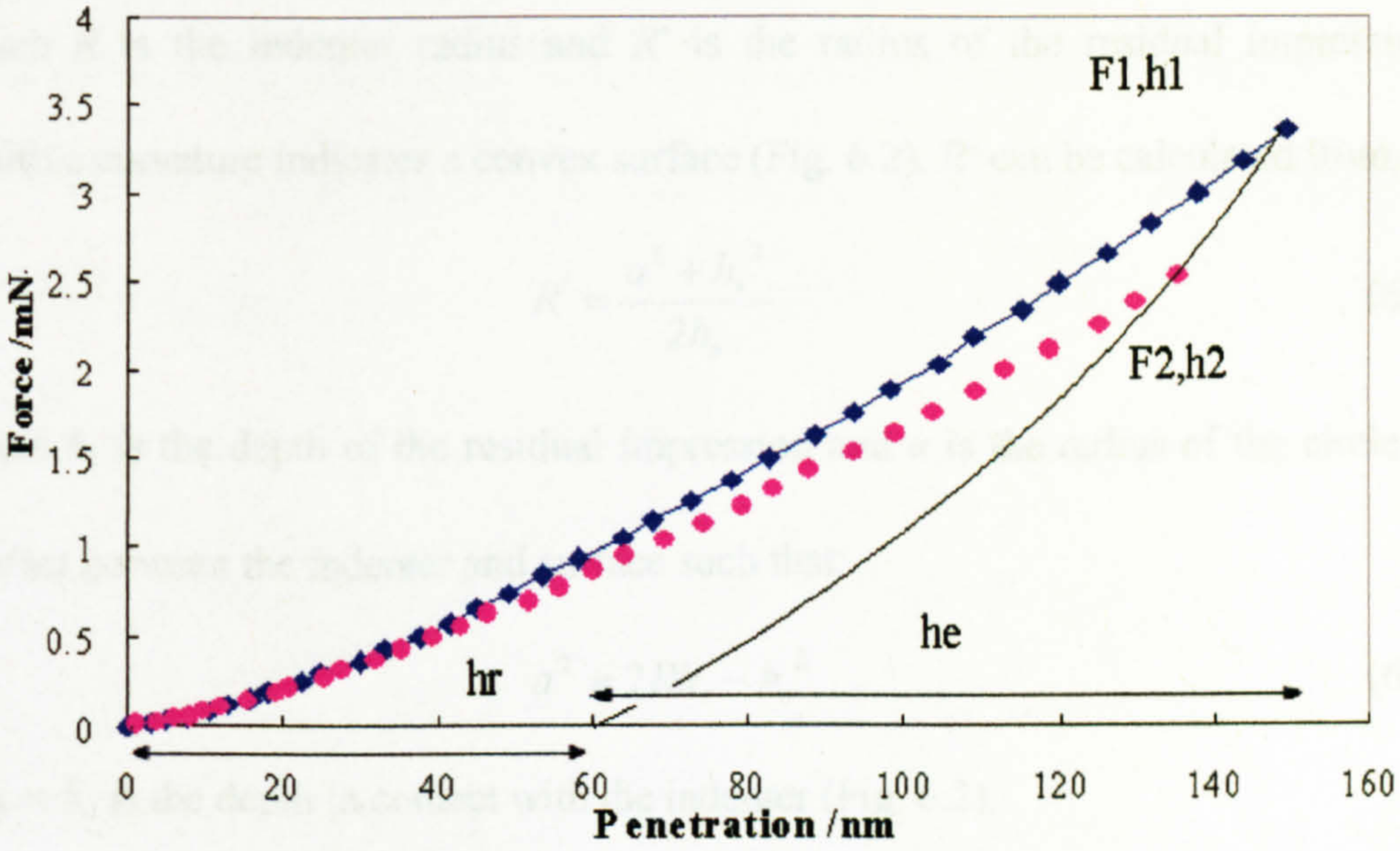

Figure 6.1 A typical example of a force – penetration data set. The fully loaded points diamond, partial unloaded points circles. The solid line is the load-unload curve that passes through points F_1, h_1 and F_2, h_2. This load-unload results in a residual depth h_r.

The elastic displacements, h_e, of the unloading curve are given by (Johnson, 1985):

$$h_e = \left(\frac{9}{16}\right)^{1/3}\left(\frac{F}{E^*}\right)^{2/3}\left(\frac{1}{R}-\frac{1}{R'}\right)^{1/3} \tag{6.1}$$

where F is the applied force on the indenter, E^* is the composite (indentation) modulus of the two surfaces in contact given by

$$\frac{1}{E^*} = \left(\frac{1-\nu_s^2}{E_s}\right)+\left(\frac{1-\nu_i^2}{E_i}\right) \tag{6.2}$$

in which E is the Young's modulus and ν is the Poisson's ratio for an isotropic material (other combinations of the elastic constants are required for single crystal

materials) and subscripts s and i refer to the indented surface and indenter respectively, and $\left(\frac{1}{R}-\frac{1}{R'}\right)$ is the relative curvature between in the two surfaces in which R is the indenter radius and R' is the radius of the residual impression, positive curvature indicates a convex surface (Fig. 6.2). R' can be calculated from:

$$R' = \frac{a^2 + h_r^{\,2}}{2h_r} \tag{6.3}$$

where h_r is the depth of the residual impression and a is the radius of the circle of contact between the indenter and surface such that:

$$a^2 = 2Rh_c - h_c^{\,2} \tag{6.4}$$

where h_c is the depth in contact with the indenter (Fig. 6.2).

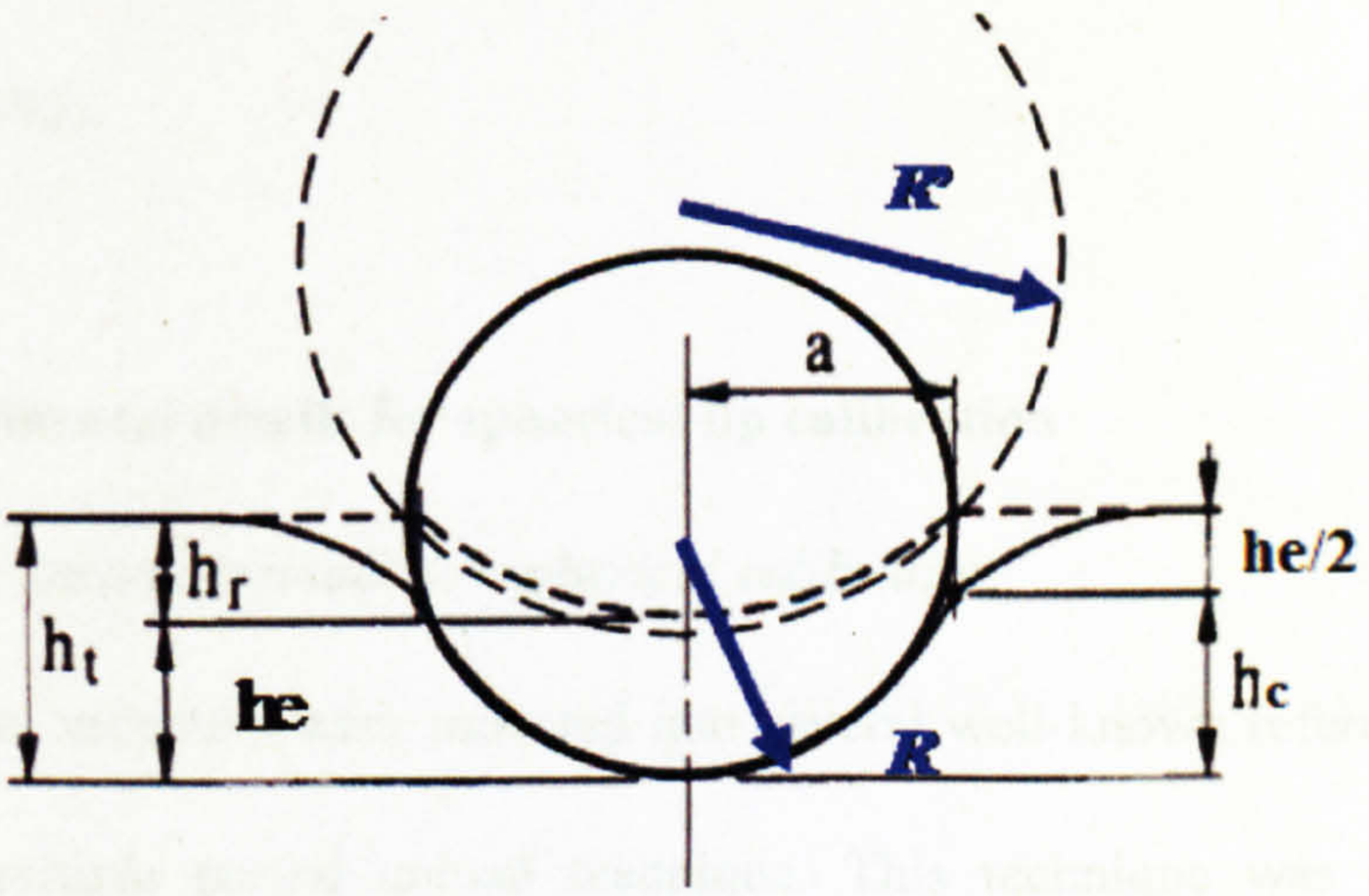

Figure 6.2 Schematic plot of relationship between the depth of loaded and unloaded indentations. (Modified from Field and Swain 1993, 1995)

The depth of the residual impression, h_r, that would occur on unloading from force F_1 can be calculated by applying Eq. (6.1) at points 1 (load) and 2 (unload) giving:

$$h_r = \frac{h_1 - \left(F_1 / F_2\right)^{2/3} h_2}{1 - \left(F_1 / F_2\right)^{2/3}} \tag{6.5}$$

This method assumes that the indenter radius is the same at points 1 and 2. Such an assumption is reasonable and does not introduce significant errors providing the partial unloading step is small (typically $F_2 = 0.75F_1$) and the indenter radius does not change by more than a factor of 2 over the full range of indentation depth.

The depth in contact with the indenter, h_c, can then be calculated using the result of Sneddon (1965) as:

$$h_c = \frac{h_1 + h_r}{2} \tag{6.6}$$

This result assumes that the indenter is effectively rigid and that there is negligible lateral shrinkage in the plane of the indented surface on unloading and gives the same result as that calculated by analysis of the unloading slope (Oliver and Pharr, 1992).

6.2.3 Experimental details for spherical tip calibration

6.2.3.1 Experimental methods for spherical calibration

Spherical indenters were indented into several well-known reference materials using the multiple partial unload technique. This technique was developed by Bushby and Jennett (2001). All nanoindentation tests were performed on UMIS 2000 instrument (CSIRO, Lindfield NSW, Australia). The equipment is able to control and record the penetration depth, force and time accurately. In other words, the raw data obtained from equipment are penetration depth, force and time.

Load controlled nanoindentation experiments are carried out, the true displacement into the surface for increment *i* is given by:

$$h_i = h_m + h_0 - C_f F_i \tag{6.7}$$

where h_m is the measured displacement, h_0 is a correction applied post-hoc for determination of the actual contact with the solid surface (by projection of the loading data to zero load or examination of the change in contact stiffness), C_f is the instrument frame compliance (typically ~ 0.2nm/mN) and F_i is the force for increment *i*. Correspondingly, the true displacements are determined.

Indenting into several reference materials of independently measured elastic properties allows the apparent indenter radius to be calculated using Hertzian mechanics.

Substituting Hertzian mechanics equations (6.4) and (6.3) into (6.1) and solving for *R* gives:

$$\left(2Qh_c^2\right)R^2 + (2h_r - 2h_c + Qh_r^2 - Qh_c^2)R + (h_c^2 - h_r^2) = 0 \tag{6.8}$$

where $Q = \frac{16}{9}\frac{E^{*2}}{F_1^2}h_e^3$, the positive root of which gives the apparent indenter radius for a given reference material.

The effective indenter radius, R_{eff} (h_c), can not be determined from indentation into a single reference material since in reality there are too many unknowns. The instrument frame compliance may be effected by the mounting of the indenter tip and the elastic constants used for the diamond may vary from indenter to indenter depending on the quality and orientation of the diamond. It is normally necessary to use indentation data from at least three reference materials covering as wide a

range of elastic modulus as possible in an iterative calculation process. R_{eff} is sensitive to the value of E^* (including the elastic constants of the indenter material) at low values of h_c whereas R_{eff} is sensitive to C_f at high values of h_c. Using reference materials with a wide range of elastic constants, these differences can be identified. Inserting known values for the elastic constants of the reference materials and iterating values for the frame compliance and the elastic constants of the indenter material, the effective tip radius and instrument frame compliance may be found to within a few percent uncertainty by superposition of all the data.

6.2.3.2 Material properties

The properties of the 4 reference materials used are tabulated in Tab.6.1. The choice of reference materials is important to ensure homogeneity, low surface roughness and minimal or no surface oxide.

Table 6. 1 Elastic constants of the reference materials

	Glassy Carbon[a]	Fused Silica[a]	Silicon (001)[b]	Tungsten[b]	Diamond (indenter)[b]
Elastic modulus (GPa)	36	72.9	168	410	1150
Poisson's ratio	0.2	0.16	0.16	0.29	0.07

[a] Young's modulus determined by the Surface Acoustic Wave technique (Herrmann et al. 2003).

[b] Apparent indentation modulus calculated for indentation of single crystals (Swadener *et al.* 2001)

6.2.4 Results and discussion for spherical tip calibration

Fig. 6.3 shows results of $R_{eff}(h_c)$ for three indenters. The superposition of the results for each indenter from all four of the reference materials, spanning an order of magnitude of elastic modulus, demonstrates that all parameters have been successfully calibrated. The indenter radii are close to their nominal values of 450nm, 3μm and 10μm, and the frame compliance is found to be $C_f = 0.24$nm/mN. The uncertainty in effective radius increases at low contact depths for all indenters due to the influence of surface roughness on both the reference material and indenter, and due to other near surface effects such as oxides and absorbed layers. However, at contact depths at which the yield pressure usually happened (denoted as red arrows in Fig. 6.3), the uncertainties are reduced to the order of a few percent. The uncertainty in determining the indenter radii is small compared to the difference in radius between the different tips used. These are important for studying the spherical indentation yield size effect as presented in chapter 7.

In total, six spherical tips were applied in this study, with the indenter radius ranging from 0.5 to 90μm.

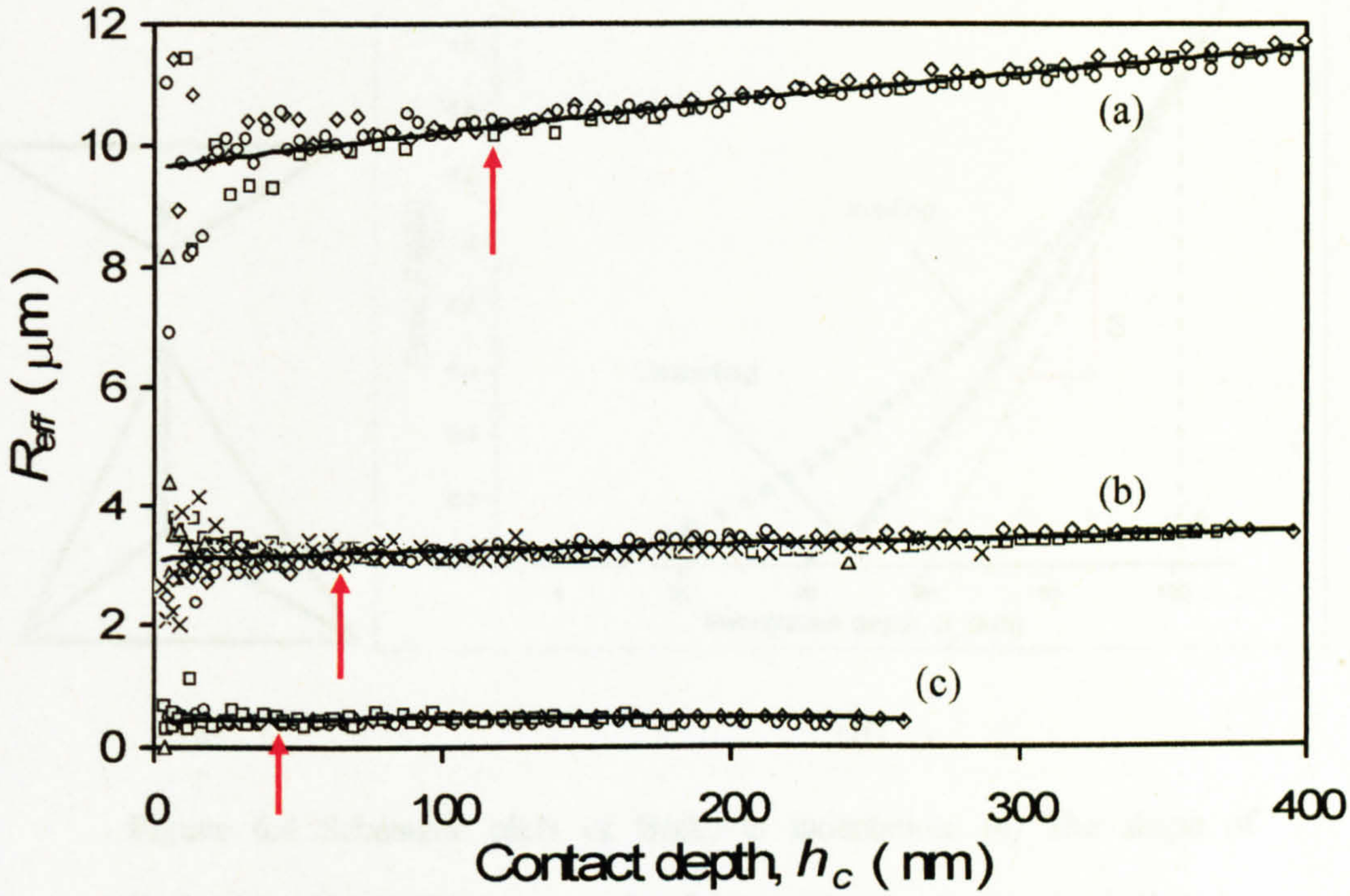

Figure 6.3 Effective indenter radius R_{eff} as a function of contact depth, h_c, for three indenter tips of nominal radii (a) 10μm, (b) 3μm and (c) ½μm, each indented into the four reference materials, glassy carbon (□), fused silica (◇), (001) single-crystal Si (○) and tungsten (×). The red arrows denote the contact depths at which the yield pressure usually happened

6.3 Berkovich indentation calibration

Pointed indenters are delicate, hence careful calibration is necessary. The shape of the Berkovich indenter is illustrated schematically in Fig.6.4 (a).

In this study, a Berkovich indenter was calibrated by indenting in to several reference materials using fully load-unload method (Oliver and Pharr, 1992).

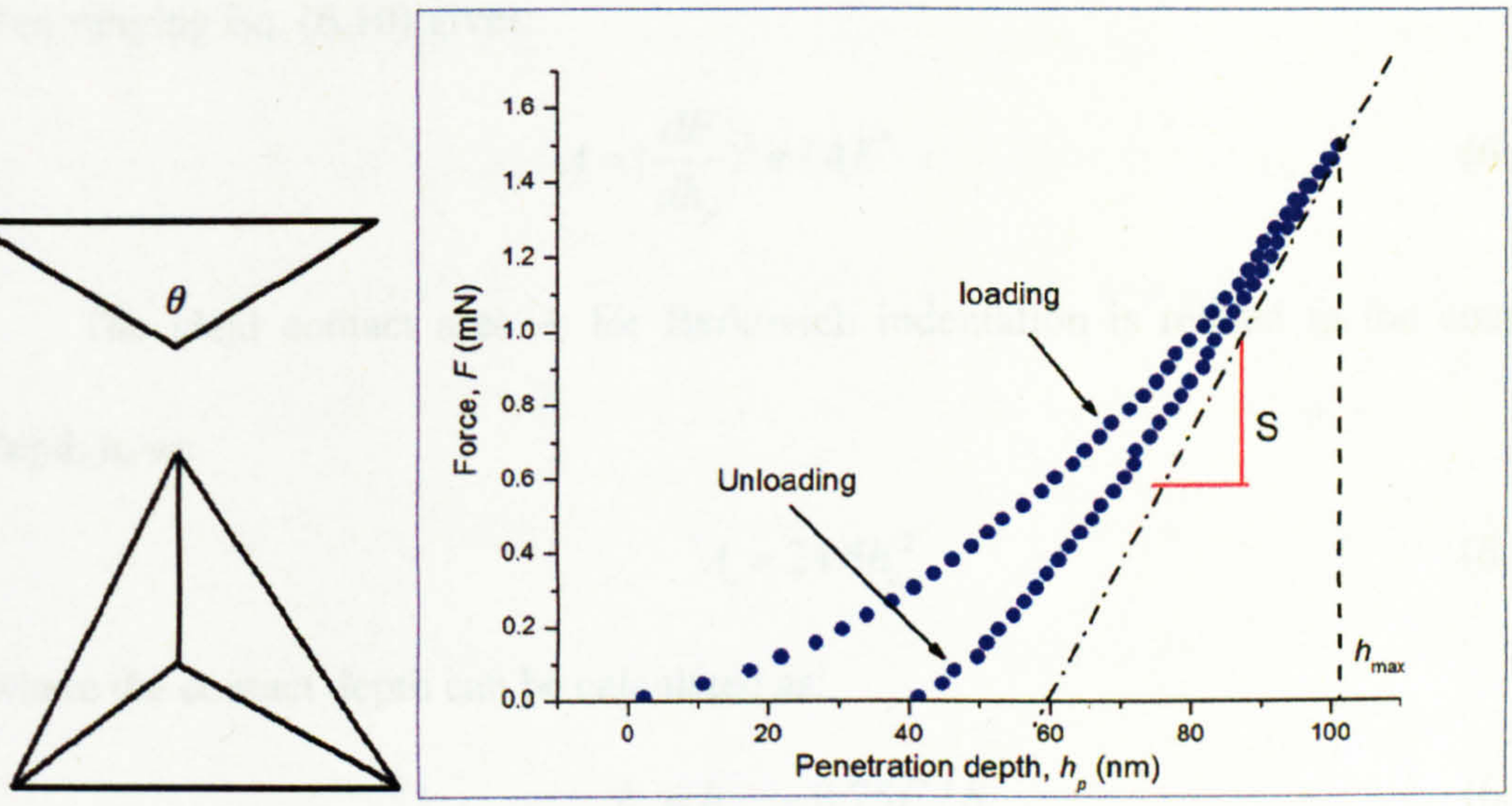

(a) (b)

Figure 6.4 Schematic plots of Berkovih indentation. (a) The shape of Berkovich indenter (b) An example of force (F) –penetration depth (h_p) plot by using fully load- unload technique. Stiffness S is defined as the slope of the initial portion of the unloading curve $\frac{dF}{dh_p}$.

6.3.1 Fully load-unload method for Berkovich indentation

Material response is detected throughout the fully load-unload cycle by recording the force F and penetration depth h_p. The analysis method follows Oliver and Pharr (1992).

Stiffness, S (in Fig. 6.4(b)) can be expressed as,

$$S = \frac{dF}{dh_p} = \frac{2}{\sqrt{\pi}} E^* \sqrt{A} \tag{6.10}$$

where $\frac{dF}{dh_p}$ is defined as the slope of the initial portion of the unloading curve, illustrated from the load-depth graph (Fig.6.4(b)). A is the actual area of indent.

Rearranging Eq. (6.10) gives:

$$A = (\frac{dF}{dh_p})^2 \pi / 4E^* \tag{6.11}$$

The ideal contact area A_i for Berkovich indentation is related to the contact depth h_c as:

$$A_i = 24.5h_c^2 \tag{6.12}$$

where the contact depth can be calculated as:

$$h_c = h_{\max} - 0.75F / S \tag{6.13}$$

in which $h_{\max}$ is the max penetration depth illustrated in Fig. 6.4.

6.3.2 Experimental details for Berkovich indentation calibration

The effective ratio of A / A_i is calibrated as a function of contact depth h_c, by indenting into three reference materials using fully load-unload technique. For every single reference material, the indenter was loaded over a range of different forces.

Three reference materials used were: glassy carbon, fused silicon and sapphire. Properties of materials are listed in table. 6.1.

6.3.3 Results and discussion of Berkovich indenter calibration

The calibration result of the Berkovich tip used here is shown in Fig. 6.5. This can be assumed as the profile of the tip without loading into materials. The effective ratio-depth curve is fitted by three different functions at different range depth for accuracy. The superposition of the results from all three of the reference materials,

spanning an order of magnitude of elastic modulus, demonstrates that all parameters have been successfully calibrated. The effective ratio is close to the theoretical value of 1, which means the shape of the indenter is relatively accurate (e.g., θ in Fig. 6.4(a)). The uncertainty in effective ratio increases at low contact depths for all indenters due to the influence of surface roughness on both the reference material and indenter, and due to other near surface effects such as oxides and absorbed layers.

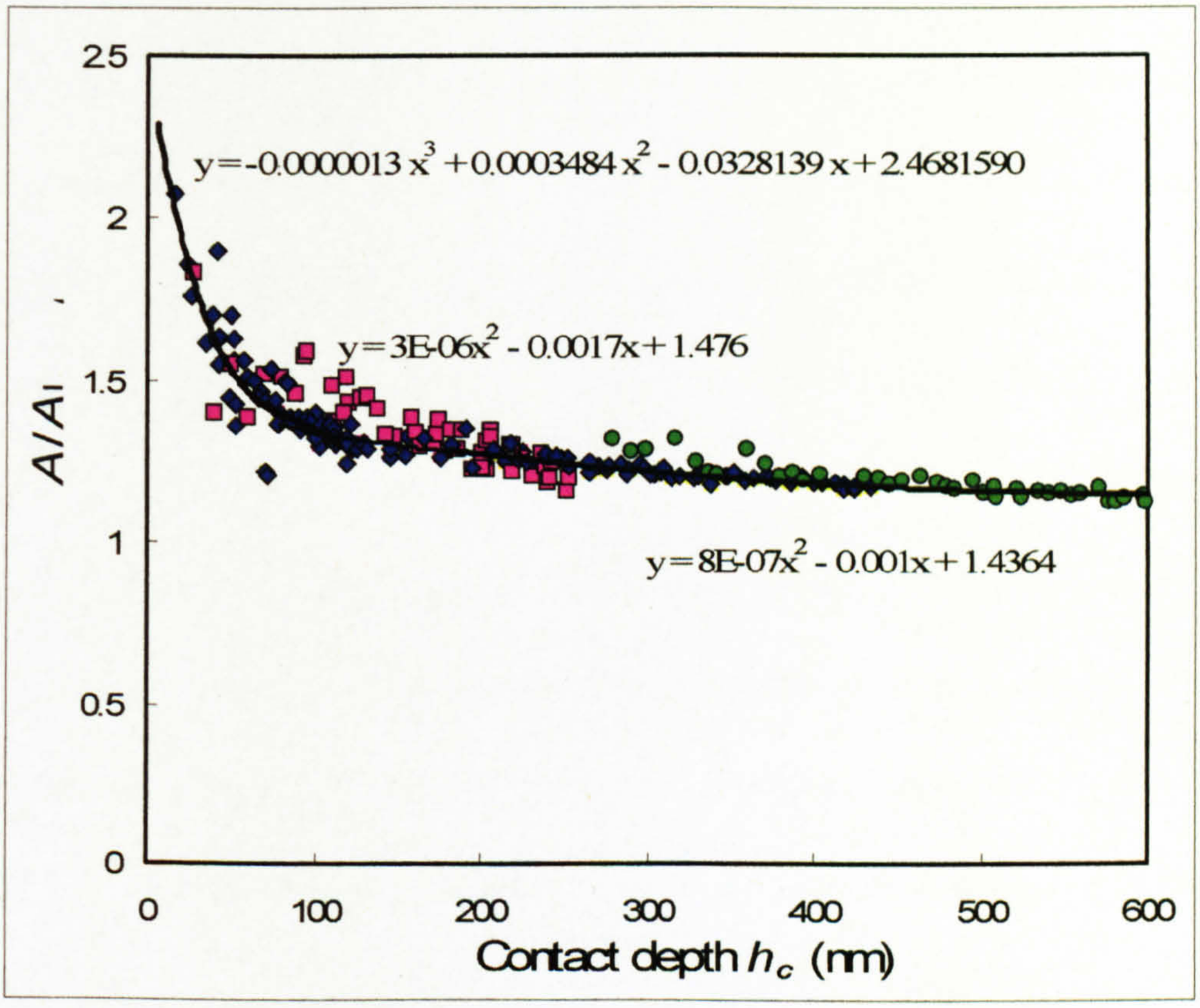

Figure 6.5 Effective indenter ratio A / A_i against contact depth, h_c, for Berkovich tip indented into the three reference materials: glassy carbon (green circle), fused silica (blue diamond), and sapphire (pink cube). This can be assumed as the profile of the tip without loading into materials. The black curves are fitted by three different functions at different depth ranges for accuracy. The fitting equations are illustrated in the graph.

6.4 Conclusions

For spherical indentation calibration, the uncertainty in R_{eff} is small compared to the difference in radius between the different tips used. R_{eff} is known with an uncertainty of a few percent, at depths which yield usually happens (Fig.6.3). These ensure the accuracy of study for spherical indentation yield size effect in chapter 7.

Berkovich indenter is successfully calibrated, which ensure the accuracy of the study of indentation size effect in chapter 7.

7 Size effect in nanoindentation

(In this chapter, the first part has been published in Journal of Mechanics and Physics of Solids and the latter part has been published in Journal of Physics D: Applied Physics)

7.1 Introduction and background

As reviewed in section 2.3.5, indentation size effects (with different indenter shapes) have been observed and reported repeatedly during the last two decades.

However, the study of the initial yield size effect via nanoindentation is limited in the literature. For pointed indenters, there is a significant flow starting from an early stage in the indentation cycle. Consequently, it is hard to observe the initiation of plasticity and few papers report size effects at yield, often manifest as the delayed onset of yield or 'pop-in' behaviour due to the low dislocation density and small strained volume (Gane and Bowdon, 1968; Goundstone *et al.*, 2000). Spherical indenters induce a larger area of contact at small depths, and this enables the entire stress-strain curve to be measured, including the transition from the elastic regime to plastic deformation. However, there are still difficulties in characterizing initial yield behaviour and defining a reproducible yield point. The yield strength of the ductile metals is so low that the elastic regime is below the resolution of the measuring system (Gouldstone *et al.*, 2000; Herbert *et al.*, 2006). In contrast, for hard ceramics, the main difficulty is the discontinuous yield phenomenon known as 'pop-in' (Syed Asif *et al.*, 1997; Leipner *et al.*, 2001).

Hence, the size effect in the initial yield strength was studied via indentation on a series of ceramics and tungsten in this thesis, because they have relatively high yield stress that nonetheless deform by dislocation glide or twinning. A rigorous method was demonstrated to determine the onset of plasticity in ceramics using spherical nanoindentation, even when pop-in occurs. This enables us to measure the well-defined and reproducible yield pressures of high-strength materials with a high degree of accuracy. Noted here, this yield is the 'fitted yield stress', which can be considered to represent the onset of gross or macroscopic plasticity.

In this study, a clear increase in yield pressure with decreasing indenter size is observed. When the data are normalised by their bulk yield pressure, the data for tungsten with bcc crystal structure follow the same relation as those of the previously investigated fcc metals (Spary *et al.*, 2006). All of the ceramics investigated also display a similar increase in the yield pressure that is proportional to the inverse cube root of indenter radius and when normalised, again, all data fall on a single line. However, the normalised data for metals and ceramics fall on lines of quite different gradient. That is, the magnitude of the size effect is different for metals and ceramics in spite of appearing to have a similar range of elastic modulus.

Another key result is that the yield stress of ceramics scales with the inverse cube root of R and that this scaling is experimentally indistinguishable from the inverse square root of contact radius, a. For pointed indenters, as addressed in chapter 2 (section 2.3.4), an increase in measured hardness, H, is usually associated with a decreasing indenter penetration depth, h_p, with the proportionality $H \propto 1/\sqrt{h_p}$

(Ma and Clark, 1995; Nix and Gao, 1998). However, h_p is known to be linearly dependent on the contact size a; for instance, in Berkovich indentation, $a \approx 2.8h_p$. So for both spherical and pointed indenters, it may be that the contact radius is the important parameter rather than h_p or R, and that indentation pressure might scale as the inverse square root of a. Here, the Berkovich and spherical indentation size effects of sapphire are compared. The results strongly support the idea that the indentation size effect is driven by the geometry of contact and inversely scaled by the square root of the contact size, independent of the shape of the indenter.

In this chapter, the method to find the yield strength for ceramics (with or without pop-in) and high strength metals is briefly introduced. Details were published in Zhu, *et al.* (2008a). This method is demonstrated to be comparable with Spary's (2006) method by testing tungsten. The results of yield size effect study are presented and discussed. The normalised yield pressure for tungsten (bcc) follow the same relation as those of the previously investigated fcc metals. However, the data for metals and ceramics fall on lines of quite different gradient. Remarkably, by comparing spherical and Berkovich indenter size effects, it strongly supports that a single length scale of the contact size dictates the geometrical part of the indentation size effect, independent of the shape of the indenter. The strength (yield pressure and hardness) is proportional to the inverse square root of the contact size. In conclusion, the magnitude of the size effect appears to be geometrical (from comparing bending results of copper and nickel in chapter 4; Spary *et al.*, 2006), but now material parameters are distinguished allowing theoretical deduction.

7.2 Experimental details

7.2.1 Experimental methods

Nanoindentation tests were conducted on a UMIS 2000 instrument (CSIRO, Lindfield NSW, Australia). A series of ceramic single crystals and a tungsten metal single crystal were subjected to nanoindentation. Each material was tested using the multiple partial-unloading method (Field and Swain, 1993; 1995) with different radius spherical indenters (from 450nm to 90μm) to determine the transition from elastic to plastic behaviour as a function of radius. In the partial-unloading method the indentation loading proceeds incrementally. Following each load increment to a force F_i, the load is reduced (partial unloading) by a small amount (in our experiments, to $0.75F_i$) before proceeding to the next higher load increment, F_{i+1}. Details have been given in chapter 6.

In the work of Spary *et al.* (2006), a different method was used to determine the indentation stress-strain relationship. They applied known indentation loads, and measured the contact radius, a, afterwards by atomic force microscope (AFM) or optical microscope. The only reason was to consider the pile-up effect of a, which is known to be a problem in soft metals (Lim and Chaudhri, 1998; 1999). Jayaweera *et al.* (2001; 2003) have verified the calculated value a by scanning electron microscope (SEM) and AFM for ceramics. At the elastic-plastic transition, no pile-up is anticipated (Jayaweera *et al.*, 2001, 2003). The method of calculation a in this work was from Field and Swain (1993, 1995). Details were described in chapter 6 and elsewhere (Field and Swain, 1993; 1995; Bushby, 2001).

Knowing a as a function of indentation load, F, two important plots can be obtained. Firstly, the indentation stress-strain curve can be plotted. The indentation stress is defined as the mean pressure acting over the projected contact area,

$$P_m = F / \pi a^2 \tag{7.1}$$

The indentation strain is expressed as,

$$a / R \tag{7.2}$$

The indentation strain is a normalised contact dimension which expresses the geometry of the contact regardless of the spherical tip radius (Bushby, 2001). Then the plot of P_m against a / R is the so-called indentation stress-strain curve.

Secondly, the elastic modulus-depth plot can be obtained. This provides a very useful tool to confirm the quality of the data, since elastic modulus is a well-known material constant.

Sapphire is indented by the Berkovich indenter using fully load-unload technique (Oliver and Pharr, 1992). The load cycle was: load to maximum force collecting 40 data points; hold for 30s; unload to zero collecting 40 data points; and hold at 10% of maximum force for 30s to assess thermal drift. The force – displacement data were analysed using the method of Oliver and Pharr (1992) to determine the contact depth as described in chapter 6. The projected area of contact, A, is then found from the shape function for the indenter appropriate to the contact depth, h_c, and the mean pressure expressed as hardness, $H = F/A$.

7.2.2 Materials

The materials investigated here are: (i) sapphire, α-Al_2O_3 $(11\bar{2}0)$-oriented single crystal; (ii) a 2.5μm thick layer of $In_xGa_{1-x}As$ grown epitaxially on InP (100)-oriented single-crystal substrate with $x = 0.53$, so that the $In_{0.53}Ga_{0.47}As$ (IGA) was lattice matched to the InP with no coherency strain; (iii) InP (100)-oriented single crystal; and (iv) GaSb (100)-oriented single crystal. (v) W (100) oriented single crystal. The properties of these materials are given in table7.1. The properties of four metals used by Spary *et al.* (2006) are also tabulated in table7.1 for comparison later.

Table 7.1 Properties of materials studied

	Crystal structure	**Grain size / μm**	***E*** / GPa* **Indentation modulus**	***v*** **Poisson's ratio**	***μ* / GPa** **Shear modulus**	***b* / nm** **Burger's vector**
Sapphire	Hexagonal	Single crystal	428[a]	0.22[c]	150	0.475
InP	Zinc-blende	Single crystal	91[a]	0.36[c]	22.5	0.414
IGA	Zinc-blende	Single crystal	93.8[a]	0.33[c]	28.9	0.413
GaSb	Zinc-blende	Single crystal	86.5[a]	0.31[c]	24	0.430
W	bcc	Single crystal	400[b]	0.29[b]	140	0.240
Al	fcc	330±40	70[b]	0.35[b]	26.5	0.286
Cu	fcc	70±30	125[b]	0.34[b]	43.5	0.256
Ni	fcc	45±15	220[b]	0.31[b]	78.6	0.249
Ir	fcc	30	510[b]	0.26[b]	202	0.272

[a] Apparent indentation modulus calculated for indentation of single crystals (Swadener and Pharr, 2001)

[b] Spary *et al.*, (2006)

7.3 Determination of yield -- gross yield point in spherical indentation

The yield pressure is normally identified as the first deviation from the elastic behaviour on the indentation force-depth plot or the stress-strain curve. However, most of the indentations in the ceramics studied here do not give a well-defined yield point in this sense, because of discontinuous yield, an abrupt jump in penetration depth. This phenomenon is often called "pop-in" behaviour. For small indenters and single crystal specimens, it is a common phenomenon, due to the small contact volume and few dislocations before loading. It is not our purpose to analyse the phenomenon of pop-in; that has been done adequately elsewhere (Syed Asif *et al.*, 1997; Gouldstone *et al.*, 2000). However the pop-in behaviour gives us a discontinuous force-depth plot and stress-strain curve. Here, the few continuous data sets were used and a method was developed to determine a well-defined and reproducible yield pressure. Then, it is demonstrated that this yield pressure can be determined without significant error from the majority of indentations in which pop-in occurs. Details of determining this method were published in Zhu *et al.* (2008a). Here, only the method is described.

For indentation data, the stress-strain curve is the plot of indentation stress (P_m) against indentation strain (a / R). The elastic region of this plot (solid lines in Fig. 7.3.) can be predicted from independent measurements of elastic modulus and has a

slope of $3\pi / 4\ E^*$

$$P_m = \frac{4E^*}{3\pi}\left(\frac{a}{R}\right) \tag{7.3}$$

where E^* is the indentation modulus. The theoretical elastic line is plotted using E^* = 93.8GPa value from table 7.1 as the solid line in Fig. 7.3.

The plastic part of the plot is described by Meyer's law (Tabor, 1951),

$$P_m = k\left(\frac{a}{R}\right)^n \tag{7.4}$$

where k and n are material constants. The exponent n assumes power law hardening for the material and typically has a value between 0 for perfect plasticity and 0.7 for ductile metals. In our data the elastic region is well defined, due to the relatively high yield stress of the materials chosen, and the departure from the elastic line is clear. A power law curve could be fitted to the plastic part of the plot if necessary. Fig.7.1 shows a typical example of yield determination. The yield point is defined as the intersection of the elastic line and the fit to the plastic curve for both continuous data and for data with pop-in. Details were published in Zhu *et al.* (2008a)

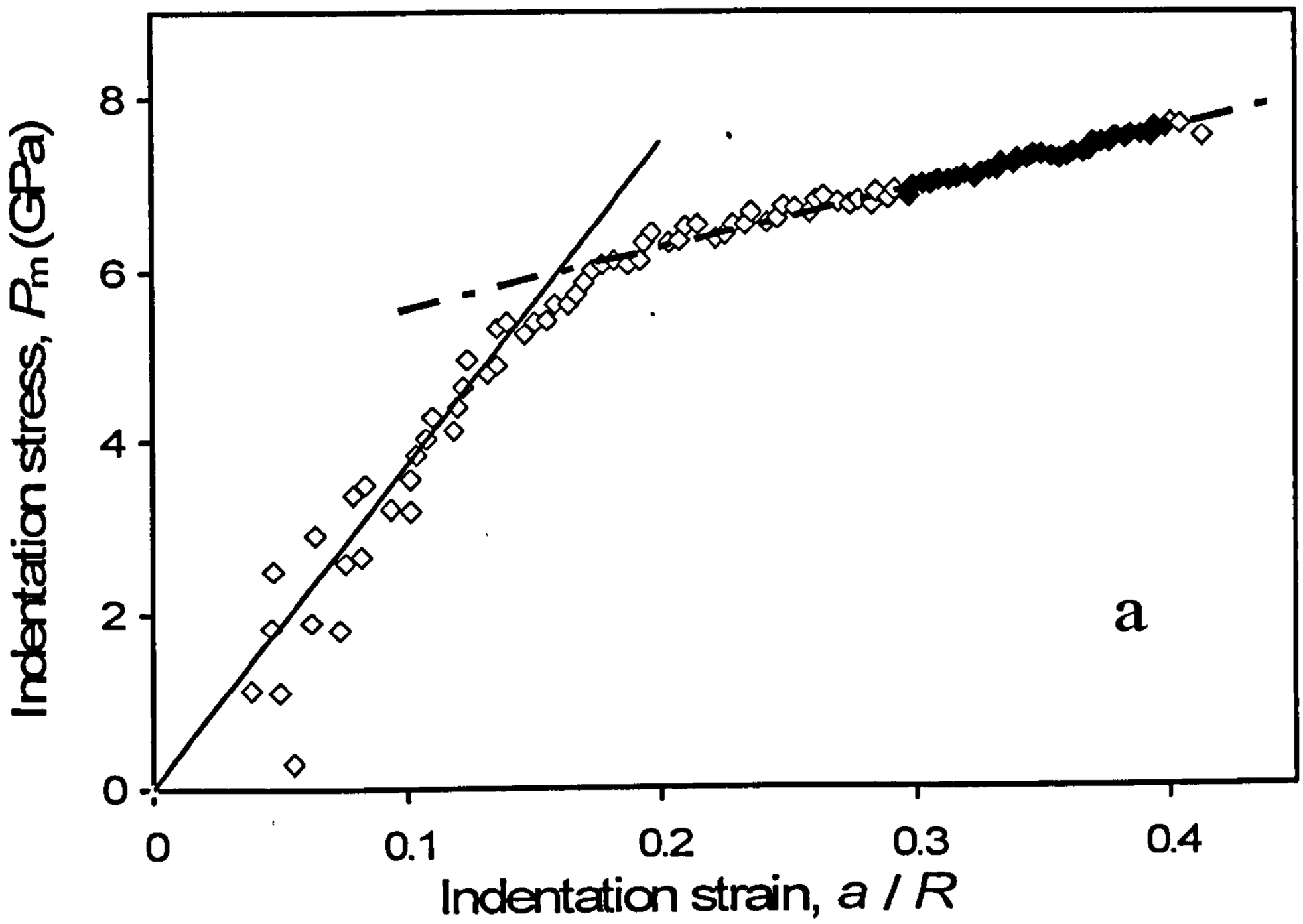

Figure 7.2 The indentation stress-strain curves of InGaAs. The solid line is the theoretical elastic line and the dotted line is the linear regression fit to the data in the plastic region. The yield point is defined as the intersection of the dotted and solid lines. (a) a continuous data set, (b) a data set with 'pop-in'.

7.4 Results and discussion

7.4.1 Indentation yield size effect

Indentation stress–strain data for sapphire are plotted in Fig.7.2 (a) for three different indenter radii (R = 0.5, 3 and 10μm). The solid line represents the theoretical elastic response (as in Eq. (7.3)). In Fig. 7.2(a), data have been chosen that display a smooth transition from elastic to plastic response (dashed line). However, $In_{0.53}Ga_{0.47}As$ or InP mostly showed pop-in behaviour, especially for smaller indenters, since they possess low dislocation density.

Also for the same three data sets, the experimental elastic modulus calculated from the data is plotted against the contact depth in Fig. 7.2 (b). The elastic modulus is about 435GPa, which is very comparable with theoretical calculation by Swadener and Pharr (2001) method for anisotropic materials (listed in table 7.1). Also, the modulus is seen to be constant with contact depth and does not change for different radius indenters whereas the pressure at yield (P_y) increases significantly in Fig.7.2 (a) for smaller radius indenters. Furthermore, the elastic modulus does not change significantly at the elastic-plastic transition. An apparent reduction in elastic modulus would indicate a cracking event rather than yielding (Bushby, 2001).

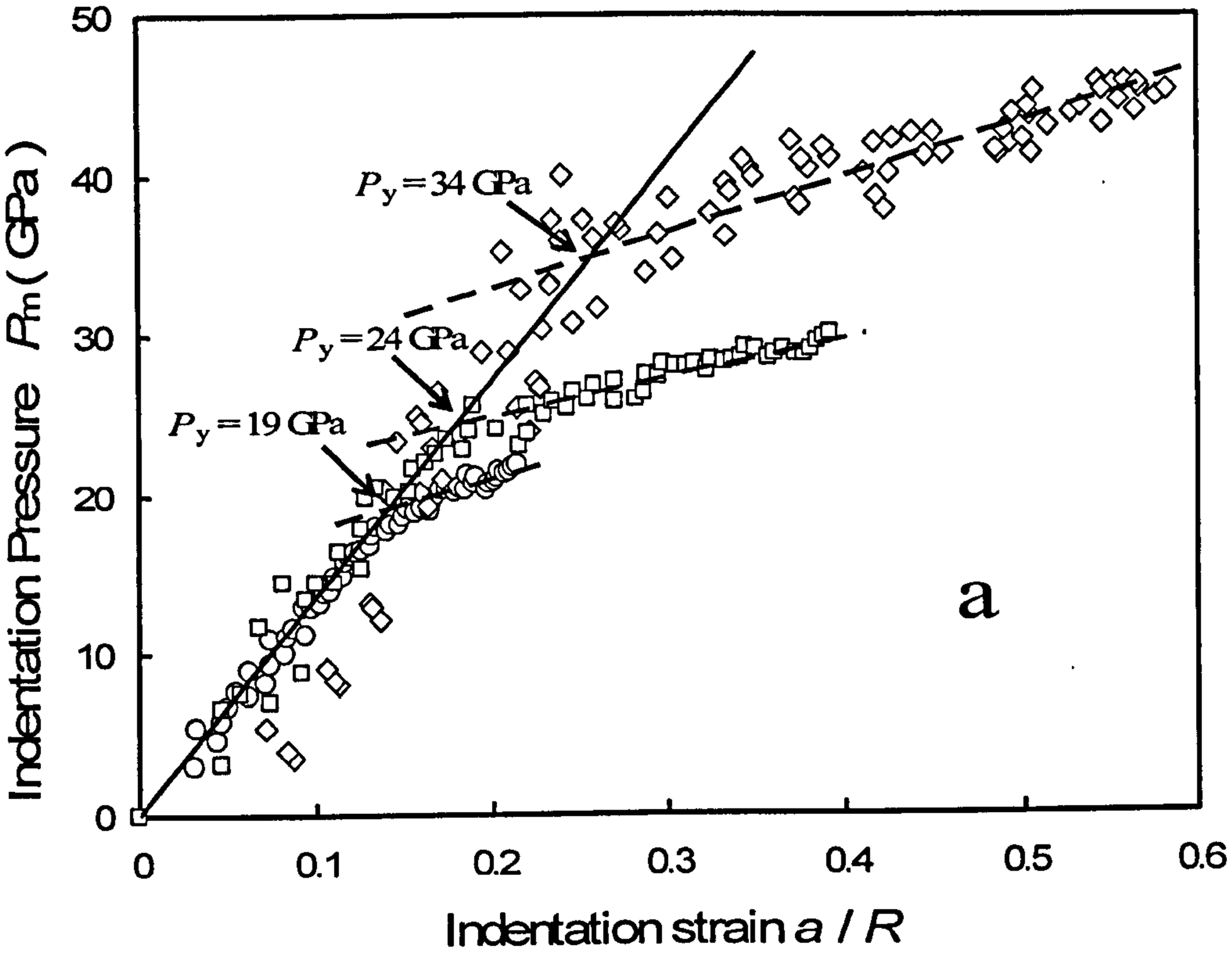

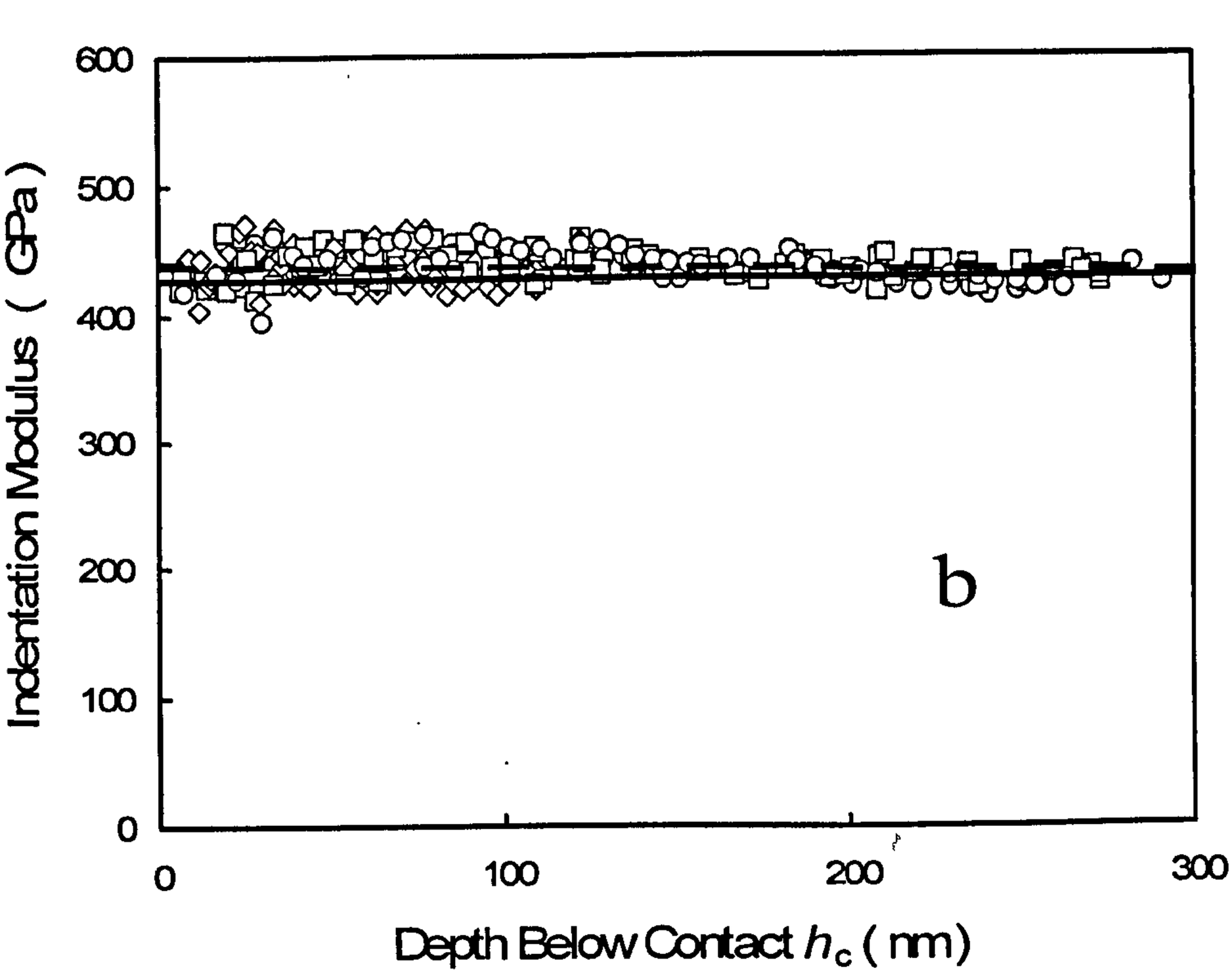

Figure 7.3 α-Al_2O_3 was indented by indenters of nominal radii ½ μm (◇), 3 μm (□) and 10 μm (○). In (a), the indentation stress–strain curves are plotted. Yield pressure has been marked in the graph. The solid line is the theoretical

elastic line. The dotted line is the linear regression fit for plastic part. In (b) the elastic moduli generated from the same raw data set are plotted against contact depth, h_c. The solid line is the theoretical value of indentation modulus (table 7.1).The dotted line is linear regression fits for all data.

Indentation stress-strain curves for the single crystal of tungsten were generated with a range of indenter radii (R = 3μm, 10μm 30μm and 90μm) using the partial unloading technique (open symbols in Fig. 7.3(a)). The theoretical Hertzian elastic response is plotted as the solid line. Again, a clear departure from the elastic line was observed, which denotes the yield pressure, P_y, which is seen to increase as indenter radius decreases in a similar manner to that observed for the ceramic materials. Noted, it is clear that some non-elastic deformation has taken place before P_y. However, here the concern is the onset of gross or macroscopic plasticity as claimed in section 7.1.

Also included in Fig. 7.3(a) are two data sets from the same material using the approach of Lim and Chaudhri (1999) and the method described for experiments on nickel in Spary *et al.* (2006) (solid symbols in Fig 7.3(a)). In this method the contact area is not determined from the nanoindentation data but directly from metrological scanning probe microscopy measurements for the 7μm radius indenter and from optical microscopy for the 90μm radius indenter. It can be seen that these two methods are very comparable considering the relative uncertainties in each method.

The experimental elastic modulus calculated from the same four data sets are plotted against the contact depth h_c in Fig. 7.3 (b). The value is about 400GPa, which

is reasonable (listed in table 7.1). Furthermore, the elastic modulus does not change significantly at the elastic-plastic transition. A slight reduction in measured value would be associated with sink-in (Bushby, 2001).

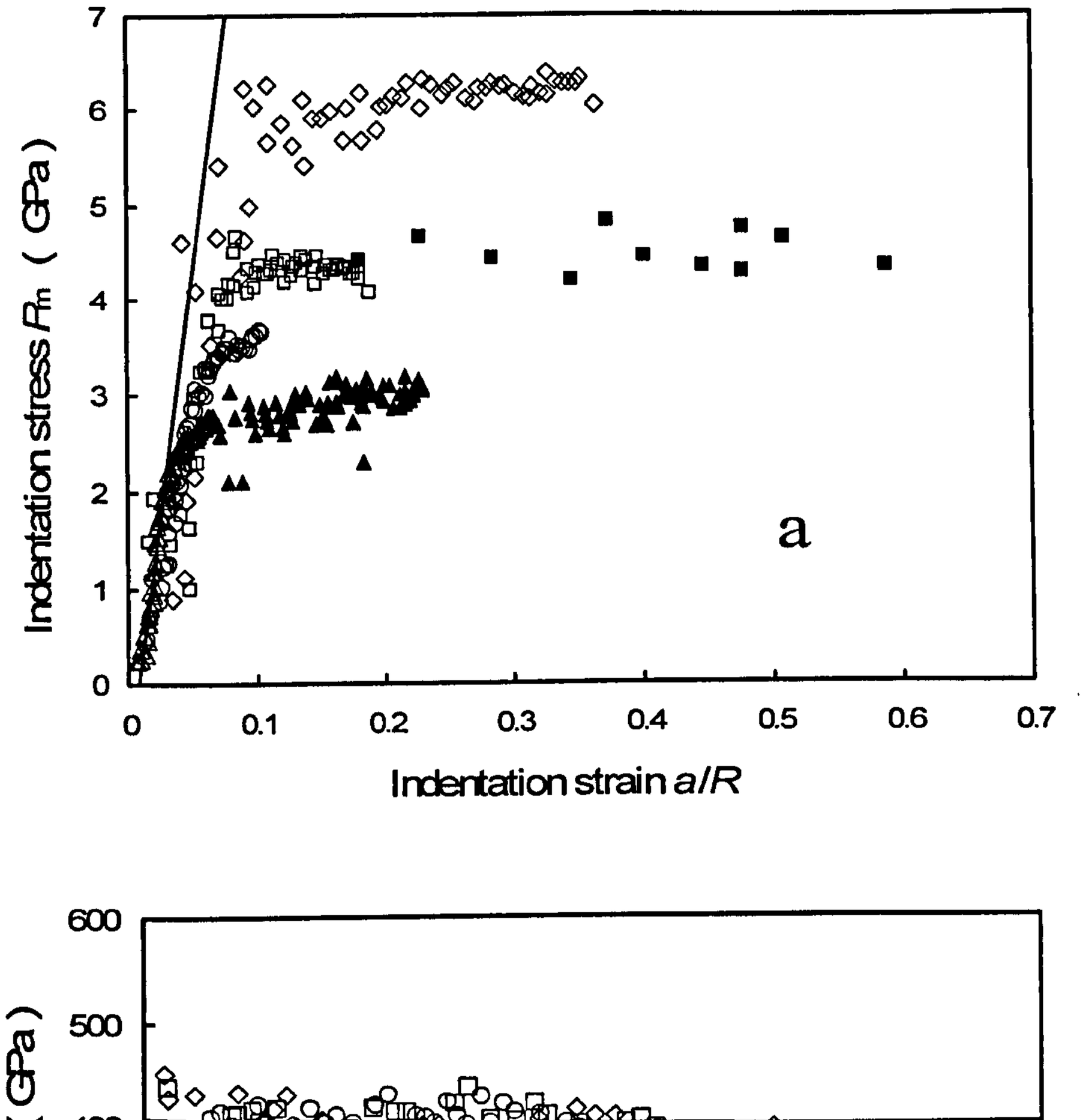

Figure 7.3 Tungsten stress-strain curves were plotted in (a) Partial unloading indentation and contact area is calculated (illustrated as open circles) indenters

of nominal radii 3μm (◇), 10μm (□), 30μm (○) and 90μm (△). Fully unload indentation have been taken and the contact area is determined directly (Lim and Chaudhri, (1999)) and treated as solid circles. Nominal radii of indenters are 7μm (■) and 90μm (▲). The solid line is the theoretical elastic line. In (b), the elastic modulus generated from the same data is plotted against contact depth, h_c. The solid line is the theoretical elastic modulus line (table7.1 for W). The dotted line is the linear regression fit for all data.

A clear increase in yield pressure with decreasing indenter size is seen in Fig.7.3(a), while the measured elastic response remains constant and close to the theoretical value for all indenters. The yield pressure, P_y, for each of the four ceramics tested is plotted in Fig. 7.4 (a) as a function of the inverse cube-root of indenter radius, $R^{-1/3}$. The error is the standard deviation of 49 tests I made for each data point in the plot. Linear fits to the data for each ceramic are shown as solid lines. The yield pressure seem to scale linearly with the inverse cube-root of indenter radius, $R^{-1/3}$, for all of the ceramics, is in agreement with Gerberich *et al.* (2002) and Spary *et al.* (2006) for metals. However, in the present data set there is significantly less scatter than for the metals, due to the well-defined reproducible yield point in the ceramics, and so the relationship with R is unambiguous. The yield pressure P_0 in the absence of a size effect, or for an infinite indenter radius, is defined in Fig. 7.4(a). Normalizing by P_0, Fig 7.4(b) shows that the data fall on a single line even though their P_0 values vary by a factor of 6. This result is also similar to the data for fcc metals (Spary *et al.*, 2006) but again with less scatter.

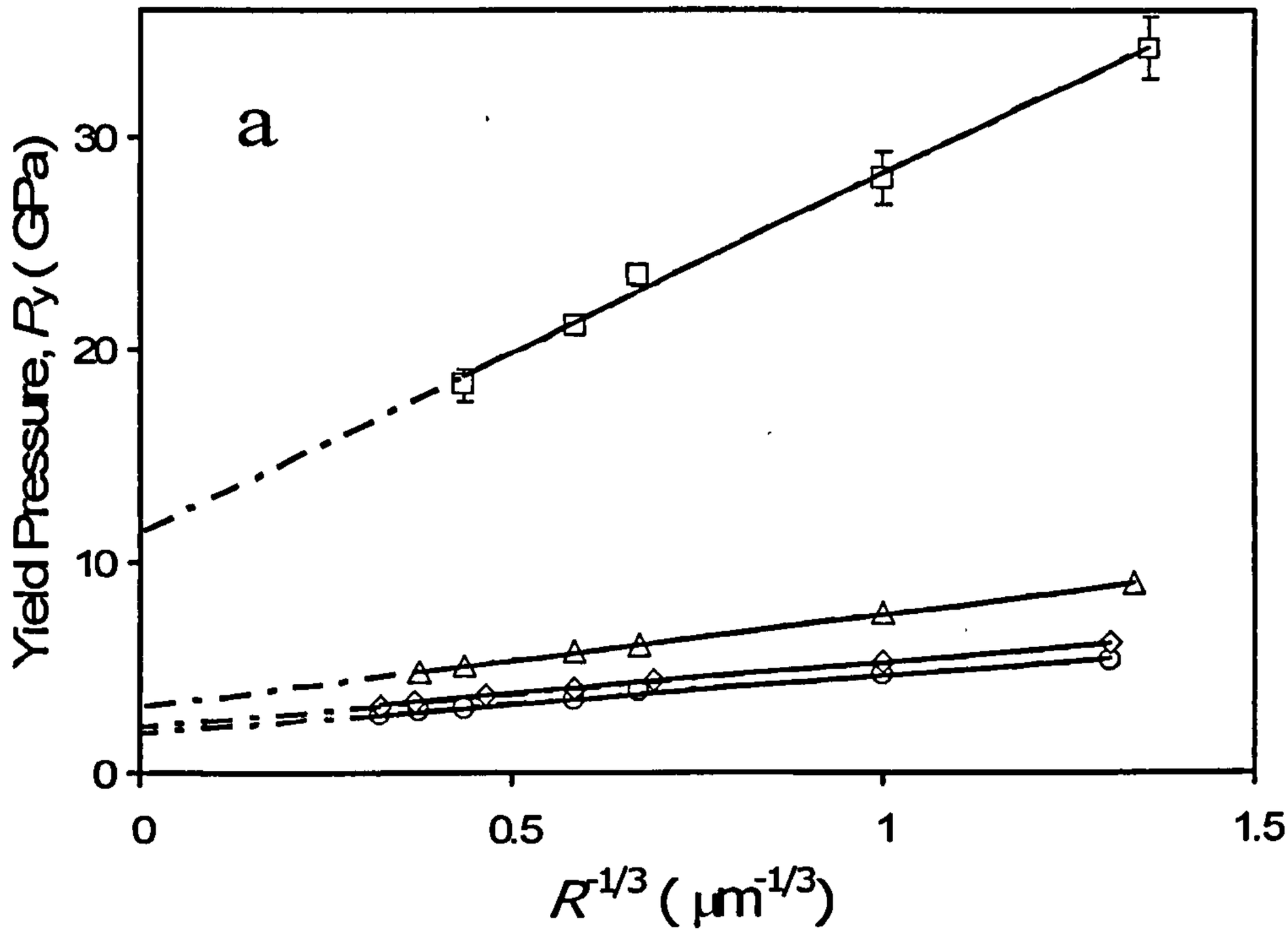

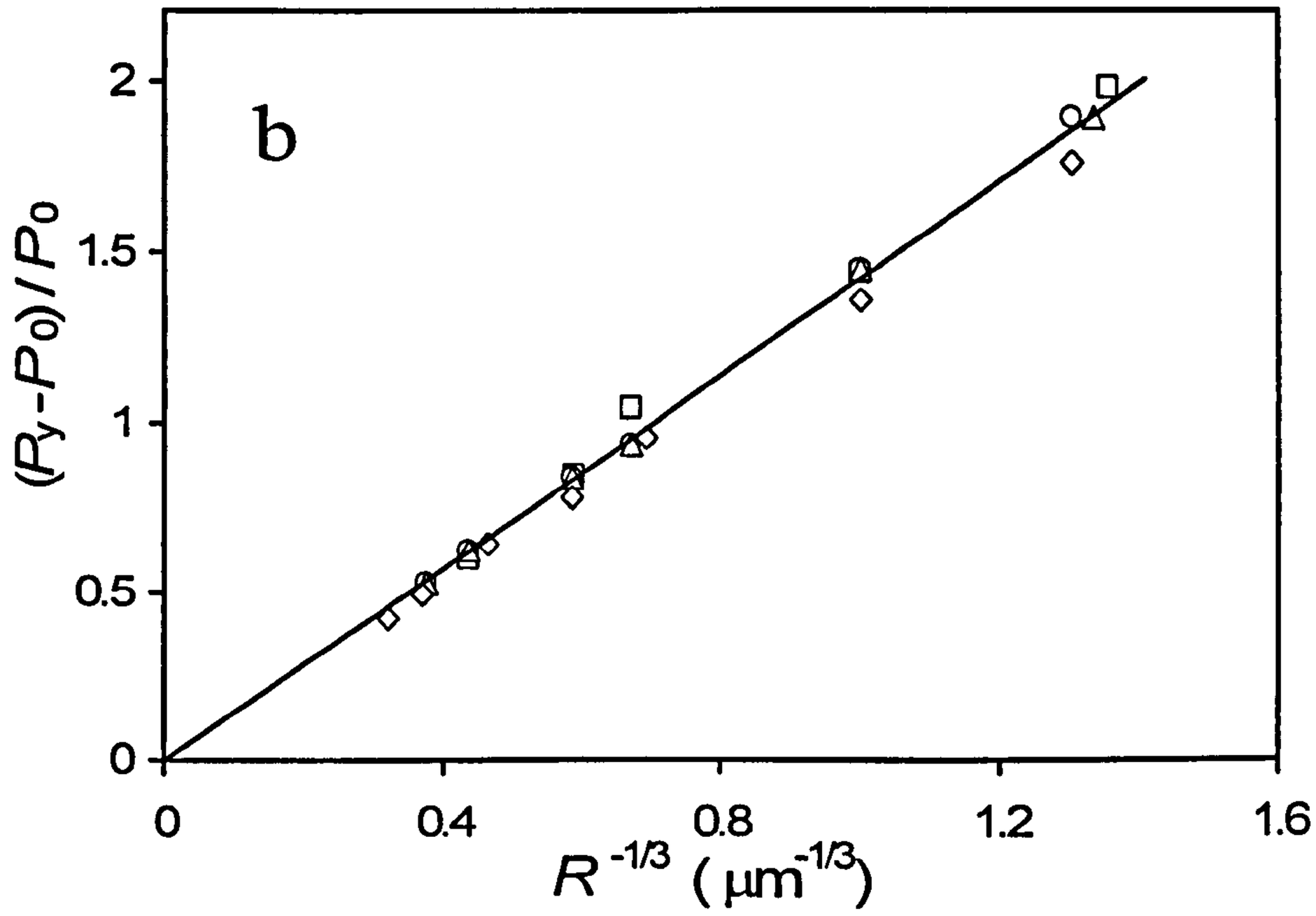

Figure 7.4 In (a) P_y are plotted for sapphire (□), InP (○), InGaAs (△) and GaSb (◇) against $R^{-1/3}$. The solid lines are linear regression fits to the data. The intercepts are the yield pressures P_0 that would be expected for infinite indenter radius. In (b) the yield pressures normalised by P_0 are plotted and the solid curve is a single linear regression fit to the data for all four materials.

In Fig. 7.5, the normalised yield pressure is plotted for tungsten as a function of the inverse cube root of indenter radius. The data for the fcc metals from Spary *et al.* (2006) are included on the plot. They determined the equivalent tensile yield strength for each metal required to simulate the indentation data for each indenter radius using a FEA modelling method. These values were normalised by the uniaxial yield strength from bulk compression tests. Comparing these normalised values to our normalised yield pressure values for the bcc tungsten, it illustrates that they are in excellent agreement (as shown in Fig.7.5). The data appeared more scattered about the regression line than for the ceramics, due to the greater uncertainties associated with determining the (relatively low) yield point of the fcc metals that are fully discussed in Spary *et al.* (2006). Fig.7.5 also includes the ceramics data regenerated from Fig.7.4 (b). The Fig.7.5 illustrates that the metallic materials and ceramic materials fall on lines with quite different slopes. That is, the rate of increase in yield pressure with decreasing indenter radius is much greater for metals.

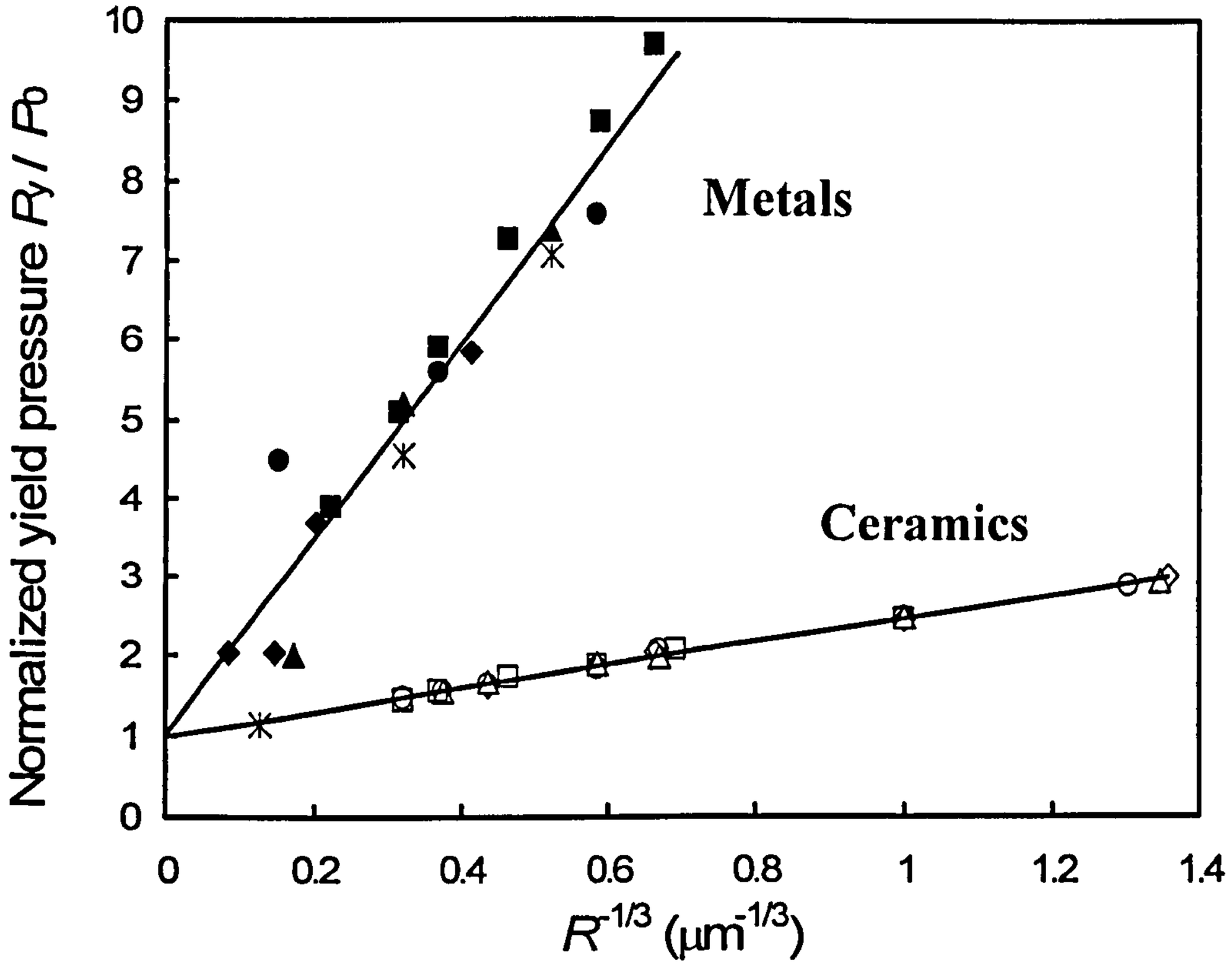

Figure 7.5 Normalised yield pressures are plotted for metals W (■), Al (▲), Cu (∗), Ni (●), Ir (◆) and ceramics, open circle, Al_2O_3 (□), $In_{0.53}Ga_{0.47}As$(△), GaSb (◇), InP (◇) against $R^{-1/3}$.

A more useful descriptor of the geometry of contact for both pointed and spherical indenters might be the contact area, characterized by the size of contact, a. In Fig.7.6, the yield pressure (P_y - P_0) normalised for P_0 is plotted against the inverse square root of the contact radius a for tungsten and ceramics, calculated directly from the raw data. All of the data of ceramics again falls on a straight line. The tungsten and ceramic materials again fall on lines with quite different slopes. The gradient for the metal is about 3 times steeper than the gradient for ceramics. Here the data are slightly more scattered than in Figs. 7.4(b) and 7.5, since in Figs. 7.4(b) and 7.5, the measured values of a and their random errors now appear in both the

ordinate and abscissa, whereas in Figs. 7.4(b) and 7.5 the data are plotted against the independently determined indenter radius *R*. Noted, the other metals studied in Spary *et al.* (2006) are left out, because it was impossible to measure the *a* at yield, from their method.

The fact that the magnitude of the size effect is greater in metal than ceramics shown in Fig. 7.6, implies very strongly that the material parameters must play a role in determining the magnitude of the indentation size effect, as well as the geometry of the indentation stress field. These results are similar to Fig.7.5, in which the normalised yield pressure against the inverse cube root of indenter radius was plotted. In that case, it enables us to compare our data to the earlier work of Spary *et al.* (2006), and showed that the tungsten displayed the same magnitude of normalised size effect to that of a range of fcc metals.

Referring to table7.1, it is seen that both the metals and ceramics presented here include a variety of crystal structures. All of the materials are either single crystal or have relatively large grain sizes so that the influence of grain size is only likely to affect the indentations made with the large indenters (data for metals only). The range of elastic modulus for both the metals and ceramics cover an equally wide range. The Burger's vectors for the ceramics are about twice that of the metals. However, it is not apparent how this difference could account for these differences in the relative rate magnitude of the size effect here (Figs. 7.5 and 7.6).

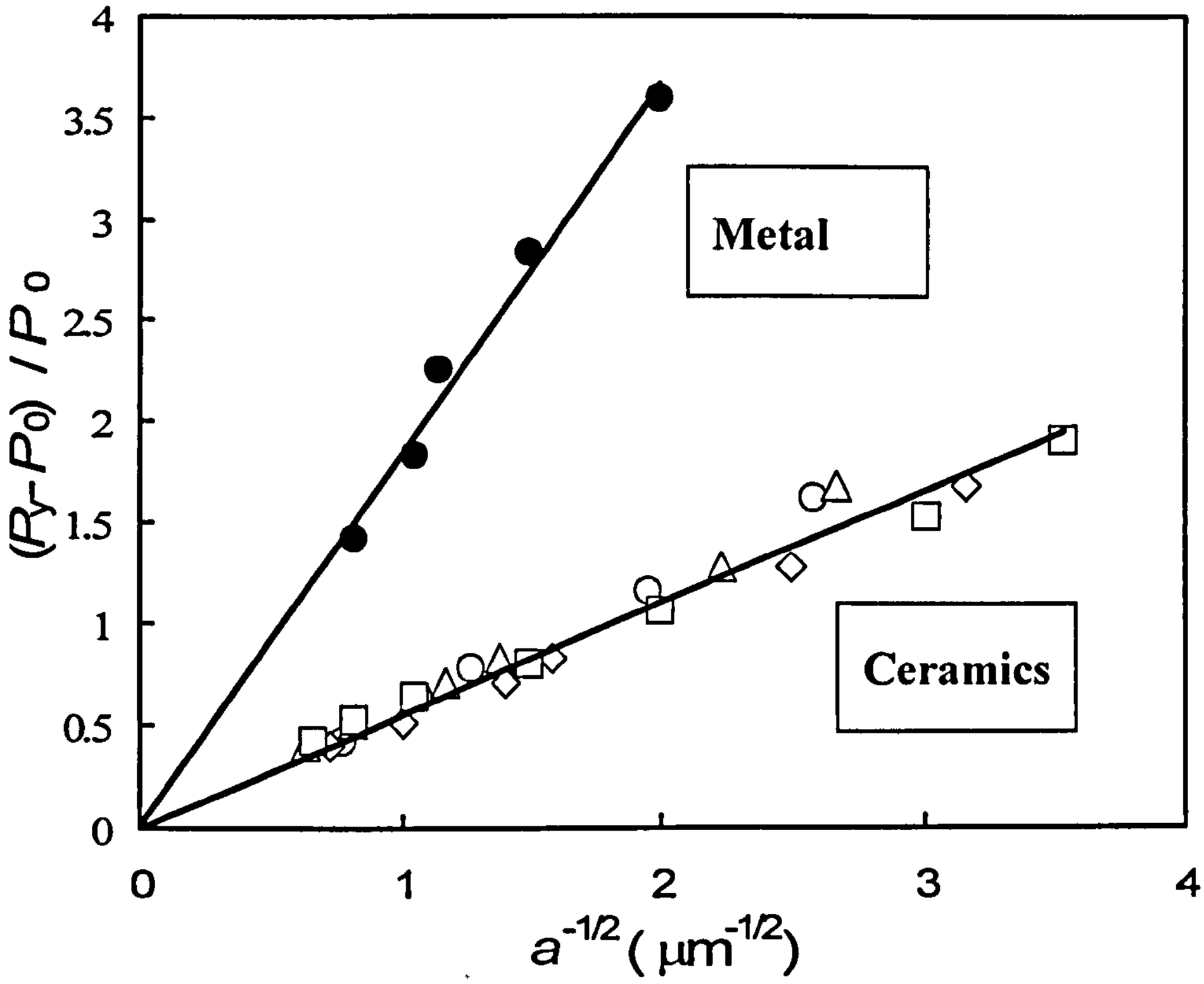

Figure 7.6 Normalised yield pressure $\frac{P_y - P_0}{P_0}$ against $a^{-1/2}$ is plotted for α-Al_2O_3 (○), InP (□), InGaAs (△) GaSb (◊) and W (●) as function of $a^{-1/2}$. The solid lines are linear regression fits for the data. For tungsten, $P_y = 1.83a^{-1/2}$; for all ceramics, $P_y = 0.552\ a^{-1/2}$.

In the indentation work of Spary *et al.* (2006) and bending work reported in chapters 3 and 4, all the materials investigated are soft metals. The conclusion was that the size effect is geometrical. However, the material parameters are extended here by studying the indentation size effect on ceramics together with metals. This allows the material parameters to be distinguished and hence helpful for theoretical deduction.

7.4.2 Length scale study in indentation size effect

If the indentation size effect, that is increase in yield strength, is proportional to $1/a^{1/2}$ for spherical indenters (as shown in Fig.7.6), it is interesting to see if the same is true for pointed indenters and the hardness size effect. In the literature for pointed indenters, most papers discuss the hardness size effect for metals and consider that the hardness depends on penetration depth h_p. This contrasts with spherical indenters, for which yield point and R, or here a, are proposed as the relevant variables rather than hardness and h_p.

In Fig.7.7, values of P_y are plotted for sapphire as a function of the inverse square root of contact size, a, for five spherical indenters with different radius. Also plotted are the hardness values obtained with the Berkovich indenter as a function of the smallest contact dimension, calculated as the square root of projected contact area divided by $3\sqrt{3}$. The Berkovich data are seen to superimpose on the spherical data extremely closely. The regression fits have almost the same slope, although the fit to the Berkovich data this is strongly influenced by the smallest contact sizes. This is an extraordinary result, since the spherical data were determined at the onset of gross yielding, while the Berkovich data are determined after some plastic deformation. Furthermore, the shape of the contact areas are quite different for the two indenter geometries and one would expect the shape of the edge of contact and, particularly, the corners of the Berkovich indentions to have a pronounced influence. These results strongly support the argument that the important length scale in the indentation size effect is determined by the contact size. The contact size a, might be

the most important characteristic length scale, but not penetration depth h_p and/or indenter radius R.

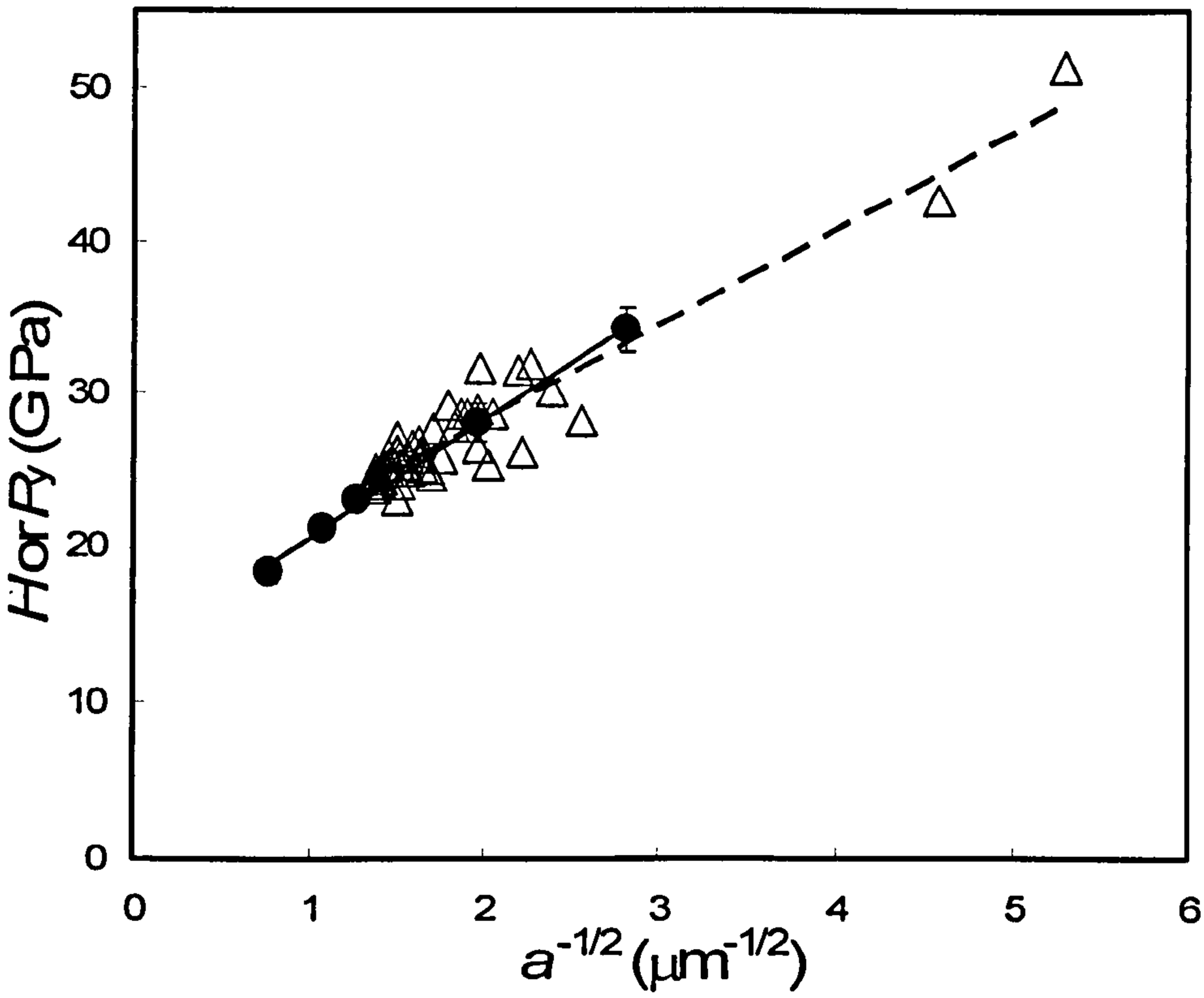

Figure 7.7 Yield pressure (spherical indenters ●) and hardness (Berkovich indenter Δ) as a function of inverse square root of smallest contact length for indents in sapphire. Solid line is a regression fit to the data from spherical indenters. The dashed line is a regression fit to the data from the Berkovich indenter.

7.5 Conclusions

The gross or macroscopic yield strength for ceramics (with or without pop-in) and high strength metals is determined. This method is demonstrated to be comparable with Spary's (2006) method by testing tungsten.

When the data are normalised by their bulk yield pressure, the data for tungsten (with bcc crystal structure) follow the same relation as those of the previously investigated fcc metals. However, the normalised data for metals and ceramics fall on lines of quite different gradient. This implies the material parameters played an important role in length scale plasticity.

By comparing Berkovich and spherical indentation size effect of sapphire, the results implies that a single length scale of the contact size dictates the geometrical part of the indentation size effect, independent of the shape of the indenter. The indentation strength (yield pressure and hardness) is found to be proportional to the inverse square root of contact size.

In conclusion, contact size, a, is the universal scaling factor for the indentation size effect. The magnitude of size effect appears to be geometrical (chapter 4; Spary *et al.*, 2006), but now material parameters are distinguished allowing theoretical deduction.

A possible theoretical explanation is given in chapter 8.

8 Analysis of the inverse square-root size effect in the plasticity of metals and ceramics

(Part of this chapter is published in Journal of Materials Research and the other part has been submitted to Journal of Mechanics and Physics of Solids)

8.1 Introduction

As reviewed in chapter 2, the origin of the size effect can be generally divided into microstructural (intrinsic) and dimensional (extrinsic) lengths. Microstructural size effects include those due to grain boundaries (Hall, 1951; Petch, 1953) and particle reinforcement (Lloyd, 1994). Effects of dimensional size have been presented for compression of pillars (Greer *et al.*, 2004; Volkert and Lilleodden, 2006), torsion of wires (Fleck *et al.*, 1994), bending of foils (Stölken and Evans, 1998; Ehrler *et al.*, 2008), indentation (Ma and Clark, 1995; Nix and Gao, 1998; Lim and Chaudhri, 1999; Swadener *et al.*, 2002; Zhu *et al.*, 2008a; b) and other geometries (Nix, 1989; Espinosa *et al.*, 2004).

In a remarkable number of instances, material strength scales with the inverse square-root of the smallest length scale. The bending results reported in chapter 3 and 5 show that the stress in bending is proportional to the inverse square-root of the effective length scale $1/l_{eff}^{1/2}$ at small strain region; the indentation size effect reported in chapter 7 shows that the indentation mean pressure (or hardness) is proportional to the inverse square-root of the contact size, $1/a^{1/2}$ for both pointed and spherical indentation; classic Hall-Petch effect shows the yield stress or flow stress is

proportional to the inverse square-root of grain size, $1/d^{1/2}$; and the recent data (Volkert and Lilleodden, 2006; Greer *et al.*, 2005) shows that the yield strength of pillar under uniaxial compression is proportional to the inverse square-root of the pillar diameter, $1/D^{1/2}$, herein designated as $1/\sqrt{l}$ scaling.

In the majority of these size dependent cases, strain gradients are involved, and there is a general agreement that the size effect can then be attributed to hardening due to geometrically-necessary dislocations (GNDs) (Nye, 1953; Ashby, 1970; Nix and Gao, 1998). A characteristic length l^* is often introduced to parameterise the theory. However, in other cases, strain gradients are not involved; for instance, micro-pillar compression has uniform deformation without strain gradients, but also appears to closely follow $1/\sqrt{l}$ scaling (Volkert and Lilleodden, 2006). General models capable of predicting $1/\sqrt{l}$ for such a diverse range of tests and microstructures have yet to emerge and it is not apparent why such an exact relationship should hold. Moreover, strain gradient plasticity theories (Fleck *et al.*, 1994; Gao *et al.*, 2000; Swadener *et al.*, 2002; Han *et al.*, 2005) can predict $1/\sqrt{l}$ scaling for some situations but the physical interpretation of the characteristic length l^* in these theories is not always clear.

Furthermore, polycrystalline nickel bending data presented in chapter 3 and polycrystalline copper spherical indentation data obtained by Hou *et al.* (2008) show that the interaction between dimensional (thickness in bending and contact size in indentation) and grain size effects. An understanding of the combination of size effects is essentially necessary for applied mechanics and engineering. Existing

theories for combining microstructure and extrinsic size effects are rarely found in the literature (as reviewed in chapter 2).

No existing theory predicts $1/\sqrt{l}$ behaviour both for the situations where l is the order of the grain size, d, and where l is the order of the structure size, h. Still less are there any theoretical approaches which address the situation where l is the order of both d and h. Our approach is to reconsider the classic theory of Conrad *et al.* (1967) in which the key factor is the distance that a dislocation can move. This theory readily captures the size effect with and without strain gradient, and in any case without requiring the characteristic length l^* (Nix and Gao, 1998, Fleck and Hutchinson, 1993, Qin *et al.*, 2007) used in strain gradient plasticity theory. Then, in a new analysis of the interactions of grain size and structure size, the effective length scale at when d is the order of structure is considered, thus the length scale parameter l_{eff} is defined including both extrinsic and intrinsic length scale. This approach gives a model which yields in excellent agreement with experimental data.

Finally, in chapter 7, Fig. 7.6 shows that the normalised yield pressure for metals and ceramics fell on quite different slopes when plotted against $a^{-1/2}$, that is, the magnitude of the size effect appeared to be greater in metals than ceramics. This result implies that material parameters must be important in length scale plasticity. It is not clear which material parameter could account for the difference in the size effect between metals and ceramics (as discussed in section 7.4.1). Current theories do not appear to have identified the material property basis that can explain these observations.

In this chapter, two possible equivalent derivations of a mechanical model are presented that can give the general $1/\sqrt{l}$ behaviour with and without strain gradient, and in any case without the extra characteristic length l^* used in the strain gradient plasticity theory. This 'slip distance' theory based on Conrad *et al.* (1967) was extended to explain the polycrystalline materials size effect by defining an effective length scale l_{eff}, including all extrinsic and intrinsic effects. This slip-distance theory also naturally incorporates the material parameters that influence the size effect. This model suggests that the yield strain and Burger's vector are the important material parameters in the size effect. The theory is in good agreement with experimental observations.

This slip-distance model was inspired by Prof. Evans, during his visit in Queen Mary last Autumn.

8.2 Slip-distance models for size effects

First of all, two analyses are introduced which essentially attribute the $1/\sqrt{l}$ behaviour to the Taylor hardening (Taylor, 1934) under fairly standard assumptions but without requiring a strain gradient.

8.2.1 Mechanical analysis of slip distance

Under homogeneous loading, mobile dislocations are considered to account for the plastic strain. Each of them is supposed to travel a mean free path, an average distance $\bar{x}$, limited by obstacles such as grain boundaries, or indeed by encountering a free surface. The plastic strain is:

$$\varepsilon_{pl} = \rho_m b \bar{x} \tag{8.1}$$

where ρ_m is the mobile dislocation density and b is the effective Burger's vector. We take the mean free path $\bar{x}$ to be proportional to the characteristic length scale l such as the distance to a grain boundary or a free surface,

$$\bar{x} = l / \lambda \tag{8.2}$$

where λ is a proportionality coefficient of the order of unity. Let the mobile dislocation density be proportional to the total dislocation density,

$$\rho_m = \xi \rho \tag{8.3}$$

where ξ is a proportionality coefficient and with $0 < \xi < 1$. Then the plastic strain is:

$$\varepsilon_{pl} = (\xi / \lambda) \rho b l \tag{8.4}$$

Assuming that hardening is due only to dislocation-dislocation interactions; equivalently, the dominant change during plastic flow is dislocation density. This is essentially the Taylor's model of forest hardening (Taylor, 1934), and so following his expression:

$$\tau = \tau_0 + \alpha \mu b \sqrt{\rho} \tag{8.5}$$

where μ is the shear modulus, τ is the shear stress, τ_0 is the initial yield stress in shear for a single crystal and α is a material coefficient of the order of unity (Gao, 1999; Huang, 2004). Substituting from Eqs. (8.1) – (8.4), Eq. (8.5) becomes

$$\tau = \tau_0 + \alpha \left(\frac{\lambda}{\xi} \right)^{1/2} \mu \sqrt{b} \frac{\sqrt{\varepsilon_{pl}}}{\sqrt{l}} \tag{8.6}$$

Note that $1/\sqrt{l}$ strengthening is predicted, and it is also linked directly with square-root power-law work-hardening.

8.2.2 Model for slip distance analysis

The analyses of section 8.2.1 result that:

$$\tau = \tau_0 + C\mu\sqrt{b}\frac{\sqrt{\varepsilon_{pl}}}{\sqrt{l}} \tag{8.7}$$

where C is the coefficient $C = \alpha(\lambda/\xi)^{1/2}$ of the order of unity.

The derivation is suspected to be equivalent, as the fundamental basis for the analyses is the assumption that dislocations are the primary source of obstruction to dislocation movement (Taylor work hardening). The inverse square-root length scaling $1/\sqrt{l}$ arose in both methods and linked directly with the square-root work hardening. The size effect arises independently of strain gradient. The density of geometrically necessary dislocations is anyway proportional to the plastic strain and so is subsumed into the coefficient ξ of Eqs. (8.3) and (8.4). This coefficient thus subsumes the characteristic length l^* used in the strain gradient plasticity theory.

The tensile flow stress is related to the shear flow stress by,

$$\sigma = A\tau \tag{8.8}$$

where A is the Taylor factor, of the order of unity, which may be interpreted as an isotropic expression of the crystalline anisotropy at the continuum level. A value of A = 3.06 is given for fcc metals (Bishop and Hill, 1951; Kocks, 1970; Huang *et al.*, 2004). Then,

$$\sigma = \sigma_0 + AC\mu\sqrt{b}\frac{\sqrt{\varepsilon_{pl}}}{\sqrt{l}} \tag{8.9}$$

8.3 Characteristic length for polycrystalline materials

In single crystal structures, the length l which determines the effective slip distance $\bar{x}$, is relatively easy to identify. For instance, in pillar compression, it is the diameter D of the pillar; in bending, it is the thickness h of the foil; in twisting, it is the diameter of the wires and for nanoindentation, we expect it to be the contact radius a of the indent. However, it will be more complicated in polycrystalline materials, because of the influence of the grain size, d.

The extrinsic size effect and the intrinsic size effect due to grain size are expected to interact when they are both of significant scale. The mean slip distance should be determined by an effective length l_{eff} determined both by grain size and by dimensional (extrinsic) constraints. In what follows, the grain structure is supposed to be independent of the dimensional constraint – as if, say, a foil was cut out of a bulk material after the grain structure was formed.

Consider a one-dimensional external size constraint, for instance, a foil undergoing bending, with thickness h and grain size d, as shown in Figs. 8.1 and 8.2. A dislocation may ideally be taken to pass along the h direction, as indicated in the figure by the broken arrow, although, in reality, its slip plane in different grains would be at various angles to the h direction.

Noted that in the limiting case with $d > h$, the dislocation slip distance $\bar{x}$ is only influenced and scaled by h, because the dislocation will not generally encounter grain boundaries but can only experience the boundaries delimiting h (the free surfaces). On the other hand, in the other limit, $d < h$, $\bar{x}$ can be simply taken as

scaled by d, because a moving dislocation generally encounters grain boundaries before it encounters the foil surface.

Fig. 8.1 is drawn to illustrate the case where d and h are comparable but $d < h$. If the grain structure is independent of the presence of free surfaces, then we have part-grains at both surfaces of foil (here drawn as half-grains). A path length h traversing N grains would imply a value for l_{eff} of

$$l_{eff} = \frac{h}{N} \tag{8.10}$$

However, the number of internal whole grains may be counted as $\frac{h}{d} - 1$. Counting the two surface part-grains as grains, we add 2, giving

$$N = \frac{h}{d} + 1 \tag{8.11}$$

Substituting Eq. (8.11) into Eq. (8.10),

$$l_{eff} = \frac{h}{N} = \frac{h}{\frac{h}{d} + 1} = \frac{1}{\frac{1}{h} + \frac{1}{d}} \tag{8.12}$$

which can also be written as

$$\frac{1}{l_{eff}} = \frac{1}{d} + \frac{1}{h} \tag{8.13}$$

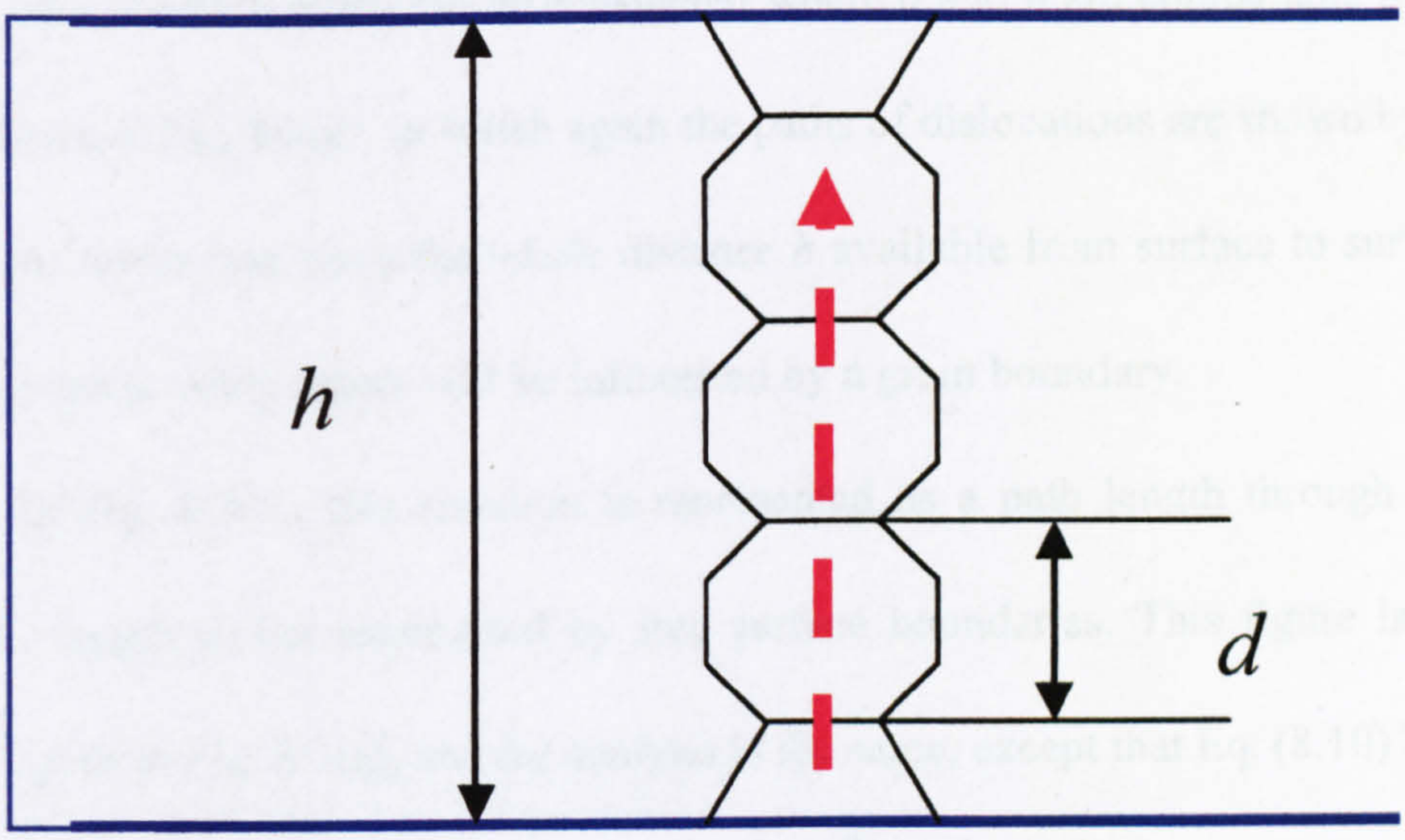

(a)

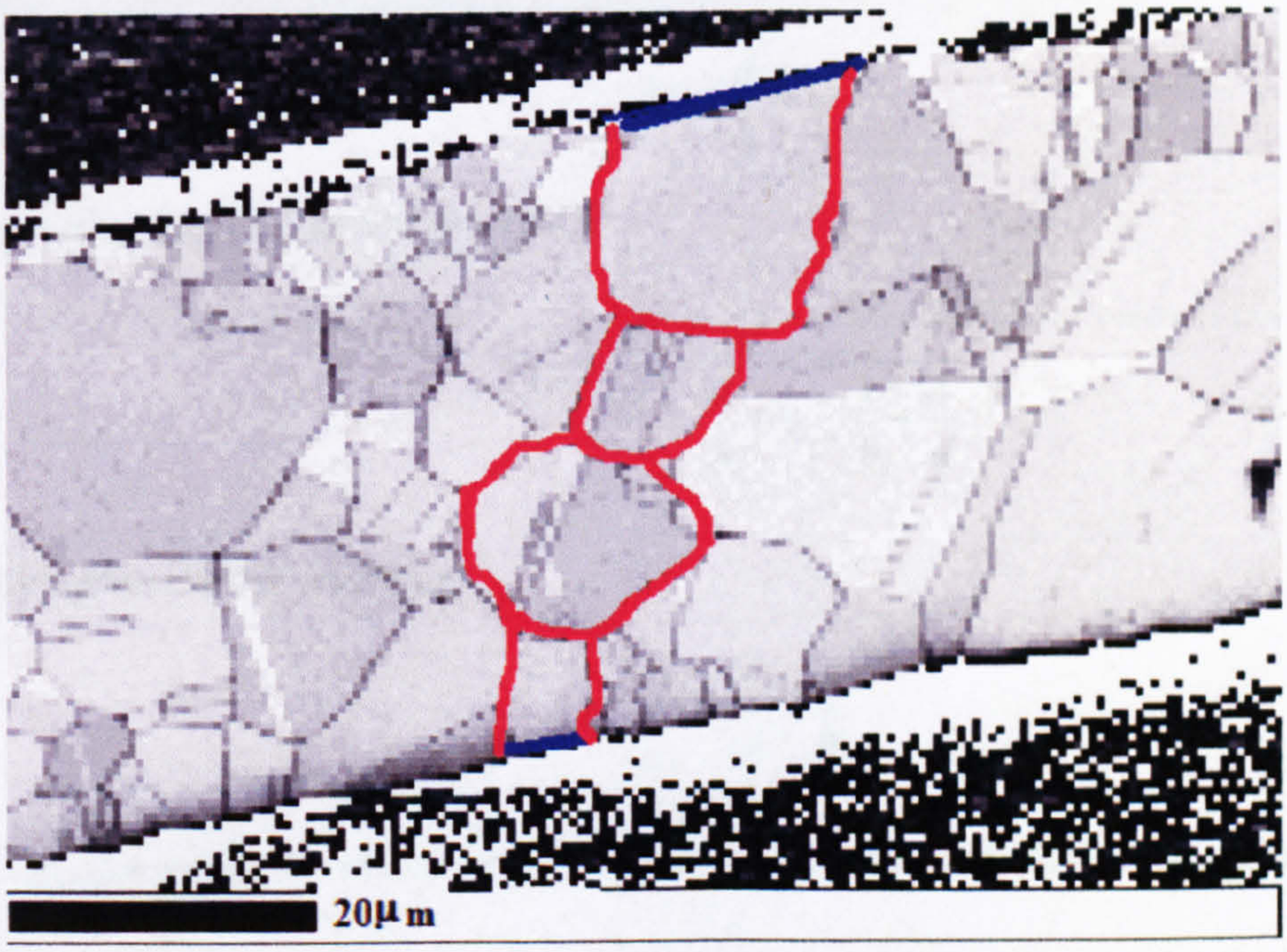

(b)

Figure 8.1 (a) Schematic diagram of a foil cross section of thickness of h with grain size d. The broken arrow shows a path available to a dislocation along the thickness direction. (b) Electron backscattering diffraction (EBSD) orientation map of the cross-section of a 50μm nickel foil with the average grain size d = 14μm. Some grain boundaries are highlighted to show a structure resembling the schematic of (a).

The situation must also be considered where d and h are comparable but $d > h$, as shown in Fig. 8.3(a), in which again the paths of dislocations are shown by broken arrows. Some may have the whole distance h available from surface to surface in a single grain, while others will be influenced by a grain boundary.

In Fig. 8.3(b), this situation is represented as a path length through a whole grain, length d, but interrupted by free surface boundaries. This figure is directly analogous to Fig. 8.2(a), and the analysis is the same, except that Eq. (8.10) becomes

$$l_{eff} = \frac{d}{N} \tag{8.14}$$

Now:

$$N = \frac{d}{h} + 1 \tag{8.15}$$

Substituting Eq. (8.15) into Eq. (8.14),

$$l_{eff} = \frac{d}{N} = \frac{d}{\frac{d}{h}+1} = \frac{1}{\frac{1}{h}+\frac{1}{d}} \tag{8.16}$$

which again can be written as

$$\frac{1}{l_{eff}} = \frac{1}{d} + \frac{1}{h} \tag{8.17}$$

So the same expressions are obtained, Eqs. (8.13) and (8.17), for l_{eff} in the cases $d < h$ and $d > h$. This expression also has the correct behaviour in the limits $d >> h$ and $d << h$. Note, however, that it is obtained assuming that the dislocations slip in the direction of h. Other directions have greater lengths (with a $1/\cos\theta$ term), and so in fits to experimental data we may expect a non-unity coefficient on h^{-1}.

Experimental measurements may check this model. As an example, a cross-section electron backscatter diffraction (EBSD) image (EBSD, HKL5, Oxford

Instruments, UK) of a nickel foil is shown in Fig. 8.1(b) The sample possess 50μm thickness and with grain size around 14μm, i.e. $d < h$. In Fig. 8.1(b), the grain boundaries are highlighted to illustrate a structure resembling the schematic of Fig. 8.1(a). Fig. 8.2(c) shows an optical microscopic cross section picture of another nickel foil, with 125μm thickness and with grain size around 200μm, i.e. $d > h$. Some grains extend from one free surface to the other, while elsewhere grain boundaries appear within the thickness, as in the schematic diagram of Fig. 8.2(a).

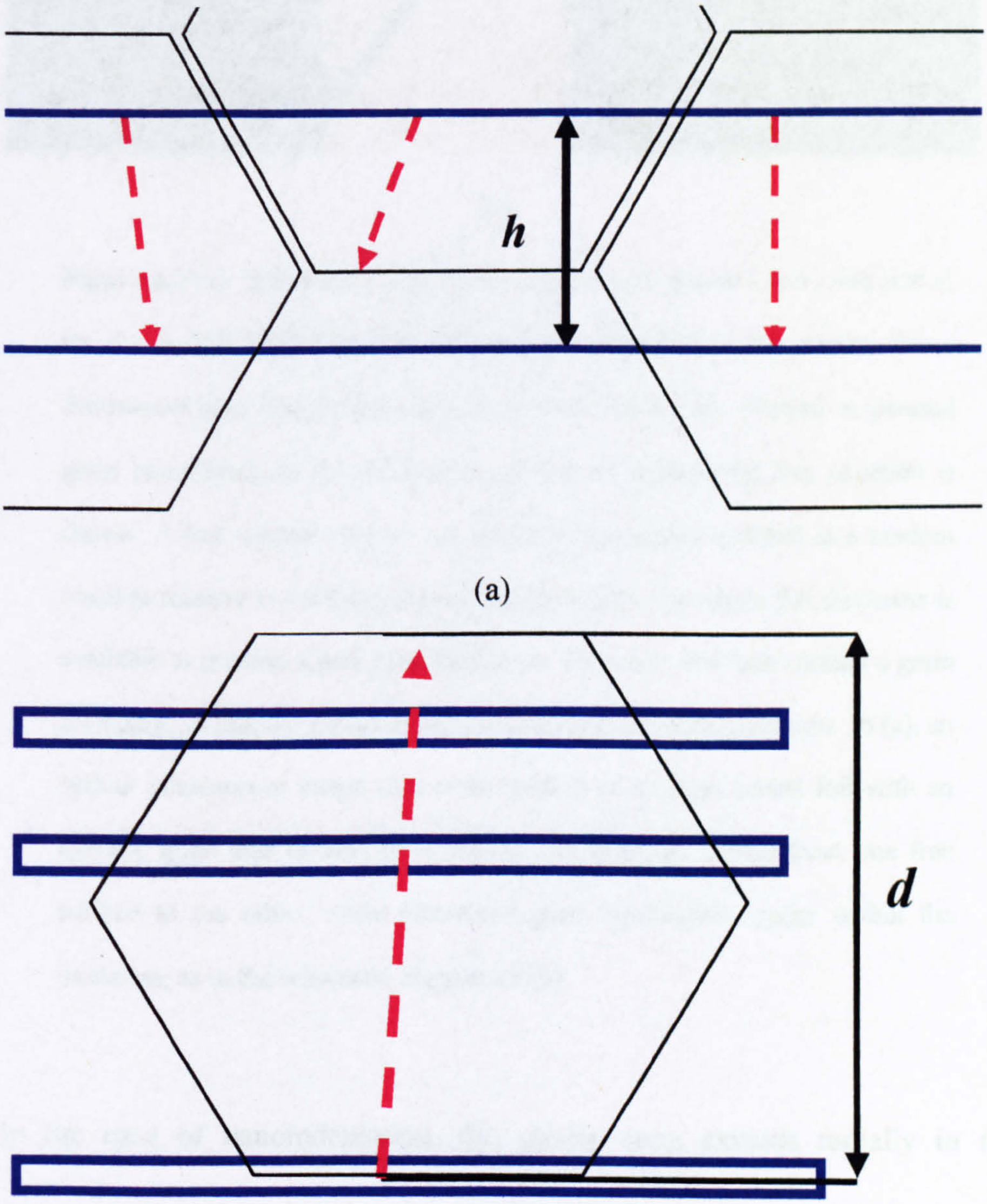

(a)

(b)

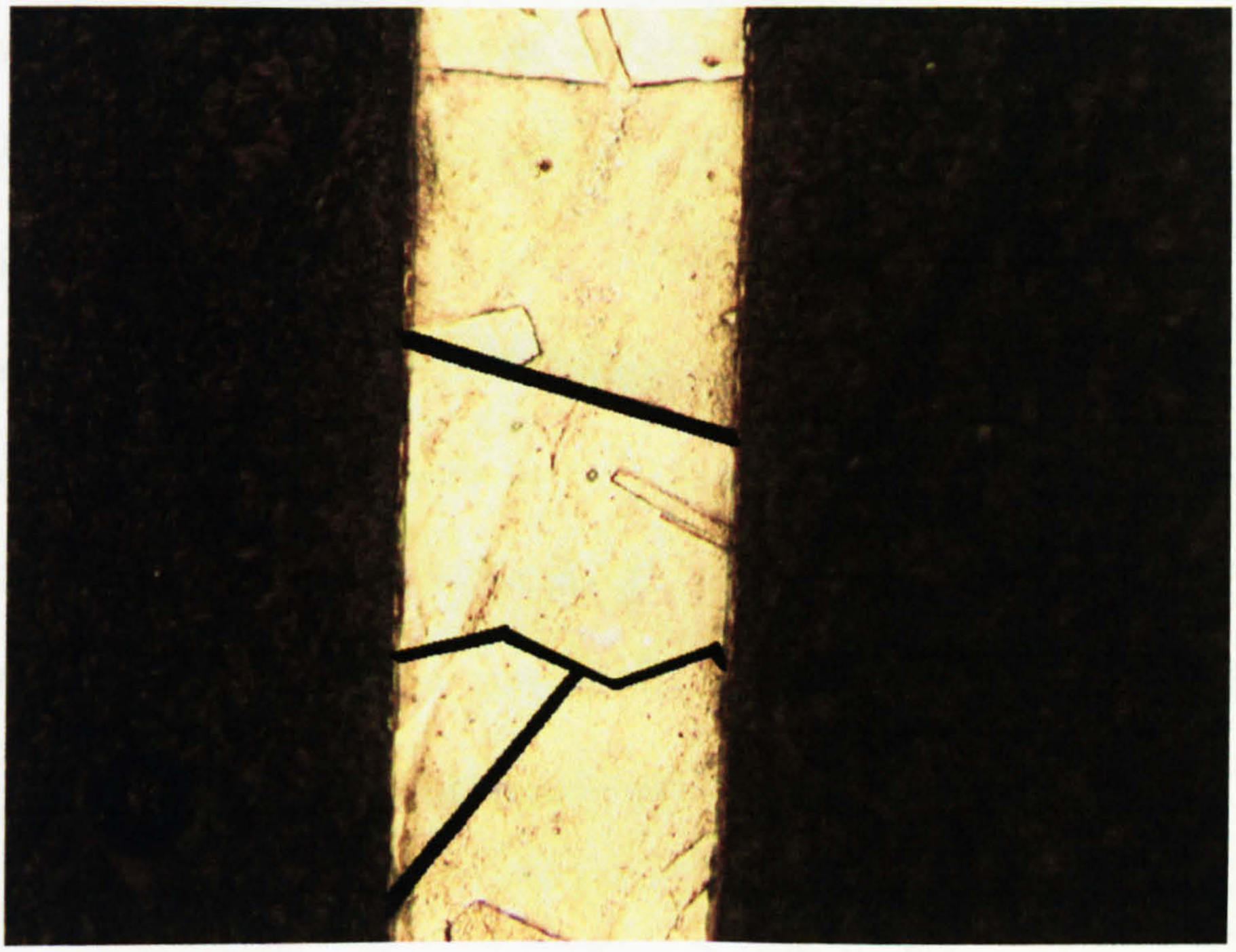

(c)

Figure 8.2 (a): Schematic diagram of a foil with thickness h and grain size d, for $d > h$. The broken arrows indicate paths available to dislocations. Some dislocation path lengths are equal to h, while others are stopped at internal grain boundaries. In (b), an alternative way of considering this situation is shown. A foil section may be cut out of a large-grain material at a random position relative to the grain shown. In most cases, the whole foil thickness is available to provide a path to a dislocation. However, h/d foils contain a grain boundary, so that the available path is only part of the foil thickness. In (c), an optical microscopic image of a cross section of a125μm nickel foil with an average grain size of 200μm is shown. Some grains extend from one free surface to the other, while elsewhere grain boundaries appear within the thickness, as in the schematic diagram of (a).

In the case of nanoindentation, the plastic zone extends radially in three dimensions. Under an axi-symmetric indenter (conical, spherical, and including as an

approximation Berkovich and cube corner indenters), the contact radius is a. Following Johnson (1987), the effective deformation zone is considered as a hemisphere with radius a and volume $V = \frac{2}{3}\pi a^3$, shown schematically in Fig. 8.3. A three-dimensional analogue of the foregoing argument would consider the number of part-grains (grains intersecting the hemispherical surface), which is of order $2\pi a^2 / d^2$, and conclude that the number of grains participating in the deformation is therefore not V / d^3 but $V / d^3 + 2\pi a^2 / d^2$. (See the schematic diagram shown in Fig. 8.3). As above, an effective length, l_{eff}, can then be derived.

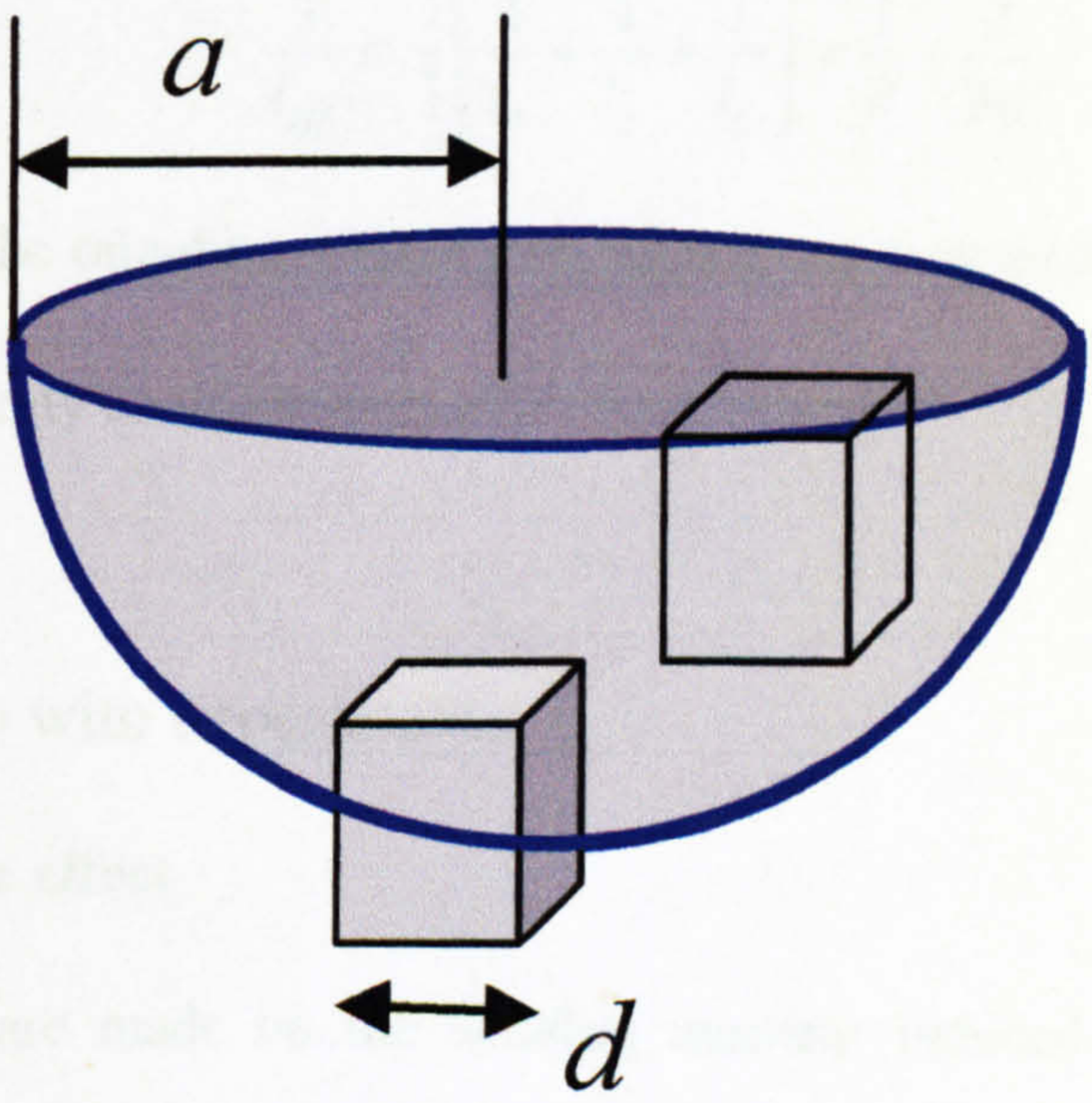

Figure 8.3 Schematic of the plastic deformation zone beneath a spherical indentation with contact radius a. The plastic zone is approximated to a hemisphere of radius a, after Johnson (1987). Grains in the metal are considered as cubic in shape with side length d, some of which may be wholly within the plastic zone and others partial within.

More simply, we note that what matters are only the slip planes and the distances dislocations can move along them. Thus the one-dimensional analysis above should remain applicable. However, the volume is not a sphere and has a different size in z (a) and in x and y ($2a$). So different effective lengths will be expected in these directions,

$$\frac{1}{l_x} = \frac{1}{l_y} = \frac{1}{d} + \frac{1}{2a} \tag{8.18}$$

$$\frac{1}{l_z} = \frac{1}{d} + \frac{1}{a} \tag{8.19}$$

Some suitable average should be taken, e.g.,

$$\frac{1}{l_{eff}} = \frac{1}{3}\left(\frac{1}{l_x} + \frac{1}{l_y} + \frac{1}{l_z}\right) = \frac{1}{d} + \frac{2}{3a} \tag{8.20}$$

Thus, as in the one-dimensional case above, we may expect fits to experiment to require a non-unity coefficient on a^{-1}.

8.4 Comparison with experiments

8.4.1 Bending size effect

The studies are made on the bending moment induced in nickel foils as a function of curvature. The full data-set and details of the experimental methods were described in chapters 3-5. Three foils with different thickness of 10μm, 50μm and 125μm were tested, with grain sizes ranging from 6μm to 200μm. Ratios of d / h range from 3 to 0.03, thus providing a stringent test of expressions in $d^{-1} + h^{-1}$.

Fig. 8.4 shows the experimental data for normalised nickel bending moment M_n at $\varepsilon_s = 0.1\%$ (These data is taken from chapter 3 of nickel bending). To calculate the

theoretical normalised bending moment, we apply the slip distance expression Eq.(8.9) for the stress $\sigma(z)$, and for the effective length scale l_{eff} in polycrystalline bending we use Eq. (8.17), where h is taken to be the foil thickness. Then,

$$\sigma = \sigma_0 + AC\mu\sqrt{b}\sqrt{\frac{1}{d}+\frac{1}{h}}\sqrt{\varepsilon_{pl}} \tag{8.21}$$

Approximating that $\sigma_0 \approx 0$, so throughout the foil, $\varepsilon_{pl} = z\kappa$. Then,

$$\sigma(z) = AC\mu\sqrt{b}\sqrt{\frac{1}{d}+\frac{1}{h}}\sqrt{z\kappa} \tag{8.22}$$

In order to compare the theory with obtained experimental results, the normalised bending moment M_n is evaluated as:

$$M_n = \frac{2\int_0^{\frac{h}{2}}\sigma(z)zdz}{wh^2} = \frac{1}{5}AC\mu\sqrt{b}\sqrt{\frac{1}{d}+\frac{1}{h}}\sqrt{\varepsilon_s} \tag{8.23}$$

The theoretical fit is obtained from Eq. (8.23), with parameter values of ε_s = 0.1%, A = 3.06 (for fcc metals (Kocks, 1970; Huang *et al.*, 2004)), $\sigma_0 \approx 0$, μ = 78GPa and b = 0.245nm and with C as the only fitting variable. A best fit is obtained by applying $C = 2.8 \pm 0.05$. The result is plotted as the dotted line on Fig. 8.4. It can be seen that the fitted strength with foil thickness and grain size is highly consistent with the measurements.

Now, consider whether the value of C is reasonable, where it need to be applied again that C is a function of λ, ξ and α, as $C = \alpha(\lambda / \xi)^{1/2}$. λ and ξ can be estimated. For foil bending, since dislocations would not traverse the neutral plane, the mean free path of the dislocations is smaller than half of the characteristic length. We apply here: $\lambda = 3$. The fraction of mobile dislocation density could be taken as $\xi \approx 0.3$ from Hackelöer *et al.* (1977). In this case, $C = 2.8$ gives $\alpha = 0.88$. The value of α cited in

the literature is between 0.2 - 1.2 (Gao *et al.*, 1999; Huang *et al.*, 2004). So the value for C is reasonable.

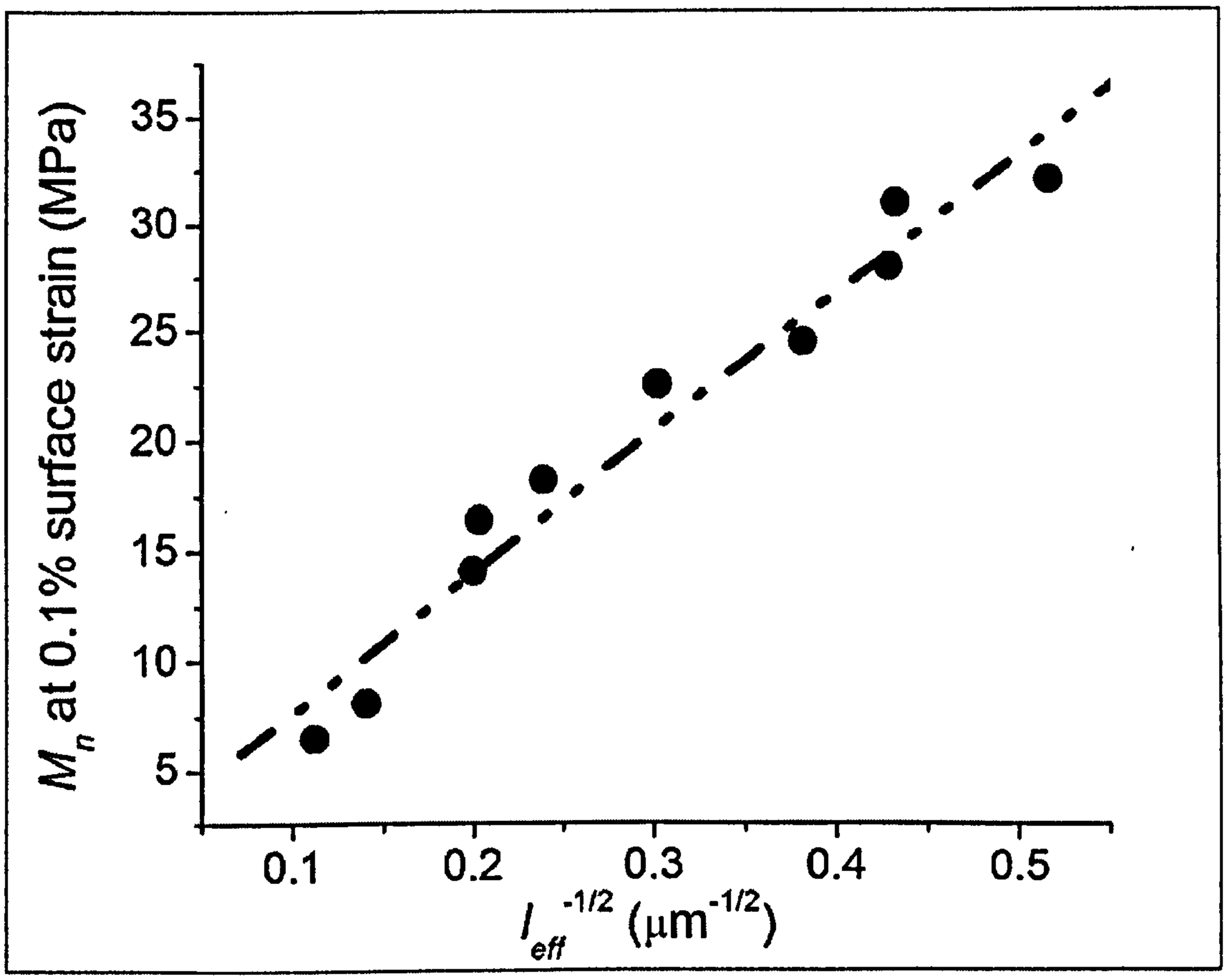

Figure 8.4 Nickel foil bending data (chapter 3, for all different thickness and grain size foils) as normalised bending moment M_n at 0.1% surface strain versus $l_{eff}^{-1/2}$ (where $\frac{1}{l_{eff}} = \frac{1}{d} + \frac{1}{h}$). The dotted line is the theoretical prediction using Eq. (8.23), with the best fit value of the free parameter, C = 2.8 ± 0.05 ($R^2 = 0.951$).

8.4.2 Indentation size effect for polycrystalline materials

Recently, Hou *et al.* (2008) performed spherical nanoindentation on single crystal and polycrystalline copper. They used different radius indenters on samples with a range of grain sizes. Their data shows interaction between the grain size effect and the indentation size effect. Three indenters were used with the contact radii a ranging from 0.82μm to 50μm. The grain sizes varied from 1.15μm to infinite large (single crystal), giving ratios of d / a in the range from infinite to 0.3. This data set is therefore able to provide a stringent test of slip distance theory and of size effects that use expressions in $d^{-1} + a^{-1}$. The results for indentation mean pressure measured at an indentation strain of 0.25 are replotted from Hou *et al.* (2008) in Fig.8.5.

In order to compare these results with the theory, the indentation mean pressure P_m is evaluated as (Tabor, 1951),

$$P_m = 2.8\sigma \tag{8.24}$$

To calculate the theoretical indentation mean pressure, we use again the slip distance theory expression Eq. (8.9) for stress σ, and for the effective length scale l_{eff} in polycrystalline indentation we use Eq. (8.20). Then,

$$\sigma = \sigma_0 + AC\mu\sqrt{b}\sqrt{\frac{1}{d}+\frac{2}{3a}}\sqrt{\varepsilon_{pl}} \tag{8.25}$$

Again, σ_0 is approximated as 0. Under these assumptions, it is possible to evaluate the plastic strain in indentation (Huang *et al.*, 2004) as

$$\varepsilon_{pl} = 0.2\varepsilon_{ind} = 0.2\frac{a}{R} \tag{8.26}$$

where ε_{ind} is the indentation strain, conventionally defined as a/R for spherical indentation (Fisher-Cripps, 2000; 2001; Bushby, 2001). The theoretical prediction of P_m is therefore,

$$P_m = 2.8\left(AC\mu\sqrt{b}\sqrt{\frac{1}{d}+\frac{2}{3a}}\sqrt{0.2\varepsilon_{ind}}\right) \tag{8.27}$$

Using Eq. (8.27), with parameter values of $\varepsilon_{ind} = 0.25$, $A = 3.06$ (for fcc metals (Kocks, 1970; Huang *et al.*, 2004)), $\sigma_0 \approx 0$, $\mu = 43.5$GPa, $b = 0.256$nm, C is the only free fitting parameter. A best fit is obtained by using $C = 0.84 \pm 0.02$, plotted as the dotted line in Fig. 8.5. The predicted variation of strength with contact radius and grain size is consistent with the measurements.

Now, the reasonability of the value of C is considered. $C = \alpha(\lambda / \xi)^{1/2}$ is recalled. In indentation, a dislocation is supposed to move across the plastic zone. Since the indentation contact size a is the characteristic length here while the plastic zone radius is about $3a$ (Johnson, 1987), a dislocation is supposed to travel farther than the characteristic length. It is reasonable to take $\lambda \approx 1/3$. As for ξ, from Hackelöer *et al.* (1977), the fraction of mobile dislocations could be taken as $\xi \approx 0.3$. Then, $C = 0.84$ gives $\alpha = 0.80$. The values of α cited in the literature are between 0.2 and 1.2 (Gao *et al.*, 1999; Huang *et al.*, 2004). So the value of $C = 0.84$ is not unreasonable.

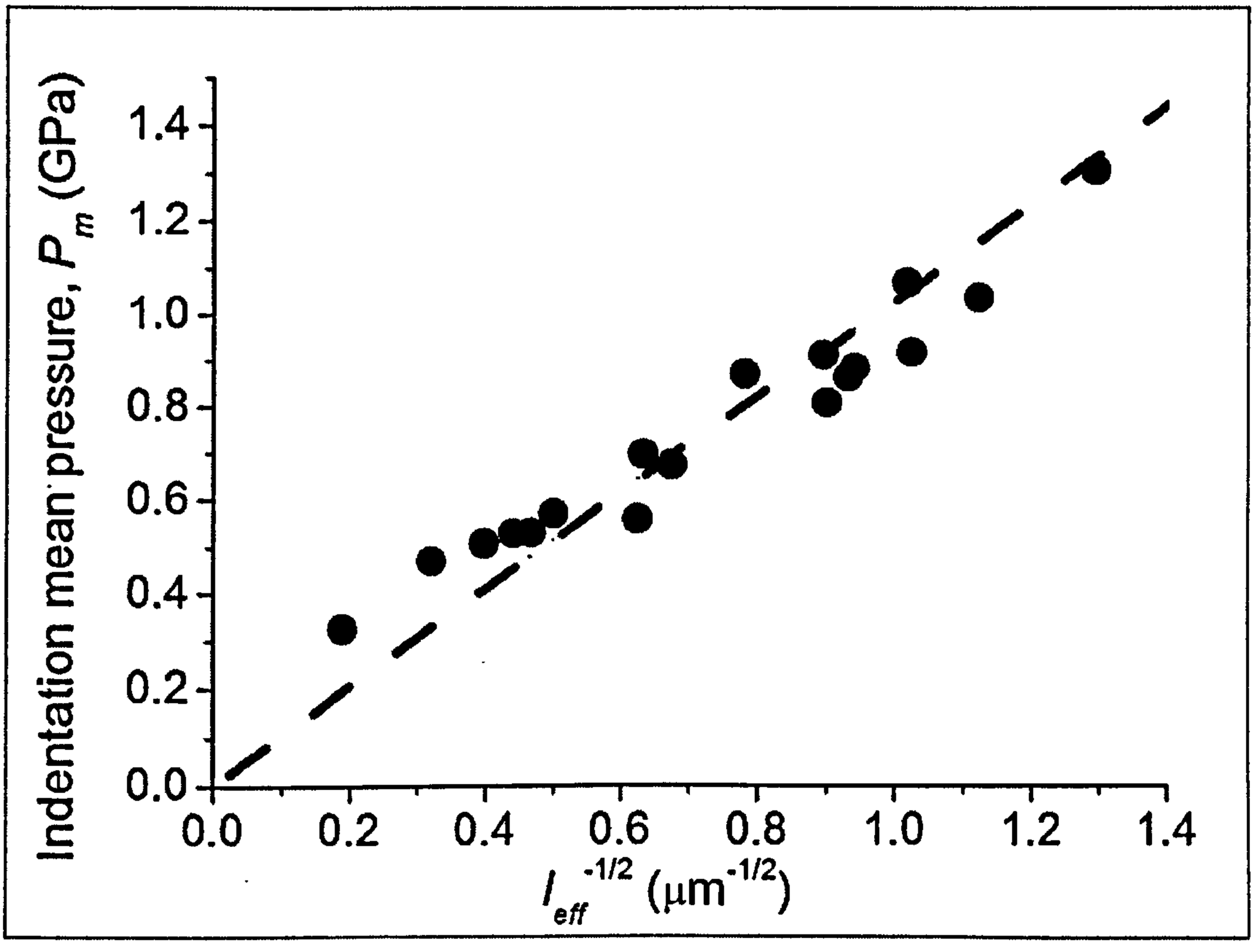

Figure 8.5 Polycrystalline copper indentation experimental data replotted from Hou *et al.* (2008) as P_m (at 0.25 indentation strain) against $l_{eff}^{-1/2}$ (where $\frac{1}{l_{eff}} = \frac{1}{d} + \frac{2}{3a}$). The dotted line is the theoretical prediction using Eq. (8.27), with the best fit value of the free parameter, $C = 0.84 \pm 0.02$ ($R^2 = 0.803$).

Remarkably, the wedge indentation size effect via two-dimensional discrete dislocation plasticity carried out by Widjaja *et al.* (2007) recently agrees with this theory as well. The data are shown in chapter 2 as Fig. 2.9. In these data, due to the finite size of the block in their simulation, the elastic hardness is h-dependent (Widjaja *et al.*, 2007). So, in Fig. 8.6, the plotted hardness is normalised by the elastic hardness (illustrated in Fig. 2.9, (Widjaja *et al.*, 2007)).

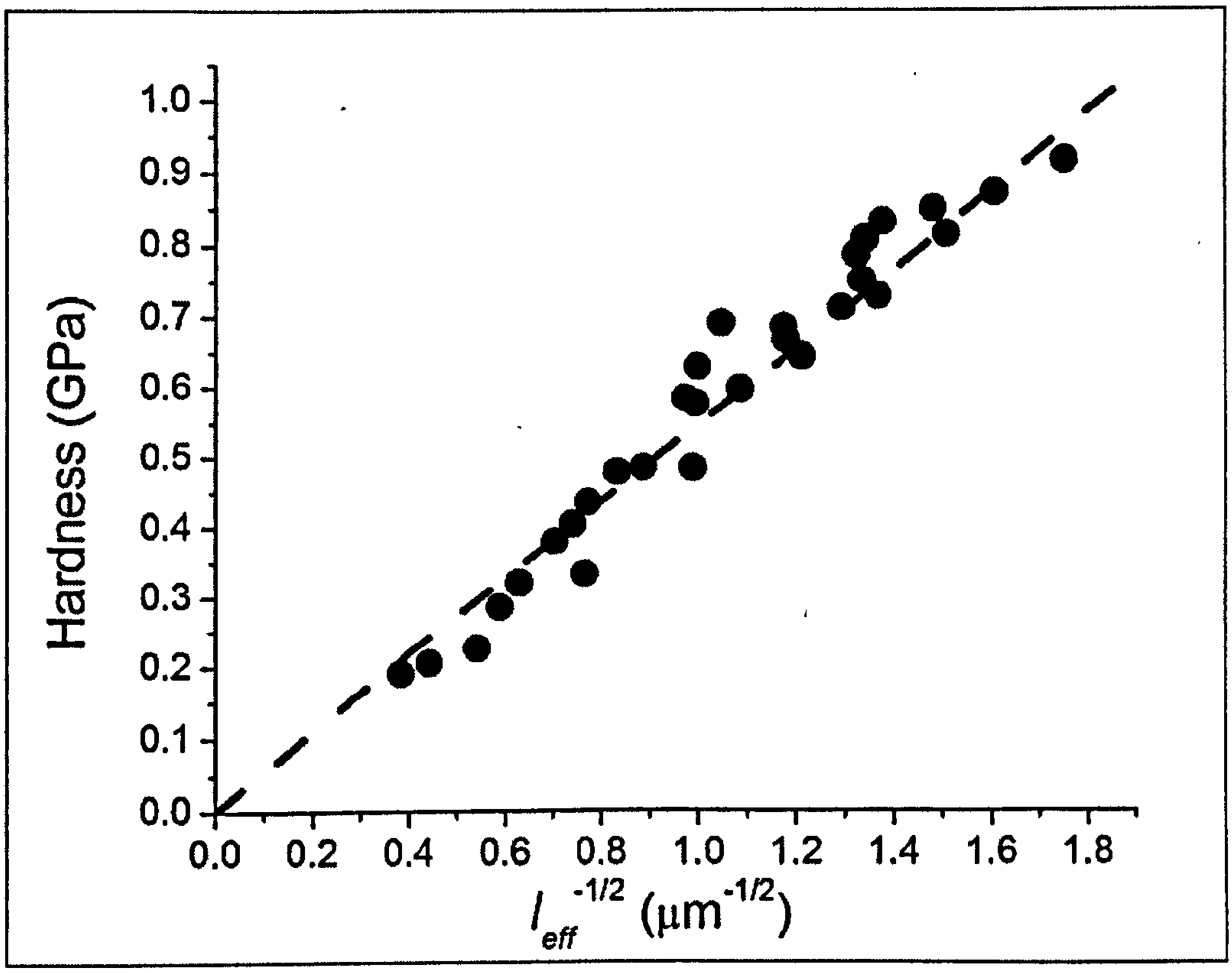

Figure 8.6 Wedge indentation simulation data replotted from Widjaja *et al.* (2007) as normalised hardness against $l_{eff}^{-1/2}$ (where $\frac{1}{l_{eff}} = \frac{1}{d} + \frac{2}{3a}$). The dotted line is the theoretical prediction using Eq. (8.27) with the best fit value of the free parameter $C = 1.01 \pm 0.02$, ($R^2 = 0.957$).

The theoretical pressure is obtained by using Eq. (8.27), with parameter values of $\varepsilon_{ind} = 0.01$, $A = 3.06$ (for fcc metals (Kocks, 1970; Huang *et al.*, 2004)), $\sigma_0 \approx 0$, $\mu =$ 26.3GPa, $b = 0.286$nm, C is the only free fitting parameter. A best fit is obtained by using $C = 1.01 \pm 0.02$, plotted as the dotted line in Fig. 8.6. The predicted variation of strength with contact radius and grain size is very consistent with the measurements. With inputting the same parameter λ and ξ as for polycrystalline copper indentation ($\lambda = 1/3$ and $\xi \approx 0.3$), then $C = 1.01$ gives $\alpha = 0.95$. The values of

α cited in the literature are between 0.2 and 1.2 (Gao *et al.*, 1999; Huang *et al.*, 2004). So the value of $C = 1.01$ is not unreasonable.

8.4.3 Indentation yield size effect - material parameters study

In chapter 7, it is showed that the normalised gross yield pressure scales with the inverse square-root of contact size a for all materials investigated. However, the normalised data for metals and ceramics fell on quite different slopes in spite of similar ranges of elastic modulus in both sets of materials (Fig. 7.6). Here, the aim is to investigate which material parameters are accounting for the different magnitude of size effect in metals and ceramics.

To calculate the theoretical indentation mean pressure at gross yield, the slip-distance theory is used again: expression Eq. (8.9) for stress, σ, and the contact size a for the effective length scale l_{eff}. Taking the apparent plastic strain at yield, ε_y^{pl}, (calculated as σ_0 divided by the Young's modulus) to be a small value equivalent to the elastic strain at the onset of yield, gives the measured yield strength scaling:

$$\sigma_y = \sigma_0 + AC\mu\sqrt{b}\frac{\sqrt{\varepsilon_y^{pl}}}{\sqrt{a}} \tag{8.28}$$

To investigate the influence of material parameters that could result in different magnitude of size effect for ceramics and metals, Eq. (8.28) at the yield point was considered:

$$\frac{\sigma_y - \sigma_0}{\sigma_0} = \frac{AC\mu\sqrt{b}\sqrt{\varepsilon_y^{pl}}}{\sigma_0\sqrt{a}} \tag{8.29}$$

If

$$\sigma_0 = A\tau_0 = An\mu\varepsilon_y^{pl} \tag{8.30}$$

where n is a constant, and it is assumed as an order of unity here.

Hence (8.29) comes to:

$$\frac{\sigma_y - \sigma_0}{\sigma_0} = \frac{C\sqrt{b}}{\sqrt{\varepsilon_y^{pl}}}\left(\frac{1}{\sqrt{a}}\right) \tag{8.31}$$

Hence,

$$\frac{P_y - P_0}{P_0} = \frac{\sigma_y - \sigma_0}{\sigma_0} = \frac{C\sqrt{b}}{\sqrt{\varepsilon_y^{pl}}}\left(\frac{1}{\sqrt{a}}\right) \tag{8.32}$$

From Eq. (8.32), if it is normalised by these moduli, it becomes

$$\left(\frac{P_y - P_0}{P_0}\right)\frac{\sqrt{\varepsilon_y^{pl}}}{\sqrt{b}} = C\left(\frac{1}{\sqrt{a}}\right) \tag{8.33}$$

Normalising Fig. 7.6 (which plots $\frac{P_y - P_0}{P_0}$ against $a^{-1/2}$) further by a factor of $\sqrt{\varepsilon_y^{pl}}/\sqrt{b}$ gives the plot of Fig. 8.7 with all data falling close to a single line. The slope of the Fig. 8.7 should be C (as in Eq. (8.33)).

This would suggest that the different slopes in Fig.7.6 arise because material properties b and ε_y^{pl} are very different for ceramics and metals.

For clarifying all the parameters used in this theory, the properties for the investigated materials are listed in table. 8.1. (Some of the parameters have been presented in table 7.1 already).

Table 8.1 Properties of the materials studied

	Shear modulus μ **/ GPa**	**Burger's vector** b **/ nm**	**Macroscopic yield stress** σ_0 **/ GPa**	**Plastic strain at gross yield** ε_y^{pl}
α-Al_2O_3	150	0.475	4.6	0.011
InP	22.5	0.414	0.78	0.0086
$In_{0.53}Ga_{0.47}As$	36	0.413	1.3	0.014
GaSb	24	0.430	0.90	0.010
W	150	0.240	0.50	0.0011

In indentation, a dislocation is supposed to move across the plastic zone. Since the indentation contact size a is the characteristic length here while the plastic zone radius is about $3a$, a dislocation is supposed to travel farther than the characteristic length. It is reasonable to take $\lambda \approx 1/3$. As for ξ, from Hackelöer et al. (1977), the fraction of mobile dislocations could be taken as $\xi \approx 0.3$. This gives, C in the range of $0.9 < C < 1.02$ (appeared in Fig. 8.7), giving α in the range of $0.95 < \alpha < 1.07$. The values of α cited in the literature are between 0.2 and 1.2 (Gao *et al.*, 1999; Huang *et al.*, 2004). So the values of C are not unreasonable.

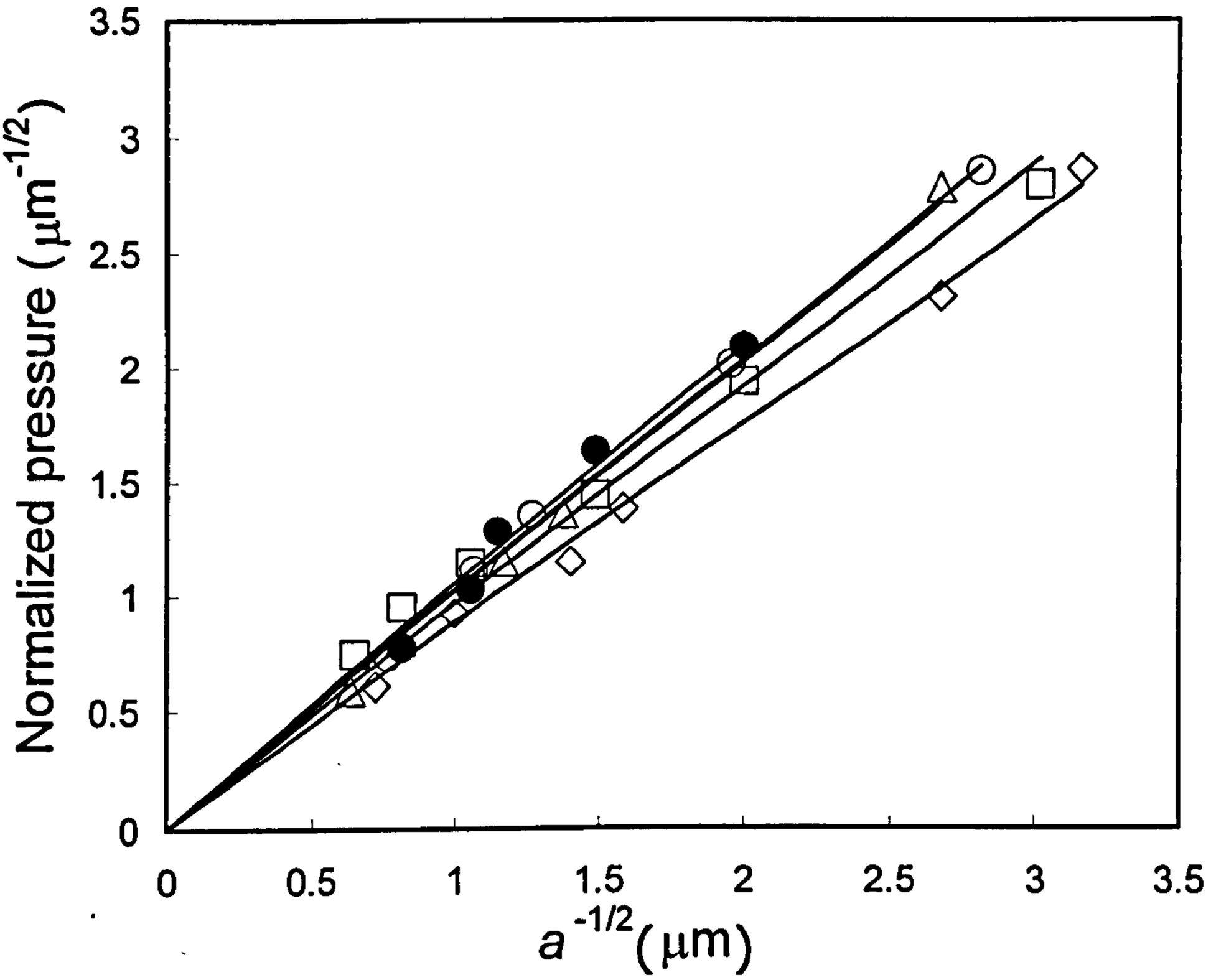

Figure 8.7 Normalised yield pressure $\left(\frac{P_y - P_0}{P_0}\right)\frac{\sqrt{\varepsilon_y^{pl}}}{\sqrt{b}}$ against $\frac{1}{\sqrt{a}}$, plotted for α-Al_2O_3 (○), InP (□), InGaAs (△) GaSb (◊) and W (●) as function of $a^{-1/2}$. The solid line is fitted by slip distance theory, equation (8.39) for each set of data using the material parameters listed in table 7.1.

8.5 Discussion

The mechanics model introduced here predict the inverse square-root size effect of plasticity in general deformation with or without a strain gradient and, in both cases, it is without an extra characteristic length parameter l^*.

The only free fitting parameter C in the theory is obtained from the best fit for experimental data. The value of C is found by this process to an accuracy of about ±2%. In the different loading geometries, by estimating the value of the coefficients

λ (the proportion of the dislocation mean free path to the characteristic size) and ξ (fraction of mobile dislocations), the coefficient α is obtained. The value of α is similar, all are close to 1.0. This is in good agreement with the cited values in the literature (Gao *et al.*, 1999; Huang *et al.*, 2004). The values obtained for C appear to be intuitive and could be predicted from sensible estimates of α, λ and ξ.

The ability of the approach presented here to combine different length scales, both intrinsic and extrinsic thus defining an effective length scale, is compelling. In the bending of thin foils the grain boundaries and free surfaces appear to have the same effect in limiting the slip distance and controlling the size effect. Similarly in the case of indentation the grain boundaries and extent of plastic zone also appear to present the same limitation of dislocation movement. These results imply that increased strength at small length scales can be achieved however the slip distance is delimited; by grain boundaries, free surfaces or strain gradients.

The material properties that influence the magnitude of size effects are also identified within this slip-distance model. The model suggests that the magnitude of the size effect is controlled by the yield strain and the Burger's vector for the material Eq. (8.33). In Fig. 8.7, in spite of the wide range of materials represented, the value of the constant C, that is the gradients of Fig. 8.7 for the different materials, are very similar, ranging from 0.9 to 1.02 and not in any systematic way by material class, shear modulus or yield strain. The resulted α is also close to 1.0, which is in good agreement with the literature (Gao *et al.*, 1999; Huang *et al.*, 2004). This implies Burger's vector and ε_y^{pl} must be the effective material parameters as predicted from

the slip–distance theory Eq. (8.33).

8.6 Conclusions

Comparison with experiments in a diverse range of loading geometries shows that the theory of 'slip distance' is consistent with the experimental observations showing $1/\sqrt{l}$ scaling.

Within the theory, different intrinsic and extrinsic length scales can be successfully combined to define an effective length scale for the material, l_{eff}.

The model also suggests that the magnitude of the size effect is controlled by the yield strain and the Burger's vector for the material, which agrees well with experimental observations.

9 Overall discussion

In order to clarify the whole story of this thesis, this chapter is placed.

From analysis of nickel bending data in chapter 5, the clear symmetry is shown between d and h in work hardening coefficient k in Fig.5.3 and flow strength in Fig.5.5, and the absence of any breakpoint in the data or the fits between $d < h$ and $d > h$, suggest that different ways of delimiting a finite volume or thickness have the same effect on the material strength, i.e., independent on the boundary conditions. In other words, the grain boundary and the free surface may have the same effect on strength of materials.

Furthermore, in chapter 7, the fact that the indentation mean pressure (or hardness) is proportional to the inverse square-root of the contact size, $1/a^{1/2}$, independent of the indenter shape, is intriguingly similar to the classic Hall-Petch effect in which the yield stress or flow stress of a metal is proportional to the inverse square-root of the grain size, $1/d^{1/2}$ (Hall, 1951; Petch, 1953), to recent data showing that the yield strength of pillars under uniaxial compression is proportional to the inverse square-root of the pillar radius, $1/D^{1/2}$ (Volkert and Lilleodden, 2006), to the bending data presented in chapter 3 showing bending stress at small strain is proportional to the inverse square-root of the effective length, $l_{eff}^{-1/2}$. These may further demonstrate that it is finite or restricted volumes that are responsible for the increased strength, rather than the boundary conditions at the edges of these volumes. In other words, the physics of the Hall-Petch effect, the uniaxial compression of pillars, and the indentation size effect, must be the same although the finite volume is

defined respectively by grain boundaries, by free surfaces, and by the edge of a strain field. All these different size effects may be unified to a single size effect.

In conclusion from all these experimental evidence, the general $1/\sqrt{l}$ behaviour should be valid, universally (with and without strain gradient) and might start from the same origin. Also, the effective length scale must be defined to include all extrinsic and intrinsic length scales.

Correspondingly, a theory based on the slip-distance model of Conrad *et al.*, 1967) is suggested, which naturally generates the $1/\sqrt{l}$ with and without strain gradient. The effective length is determined including all extrinsic and intrinsic effects. In chapter 8, it is shown that the theory agrees well with experiments in various loading geometries (Figs.8.5-8.7). Fittings for other geometries can be found in the submitted paper Zhu *et al.* (2008c).

Another key result found in this study is the influence of magnitude of size effects due to material parameters. In chapter 4, by comparing the bending results of copper and nickel, the size effects (both grain and thickness size effects) appear to be geometrical, i.e., independent of material parameters. This agrees well with Spary *et al.* (2006), who studied indentation size effect. However, both of these two studies (bending in chapter 4 and Spary *et al.*, (2006)) are performed on soft metals, where the only significantly different material parameter is the elastic modulus. In chapter 7 (Figs. 7.5 and 7.6), it is observed that the normalised yield pressure for metals and ceramics fell on quite different slopes in spite of similar ranges of elastic modulus in both sets of materials; that is, the magnitude of the size effect appeared to be greater

in metals than ceramics. This result implies that material parameters as well as geometry must be important in length scale plasticity. Which parameters can account for the difference in the size effect between metals and ceramics?

In chapter 8, the slip-distance model suggests that the magnitude of the size effect is controlled by the yield strain and the Burger's vector for the material. These two factors are very different between metals and ceramics, but not between metals. This explains why the magnitude of size effect is distinguished in chapter 7 for indentation on metals and ceramics, but not obvious in bending nickel and copper foils (chapter 4) or nanoindentation on a series of soft metals (Spary *et al.*, 2006). The theory shows good agreement with experimental observations (Fig.8.8).

10 Conclusions

More accurate data are successfully obtained over a wider range of strain (0 to 0.1) and grain size (d / h ranged from 3 to 0.03) from bending of nickel and copper thin foils. However, the yield study has still not been completed. Better data around the elastic-plastic region is required. The symmetry between d and h in work hardening coefficient and flow strength and the continuity of data or fits between $d < h$ and $d > h$, may suggest that the grain boundary and free surface have the same effect in plastic deformation. Comparing the bending results of nickel and copper, both grain and thickness size effects are geometrical, i.e., independent on material properties.

The direct method of determining gross yield strength for ceramics and high strength metals by using spherical nanoindentation, is proved to be comparable with Spary *et al.* (2006) from finite modelling simulation together with indentation. The normalised yield pressure shows similar dependence on contact size for all ceramics, while the metals show very different slope. That is, the magnitude of size effect is appeared to be greater in metals than ceramics. By comparing the Berkovich and spherical indentation size effects, the results imply that the contact size a is the most fundamental length scale in indentation size effect, independent of the shape of the indenter. The indentation strength is inversely scaled with the square root of a.

Taking the Hall-Petch, pillar, bending and indentation size effects together, it may be concluded that the strengthening of the materials is driven by the restricted strain volume. The delimited boundary condition of the volume is not relevant.

The slip-distance theory (based on (Conrad *et al.*, 1967)) appears able to account for the size effects in all contexts (uniform or non-uniform, with or without grain size interaction with extrinsic size and for different geometries), without requiring strain gradient plasticity theory or an implicit characteristic length. The slip-distance model also suggests that the magnitude of the size effect is controlled by the yield strain and the Burger's vector of the material, which agrees with experimental observations.

This thesis presents data which in most experiments is improved the literature data in accuracy or in range of parameter. The improved data has highlighted the ubiquity of the $1/\sqrt{l}$ behaviour and suggested a common origin. Slip-distance theory is certainly shown to be consisted with an 'effective length scale' reconciling intrinsic and extrinsic size effects and predicting a wide range of geometrical size effects.

11 Future work

The study of material yield is certainly interesting and useful to be completed. Better technique may be required for achieving that, e.g., twisting a long wire.

In the bending of nickel foil (chapter 3 and 5), it is shown that the strength is inversely scaled with the square root of effective length l_{eff} together with a square-root work hardening, at small strain region. However, at high strain, the linear work hardening is operating and the strength is scaled with the reciprocal of l_{eff}. Is this generally true for all different loading geometries? If so, why the size effect is changing with different work hardening behaviour? Why it is different between small and high strain region? What is the underlying physics?

Whether the shortest contact length is always the dominating length in size effect? By testing this, the best experiment may be on asymmetric subjects: e.g., knife edge indentation and wall-pillar compression tests.

Furthermore, in this thesis, interaction between intrinsic and extrinsic size effects is studied experimentally and theoretically. However, this is limited by the interaction between two sizes. It will be very interesting to study the interaction among more sizes, e.g., interaction among indention contact size, film thickness and grain size effects. A possible theory for this is also proposed and shown in the Appendix.

References

Abadias, G. Michel, A., Tromas, C., Jaouen, C. and Du, S.N.: 2007. Stress, interfacial effects and mechanical properties of nanoscale multilayered coatings. *Sur. oat. Technol.*, **202**, 844–53.

Armstrong, R.W., Codd, I., Douthwaite, R.M., and Petch, N.J.: 1962. The plastic deformation of polycrystalline aggregates. *Phil. Mag.*, **7**, 45.

Armstrong, R.W.: 1970. In: Herman, H. (Ed.), Wiley, New York, 101–145.

Arsenlis, A. and Park, D.M.: 1999. Crystallographic aspects of geometrically-necessary and statistically-stored dislocation density. *Acta. Mater*, **47**, 1597-1611.

Artz, E.: 1998. Size effects in materials due to microstructural and dimensional constraints: a comparative. *Acta Mater.*, **46**, 5611-26.

Ashby, M.F.: 1970. The deformation of plastically non-homogeneous materials. *Philos. Mag.* **21**, 399–424.

Bishop, J.F.W and Hill, R.: 1951. A theoretical derivation of the plastic properties of a polycrystalline face-centered metal. *Phil.Mag.*, **42**, 1298.

Bishop, J.F.W and Hill, R.: 1951. A theory of plastic distortion of a polycrystalline aggregate under combined stresses. *Phil.Mag.*, **42**, 414.

Brenner, S.S.: 1956. Tensile strength of whiskers. *J. Appl. Phys.* **27**, 1484–91.

Brenner, S.S.: 1958. Growth and properties of 'whiskers'. *Science*, **128**, 568–75.

Brown, L. M. and Ham, R. K. 1971. Strengthening methods in crystals. Ed. Kelly, A. and Nicholson, R. B., Applied Science Publishers Ltd., London.

Budiman, A.S., Han, S.M., Greer, J.R., Tamura, N., Patel, J.R. and Nix, W.D.: 2008. A search for evidence of strain gradient hardening in Au submicron pillars under uniaxial compression using synchrotron X- ray microdiffraction. *Acta Mater.*, **56**, 602–8.

Bushby, A.J. and Jennett, N.M.: 2001. Determining the area function of spherical indenters for nanoindentation. In: Baker, S.P., Cook, R.F., Corcoran, S.G., Mood, N.R. (Eds.). *Materials Research Society Symposium Proceedings*. Fundamental of Nanoindentation and Nanotribology. **649**, pp. Q7.17.1-6

Bushby, A.J., Zhu, T.T. and Dunstan, D.J.: 2008. Slip distance model for the indentation size effect at the initiation of plasticity in ceramics and metals. *Journal of Materials Research*, in press.

Bushby, A.J.: 2001. Nano-indentation using spherical indenters. *Nondestruct. Test. Eval.*, **17**, 213-234.

Cao, Y., Allameh, S., Nankivil, D., Sethiaraj, S., Otiti, T. and Soboyejo, W.: 2006. Nanoindentation measurements of the mechanical properties of polycrystalline Au and Ag thin films on silicon substrates: effects of grain size and film thickness. *Mater. Sci. Eng. A*, **427**, 232–40.

Chia, K-H., Jung, K. and Conrad, H.: 2005. Dislocation density model for the effect of grain size on the flow stress of a Ti–15.2 at.% Mo β-alloy at 4.2–650 K. *Mater. Sci. Eng. A*, **409**, 32–38.

Conrad, H. and Jung, K.: 2005. Effect of grain size from mm to nm on the flow stress and plastic deformation kinetics of Au at low homologous temperatures. *Mater. Sci. Eng. A*, **406**, 78-85.

Conrad, H., Feuerstenin, S. and Rice, L.: 1967. Effect of grain size on the dislocation density and flow stress of Niobium. *Mater. Sci. Eng. A*, **2**. 157.

Cracknell, A. and Petch, N.J.: 1955. Frictional forces on dislocation arrays at the lower yield point in Iron. *Acta. Met.*, **3**, 186.

Duan, D.M., Wu, N.Q., Slaughter, W.S. and Mao, S.X.: 2001. Length scale effect on mechanical behavior due to strain gradient plasticity. *Mater. Sci. Eng. A* **303**, 241.

Dunstan, D.J. and Bushby, A.J.: 2004. Theory of deformation in small volumes of material. *Proc. R. Soc. Lond. A*, **460**, 2781–96.

Dunstan, D.J.: 1997. Review strain and strain relaxation in semiconductors. *Journal of Materials Sience: Mterials in Eectronics*, **8**, 337-375.

Durst, K., Backes, B., Franke, O., Goken, M.: 2006. Indentation size effect in metallic materials: Modeling strength from pop-in to macroscopic hardness using geometrically necessary dislocations. *Acta Materialia*, **54**, 2547-55.

Ebrahimi, F., Bourne, G.R., Kelly, M.S. and Matthews, T.E.: 1999. Mechanical Properties of Nanocrystalline Nickel Produced by Electrodeposition. *Nanostruct. Mater.* **11**, 343-50.

Ehrler, B., Hou, X.D., Zhu, T.T., P'ng, K.M.Y., Walker, C.J., Bushby, A.J. and Dunstan, D.J.: 2008. Grain size and sample size interact to determine strength in a soft metal. *Phil. Mag.*, in press.

Eshelby, J.D.: 1951. The force on an elastic singularity. *Phil. Trans. R. Soc. A*, **244**, 87-112.

Espinosa, H.D., Prorok, B.C., and Peng, B.: 2004. Plasticity size effects in free-standing submicron polycrystalline FCC films subjected to pure tension. *J. Mech. Phys. Solids*, **52**, 667–689.

Fang, L. and Friedman, L. H.: 2005 Strength of metallic multilayers at all length scales from analytic theory of discrete dislocation pileups. *Philos. Mag.*, **85**, 3321–55.

Field, J.S and Swain, M.V.: 1995. Determining the mechanical properties of small volumes of material from submicrometer spherical indentations. *J. Mater. Res.*, **10**, 101-12.

Field, J.S. and Swain, M.V.: 1993. A simple predictive model for spherical indentation. *J. Mater. Res.*, **8**, 297-306.

Fischer-Cripps, A.C.: 2000. Introduction to contact mechanics. Ling, F.F.(Ed), Spring-Verlag New York Berlin Heidelberg.

Fischer-Cripps, A.C.: 2001. Nanoindentation. Springer, New York.

Fitzgerald, E.A.: 1991. Dislocations in strained- layer epitaxy: theory, experiment, and applications. *Mater. Sci. Reports*, **7**, 87-142.

Fleck, N.A. and Hutchinson, J.W.: 1993. A phenomenological theory for strain gradient effects in plasticity. *J. Mech. Phys. Solids*, **41**, 1825-57.

Fleck, N.A. and Hutchinson, J.W.: 2001. A reformulation of strain gradient plasticity. *J. Mech. Phys. Soldis*, **49**, 2245.

Fleck, N.A. and Hutchinson, J.W.: 1997. Strain gradient plasticity. *Adv. Appl. Mech.*, **33**, 295.

Fleck, N.A., Muller, G.M., Ashby, M.F. and Hutchinson, J.W.: 1994. Strain gradient plasticity: theory and experiments. *Acta. Metall. Mater.*, **42**, 475-487.

Frank, F.C. and Merwe, J. H.ven der: 1949. One-dimensional dislocations: misfitting monolayers and oriented growth. *Proc Roy Soc (London)*: **A198**, 216.

Freund, L.B.: 1987. The stability of a dislocation threading a strained layer on a substrate. *J. Appl. Mech.*, **54**, 553-7.

Gao, H., Huang, Y., Nix, W.D. and Hutchinson, J.W.: 1999. Mechanism based strain gradient plasticity. *J. Mech. Phys. Solids*, **48**, 1239-63.

Gerberich, W.W., Cordill, M.J., Mook, W.M., Moody, N.R., Perrey, C.R., Carter, C.B., Mukherjee, R. and Girshick, S.L.: 2005. A boundary constraint energy balance criterion for small volume deformation. *Acta Mater.*, **53**, 2215–29.

Gerberich, W.W., Mook, W.M., Perrey, C.R., Carter, C.B., Baskes, M.I. and Mukherjee, R.: 2003. Superhard silicon nanospheres. *J. Mech. Phys. Sololid*, **51**, 979-92.

Gerberich, W.W., Tymiak, N.I., Grunlan, J.C., Horstemeyer, M.F. and Baskes, M.I.: 2002. An energy balance criterion for nanoindentation-induced single and multiple dislocation events. *J. Appl. Mech.*, **69**, 433-442.

Gouldstone, A., Koh, H.-J., Zeng, K.-Y., Giannakopoulos, A.E. and Suresh, S.: 2000. Discrete and continuous deformation during nanoindentation of thin films. *Acta Mater.*, **48**, 2277-95.

Greer, J.R. and Nix, W.D.: 2006. Nanoscale gold pillars strengthened through dislocation starvation, *Phys. Rev. B*, **73**, 245410-6.

Greer, J.R., Warren, O.C. and Nix, W.D.: 2005. Size effects in mechanical properties of gold at the micron scale in the absence of strain gradients. *Acta Mater.*, **53**, 1821–30.

Griffith, A.A.: 1920. Phenomena of rupture and flow in solids. *Philos. Trans. R. Soc. London A*, **221**, 163-198.

Hackelöer, H. J., Selbach, H., Kanert, O., Sleeswyk, A. W. and Hut, G.: 1977. Determination of the velocity of mobile dislocations by nuclear spin relaxation measurements. *Physica Status Solidi (b)*, **80**, 235-43.

Hall, E. O.: 1951. The deformation and aging of mild steel: iii discussion of results. *Proc. Phys. Soc. Lond.*, **64**, 747–53.

Han, C.S., Gao, H., Huang, Y., Nix, W.D.: 2005. Mechanism based strain gradient crystal plasticity - Analysis. *J. Mech. Phys of solids*, **53**, 1188–1203.

Hansen, N: 2004. Hall–Petch relation and boundary strengthening. *Scr. Mat.* **51**, 801.

Herbert, E.G., Oliver, W.C., Pharr, G.M.: 2006. On the measurement of yield strength by spherical indentation. *Phil. Mag.* **86**, 5521-39.

Herrmann, K., Jennett, N.M., Kuypers, S., McEntegaart, I., Ingelbrecht, C., Hangen, U., Chudoba, T., Pohlenz, F., Menelao, F.: 2003. Investigation of the properties of candidate reference materials suited for the calibration of nanoindentation instruments. *Zeitschrift fur Metallkunde.* **94**, 802-6.

Hertz. H.: 1882. On the contact of elastic solids. *J. Reine Angew. Math.*, **92**, 156-171.

Hill, R.: 1950. The mathematical theory of plasticity. Editors: Moullin, E.B., Pye, D.R. and Southwell, R.V. Oxford at the Clarendon Press.

Hoagland, R.G., Kurtz, R.J. and Henager, C.H.: 2004. Slip resistance of interfaces. and the strength of metallic multilayer composites. *Scripta Mater.*, **50**, 775–79.

Hommel, M. and Kraft, O.: 2001. Deformation behavior of thin copper films on deformable substrates. *Acta. Mater.*, **49**, 3935–47.

Horstemeyer, M. F., Baskes, M.I., Prantil, V.C., Philliber, J. and Vonderheide, S.: 2003. A multiscale analysis of fixed-end simple shear using molecular dynamics, crystal plasticity, and a macroscopic internal state variable theory. *Modelling Simul.Mater. Sci. Eng.*, **11**, 265–86.

Hou, X.D., Bushby, A.J. and Jennett, N.J.: 2008. Study of the interaction between the indentation size effect and Hall-Petch effect with spherical indenters on annealed polycrystalline copper. *Journal of Physics D: Applied Physics*, **41**, 074006 (6pp).

Huang, Y., Gao, H., Nix, W.D. and Hutchinson, J.W.: 2000. Mechanism based strain gradient crystal plasticity-Analysis. *J. Mech. Phys. Solids*, **48**, 99-128.

Huang, Y., Qua, S., Hwang, K.C., Li, M. and Gao, H.: 2004. A conventional theory of mechanism-based. strain gradient plasticity. *International Journal of Plasticity*, **20**, 753–82.

Hutchinson, J. W.: 2002. Plasticity at the micron scale. *Int. J. Solids Struct.*, **37**, 225-38.

Inglis, C.E.: 1913. Stresses in a plate due to the presence of cracks and sharp corners. *Trans Inst Naval Archit.*, **55**, 219–41.

Jayaweera, N. B., Downes, J.R., Dunstan, D. J., Bushby, A. J., Kidd, P., Kelly, A.: 2001. Coherency strain and a new yield criterion. *Mater. Res. Soc. Symp. Proc.* **634**, B4.10.

Jayaweera, N.B., Downes, J.R., Frogley, M.D., Hopkinson, M., Bushby A.J., Kidd, P., Kelly, A. and Dunstan, D.J.: 2003. The onset of plasticity in nanoscale contact loading. *Proc. R. Soc. Lond. A.*, **459**, 2049-68.

Johnson, K.L.: 1985. Contact Mechanics. Cambridge University Press.

Keller, R-M., Baker, S. P. and Arzt, E.: 1998. Quantitative analysis of strengthening mechanisms in thin Cu films: effects of film thickness, grain size and passivation. *J. Mater. Res.*, **13**, 1307-17.

Kiener, D., Motz, C., Schöberl, T., Jenko, M. and Dehm, G.: 2006. Determination of mechanical properties of copper at the micron scale. *Adv. Eng. Mater.*, **8**, 1119–25.

Kocks, U.F., 1970. The relation between polycrystal deformation and single crystal deformation. *Metallurgical and Materials Transactions*, **1**, 1121–1144.

Lawn, B. R.: Fracture of brittle solids, 1975 Cambridge University Press, Cambridge, England.

Li, J.C.M. and Chou, Y.T.: 1970. The role of dislocations in the low stress-grain size relationships. *Metallurgical Transactions*, **1**, 1145-59.

Li, J.C.M.: 1963. Petch relation and grain boundary sources. *Transactions of the Metallurgical Society of AIME*, **227**, 239-47.

Lim, Y.Y. and Chaudhri, M. M.: 1999. The effect of the indenter load on the nanohardness of ductile metals: an experimental study on polycrystalline work-hardened and annealed oxygen-free copper. *Philos. Mag. A*, **79**, 2979- 3000.

Lloyd, D.J.: 1994. Particle reinforced aluminium and magnesium matrix composites. *International Materials Reviews*, **39**, 1-23.

Ma, Q. and Clarke, D. R.: 1995. Size dependent hardness in silver single crystals. *Journal of' Materials Research*, **10**, 853-63.

Madelung, O.: 1991. Semiconductors group IV elements and III-V compounds. Springer-Verlag, Berlin.

Matthews, J. W.: 1966. Accommodation of misfit across the interface between single-crystal films of various face-centred cubic metals. *Philos. Mag.*, **13**, 1207-13.

Mattoni, A., Colombo, L. and Cleri, F.: 2005. Atomic scale origin of crack resistance in brittle fracture. *Philos. Rew. Letter.*, **95,** 115501.

Meyers, M.A., Mishra, A. and Benson, D.J.: 2006. Mechanical properties of nanocrystalline materials. *Progress in Materials Science*, **51** 427–556.

Misra, A., Hirth, J.P. and Hoagland, R.G.: 2005. Length-scale-dependent deformation mechanisms in incoherent metallic multilayered composites. *Acta Mater.*, **53**, 817–24.

Moreau, P., Raulic, M., P'ng, K. M. Y., Gannaway, G., Anderson, P., Gillin, W. P., Bushby, A. J. and Dunstan, D.J.: 2005. Measurement of the size effect in the yield strength of nickel foils. *Philos. Mag. Lett.*, **85**, 339–43.

Murr, L.E.: 1975. Interfacial phenomena in metals and alloys. Addison-Wesley. pp. 338-344.

Nicola, L., Bower, A.F., Kim, K.-S., Needleman, A., Giessen, E. Van der: 2007. Surface versus bulk nucleation of dislocations during contact. *J. Mech. Phys. Solids*, **55**, 1120–44.

Nix, W.D.: 1989. Mechanical properties of thin films. *Metall. Trans. A*, **20**, 2217-45.

Nix, W.D. and Gao, H.: 1998. Indentation size effects in crystalline materials: a law for strain gradient plasticity. *J. Mech. Phys. Solids*, **46**, 411-25.

Nix, W.D., Greer, J.R., Feng, G. and Lilleodden, E.T.: 2007. Nanoscale gold pillars strengthened through dislocation starvation. *Thin Solid Films*, **515**, 3152–7.

Nye, J.F.: 1963. Some geometrical relations in dislocated crystals. *Acta Metall*, **1**, 153-162.

Oliver, W.C. and Pharr, G.M.: 1992. Improved technique for determining hardness and elastic modulus using load and displacement sensing indentation experiments. *J. Mater. Res.* **7**, 1564–1580.

Orowan, E.: 1947. Symposium on Internal Stress. Institute of metals, London, pp451.

Petch, N. J., 1953. The cleavage strength of polycrystals. *J. Iron Steel Inst.*, **174**, 25–28.

Phillips, M.A., Spolenak, R., Tamura, N., Brown, W.L., MacDowell, A.A., Celestre, Padmore, H.A., Batterman, B.W., Arzt, E. andPatel, J.R.: 2004. X-ray

microdiffraction: local stress distributions in polycrystalline and epitaxial thin films. *Microelectronics Engineering*, **75**, 17-126.

Phillips, W.L. and Armstrong, R.W.: 1972. The strain dependence of the flow stress-grain size relation for. 70:30 brass. *Metall. Trans. A*, **3**, 2571-7.

P'ng, K.M.Y: 2005. Strength and deformation of coherently strained superlattices. PhD thesis.

Qin, J., Huang, Y., Hwang, K.C., Song, J. and Pharr, G.M.: 2007. The effect of indenter angle on the micronindentation hardness. *Acta Materialia*, **55**, 6127.

Qu, S., Huang, Y., Pharr, G.M. and Hwang, K.C.: 2006. The indentation size effect in the spherical indentation of iridium: a study via the conventional theory of mechanism-based strain gradient plasticity. *Int. J. Plasticity*, **22**, 1265.

Sack. R.A.: 1946. Extension of Griffith's theory of rupture to three dimensions. *Proc. Phys. Soc. (London)*, **58**, 729-36

Shan, Z. W., Mishra, R., Asif, S.A.S., Warren, O. and Minor, A. M.: 2008. Mechanical annealing and source-limited deformation in submicrometre-diameter Ni crystals. *Nature Materials*, **7**, 115-9.

Shen, Y.-L., Suresh, S., He, M.Y., Bagchi, A., Kienzle, O., Ruhle, M. and Evans, A.G.: 1998. Stress evolution in passivated thin films of Cu on silica substrates. *J. Mater. Res.*, **13**, 1928–37.

Sneddon, I.N.: 1965. The relation between load and penetration in the axisymmetric boussinesq problem for a punch of arbitrary profile. *Int. J. Eng. Sci.*, **3**, 47–57.

Spary, I.J., Bushby, A.J. and Jennet, N.J.: 2006. On the indentation size effect in spherical indentation. *Phil. Mag.*, **86**, 5581–93.

Stölken, J.S. and Evans, A.G.: 1998. A microbend test method for measuring the plasticity length-scale. *Acta Metall.*, **46**, 5109-15.

Swadener, J.G. and Pharr, G.M.: 2001. Indentation modulus of elastically anisotropic half-spaces by cones and parabolae of revolution. *Phil. Mag. A.*, **81**, 447-466

Swadener, J.G., George, E.P. and Pharr, G.M.: 2002. The correlation of the indentation size effect measured with indenters of various shapes. *J. Mech. Phys. Solids.*, **50**, 681–94.

Syed Asif, S.A. and Pethica, J.B. 1997. Nanoindentation creep of single-crystal tungsten and gallium arsenide. *Phil. Mag. A*, **76**, 1105-18.

Tabor D.: 1951. The Hardness of Metals. Clarendon Press, Oxford.

Taylor, G.I.: 1934. The mechanism of plastic deformation of crystals. Part I.—theoretical. *Proc. Roy. Soc., A*, **145**, 362-388.

Thompson, C.V.: 1993. The Yield stress of polycrystalline thin films. *J. Mater. Res.*, **8**, 237-8.

Uchic, M.D., Dimiduk, D.M., Florando, J.N. and Nix, W.D.: 2004. Sample dimensions influence strength and crystal plasticity. *Science*, **305**, 986-9.

Venkatraman, R. and Bravman, J. C.: 1992. Separation of film thickness and grain boundary strengthening effects in Al thin films on Si. *J. Mater. Res.*, **7**, 2040-8.

Volkert, C.A. and Lilleodden, E.T.: 2006. Size effects in the deformation of sub-micron Au columns. *Philos. Mag.*, **86**, 5567-80.

Widjaja, W., Giessen, E.V. and Needleman, A.: 2007. Discrete dislocation analysis of the wedge indentation of polycrystals. *Acta Mat.*, **55**, 6408-15.

Zhang, T.-Y. and Xu, W.H.: 2002. Surface effects on nanoindentation. *J. Mater. Res.*, **17**, 1715-20.

Zhu, T.T., Bushby, A.J. and Dunstan, D.J.: 2008b. Size effect in the initiation of plasticity for ceramics in nanoindentation. *J. Mech. Phys of Solids*, **56**, 1170-1185.

Zhu, T.T., Bushby, A.J. and Dunstan, D.J.: 2008c. Analysis of the inverse square-root size effect in plasticity of metals. submitted.

Zhu, T.T., Hou, X.D., Bushby, A.J. and Dunstan, D.J.: 2008a. Indentation size effect at the initiation of plasticity for ceramics and metals. *J. Phys. D: Appl. Phys.*, **41**, 074004 (6pp)

Appendix

The situation of polycrystalline thin film coating indentation size effect is considered. In this case, three size will interact, i.e., thickness h, indentation contact size a and grain size d.

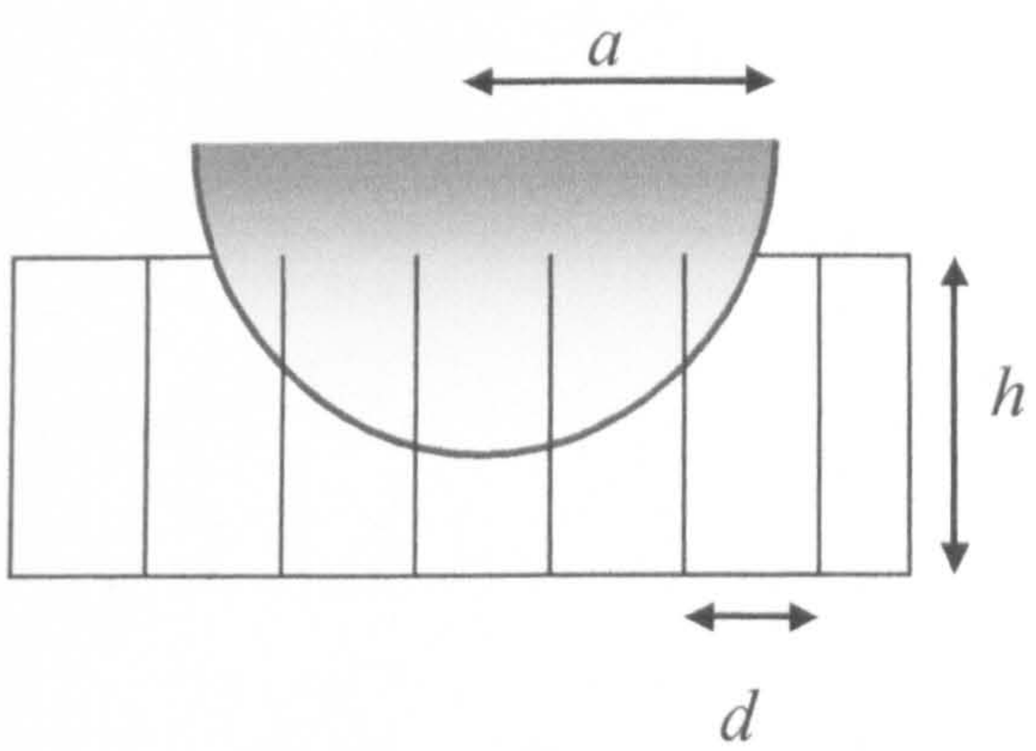

Figure A.1 Schematic of the plastic deformation zone beneath a spherical indentation with contact radius a, on a thin film with thickness h and grain size d. In thin film coating, grains normally shows column structure.

So different effective lengths in these directions are expected:

$$\frac{1}{l_x} = \frac{1}{l_y} = \frac{1}{d} + \frac{1}{2a} \tag{A.1}$$

$$\frac{1}{l_z} = \frac{1}{a} + \frac{1}{h} \tag{A.2}$$

Some suitable average should be taken, e.g. (similar as in session 8.3),

$$\frac{1}{l_{eff}} = \frac{1}{3}\left(\frac{1}{l_x} + \frac{1}{l_y} + \frac{1}{l_z}\right) = \frac{2}{3d} + \frac{2}{3a} + \frac{1}{3h} \tag{A.3}$$